Florida International University
FIU Digital Commons

FIU Electronic Theses and Dissertations | University Graduate School

11-23-2015

Climatology of overshootings in tropical cyclones and their roles in tropical cyclone intensity changes using TRMM data

Cheng Tao
ctao003@fiu.edu

DOI: 10.25148/etd.FIDC000237
Follow this and additional works at: https://digitalcommons.fiu.edu/etd

Recommended Citation
Tao, Cheng, "Climatology of overshootings in tropical cyclones and their roles in tropical cyclone intensity changes using TRMM data" (2015). *FIU Electronic Theses and Dissertations*. 2457.
https://digitalcommons.fiu.edu/etd/2457

This work is brought to you for free and open access by the University Graduate School at FIU Digital Commons. It has been accepted for inclusion in FIU Electronic Theses and Dissertations by an authorized administrator of FIU Digital Commons. For more information, please contact dcc@fiu.edu.

FLORIDA INTERNATIONAL UNIVERSITY

Miami, Florida

CLIMATOLOGY OF OVERSHOOTINGS IN TROPICAL CYCLONES AND THEIR ROLES IN TROPICAL CYCLONE INTENSITY CHANGES USING TRMM DATA

A dissertation submitted in partial fulfillment of

the requirements for the degree of

DOCTOR OF PHILOSOPHY

in

GEOSCIENCES

by

Cheng Tao

2016

To: Dean Michael R. Heithaus
College of Arts, Sciences and Education

This dissertation, written by Cheng Tao, and entitled Climatology of Overshootings in Tropical Cyclones and Their Roles in Tropical Cyclone Intensity Changes Using TRMM Data, having been approved in respect to style and intellectual content, is referred to you for judgment.

We have read this dissertation and recommend that it be approved.

_____
Hugh Willoughby

_____
Ping Zhu

_____
Xiaosheng Li

_____
Haiyan Jiang, Major Professor

Date of Defense: November 23, 2015

The dissertation of Cheng Tao is approved.

_____
Dean Michael R. Heithaus
College of Arts, Sciences and Education

_____
Andrés G. Gil
Vice President for Research and Economic Development
and Dean of the University Graduate School

Florida International University, 2016

ACKNOWLEDGMENTS

First and foremost, I would like to thank Dr. Haiyan Jiang for her continuous support during my PhD study and research in the past 5 years. Without her patience, expertise, and guidance, most accomplishments achieved today would not have been possible.

I also would like to give my sincere gratitude to the rest of my committee members: Dr. Hugh Willoughby, Dr. Ping Zhu and Dr. Xiaosheng Li, as they generously provided their immense knowledge and insightful advice in various fields, which contributed greatly to this manuscript.

Besides my committee members, I would like to thank Drs. Tie Yuan and Chuntao Liu for their extraordinary resourcefulness in sharing their knowledge on TRMM data processing. My communications with Drs. Chuntao Liu, Daniel Cecil, Jon Zawislak, and Robert Rogers also provided subtle feedback. In addition, critical comments from Dr. Ed Zipser and two anonymous reviewers helped to improve chapter 3 substantially.

My appreciation also goes to my fellow graduate students including Joseph Zagrodnik, Margie Kieper, Yongxian Pei, Brad Klotz, Cen Gao, Jonathan Furst, Corey Walton, and Amaryllis Cotto. They have brought up brilliant questions from various perspectives and provided useful comments on this project, programming, and graduate coursework.

This work is supported financially by the NASA Earth and Space Science Fellowship (NESSF) award (#NNX11AL66H) and the Dissertation Year Fellowship of FIU. Additional support for this study is also provided by the NASA Precipitation Measurement Mission (PMM) grant NNX10AE28G, NASA Hurricane Science Research Program (HSRP) grant NNX10AG34G, NASA New Investigator Program (NIP) award

(#NNX10AG55G), and NOAA Joint Hurricane Testbed (JHT) grants NA11OAR4310193 and NA13OAR4590191. Specifically, I thank Drs. Ramesh Kakar and Ming-Ying Wei (NASA headquarters) for their continued support of TRMM and hurricane sciences.

Last but not the least, I would like to thank my husband Chao and my parents for their constant encouragement, love and support during my time in graduate school.

ABSTRACT OF THE DISSERTATION

CLIMATOLOGY OF OVERSHOOTINGS IN TROPICAL CYCLONES AND THEIR ROLES IN TROPICAL CYCLONE INTENSITY CHANGES USING TRMM DATA

by

Cheng Tao

Florida International University, 2016

Miami, Florida

Professor Haiyan Jiang, Major Professor

The climatology of overshooting convection in tropical cyclones (TCs) is examined using Tropical Rainfall Measuring Mission (TRMM) Precipitation Radar (PR). The percentage of TC convective systems with overshooting convection is highest over the North Indian Ocean basin, while the northwest Pacific basin contains the highest population of both TC convective systems and convection with overshooting tops. Convective systems in the inner core region are more capable of penetrating 14 km and the associated overshooting convection are featured with much stronger overshooting properties compared with those in the inner rainband and outer rainband regions. In the inner core region of TCs, convection associated with precipitating systems of higher intensity and intensification rates has a larger probability of containing overshooting tops.

To identify the relative importance of shallow/moderate versus deep/very deep convection in the rapid intensification (RI) of TCs, four types of precipitation-convection are defined based on the 20 dBZ radar echo height (Z_{20dBZ}). Distributions of four types of precipitation-convection, and their contributions to total volumetric rain and total latent heating are quantified. It is shown that RI is closely associated with increased and widespread shallow precipitation around the storm center, while moderately deep and very deep convection (or overshooting convection) does not increase until in the middle of RI. This is further confirmed by the study of rainfall and convection evolution with respect to

the timeline of RI events. Statistically, the onset of RI follows a significant increase in the areal coverage of rainfall, shallow precipitation, and cyan of 37 GHz color composites upshear-left, which in turn could be used as potential parameters to forecast RI. Very deep convection is most frequent 12-24 hours before RI onset and concentrates upshear-left, but it quickly decreases in the following 24 hours. The percent occurrence of very deep convection is less than 1% for RI storms. The tilt of vortex is large prior to, and near the RI onset, but rapidly decreases in the middle of RI, suggesting that the vertical alignment is a result instead of a trigger of RI.

TABLE OF CONTENTS

LIST OF TABLES

TABLE PAGE

LIST OF FIGURES

FIGURE PAGE

LIST OF ACRONYMS AND ABBREVIATIONS

ATL	Atlantic
CAPE	Convective Available Potential Energy
CAT 1-2	Category 1-2 hurricanes
CAT 3-5	Category 3-5 hurricanes
CDF	Cumulative Distribution Function
DSD	Drop Size Distribution
EPA	East central Pacific
EM	Electromagnetic
FOV	Field of View
IB	Inner rainband
IC	Inner core
ITCZ	Inter Tropical Convergence Zone
LNB	Level of Neutral Buoyancy
LNB_{sfc}	Level of Neutral Buoyancy calculated using NCEP sounding and surface equivalent potential temperature
$LNB_{925\&1000}$	Level of Neutral Buoyancy calculated using potential temperature at 925 and 1000mb
NIO	North Indian Ocean
NWP	Northwest Pacific
OB	Outer rainband
OTCPF	Overshooting Tropical Cyclone Precipitation Feature
PCT	Polarization Corrected Temperature
PR	Precipitation Radar

PF	Precipitation Feature
RI	Rapidly Intensification
RMW	Radius of maximum wind
SI	Slowly Intensification
SPCZ	South Pacific Convergence Zone
SIO	South Indian Ocean
SPA	South Pacific
T_{B11}	Minimum 11-μm brightness temperature
TC	Tropical Cyclone
TCPF	Tropical Cyclone Precipitation Feature
TD	Tropical Depression
TMI	TRMM Microwave Imager
TRMM	Tropical Rainfall Measuring Mission
TS	Tropical Storm
VIRS	Visible and Infrared Scanner
Z_{trop}	Level of NCEP reanalysis tropopause
Z_{380K}	Level of 380-K potential temperature

1. INTRODUCTION AND BACKGROUND

1.1 Overview

Tropical deep convection that penetrates into the tropopause region (i.e., overshooting convection, or “hot towers”) has long been recognized as a very essential agent for heat and moisture transportation (Riehl and Malkus, 1958; Simpson, J. 1990) as well as mass exchange (Holton et al. 1995; Dessler, 2002) between the upper troposphere and lower stratosphere. Part of the deep convection with overshooting tops in the tropics and sub-tropics (within 35^{o} of the equator) occurs in tropical cyclones (TCs). A recent research by Romps and Kuang (2009) suggested that TCs contribute a disproportionate percentage to global systems with overshooting convection. As existing studies mostly focused on intense convection in general convective systems (e.g., Alcala and Dessler, 2002; Liu and Zipser, 2005), statistical analysis of the climatology of overshooting convection in TCs is highly desirable and will have important implications in terms of the contribution of TCs in global hydrologic and energy cycle.

In the meantime, some works proposed that extremely intense convection near the storm center is related to the intensification of TCs (e.g., Simpson et al. 1998; Kelley et al. 2004, 2005; Montgomery et al. 2006). For rapid intensification (RI), particularly, horizontally small, asymmetric deep convection (such as convective bursts and hot towers) within the inner core region of TCs was considered to link with their spin-up mechanism in several observational studies (Reasor et al. 2009; Reasor and Eastin, 2012; Nguyen and Molinari, 2012). Further quantification based on long-term satellite observations is needed to validate the hypothesis of theoretical and case studies on the role of overshooting

convection in RI, and may enhance our understanding of TC intensity change and improve the forecast of TC wind intensity.

Quantifying convection/precipitation in TCs is a difficult endeavor, as TCs spend most of their lifetime over ocean where no rain gauge or ground-based radar networks are available. To provide precipitation measurements across the global tropics, the Tropical Rainfall Measuring Mission satellite (TRMM, Simpson et al. 1988, 1996; Kummerow et al. 1998, 2000) launched in November 1997 and has produced over 17 years of valuable scientific data. The TRMM has contributed to improved understanding over a wide variety of weather and climate topics, including TC structure and evolution, which is most pertinent to the present study. Furthermore, with the first-ever satellite-based precipitation radar (PR), TRMM provided the unique opportunity to examine the vertical structure and properties of cloud systems and their distributions over the global tropics.

1.2 Overshooting Convection and Tropical Cyclones

1.2.1 Overshooting Convection

In general, convection refers to the transport of some property by fluid movement. In the present study, the term of "convection" is used to represent the heat transport by the vertical component of the flow associated with buoyancy. Part of the dynamics of convection can be explained by the "parcel theory". In theoretical studies, the development of deep convection can be viewed as in a large-scale environment of horizontally uniform temperature, moisture and wind. Basically, when a parcel of air has higher temperature than the surroundings, it will rise. In an unstable environment, once air is lifted to its level of free convection (LFC) and subsequently remains positively buoyant, it may rise

continuously. Here comes the concept of overshooting convection, which is defined as deep convection that is high enough to penetrate the tropopause. A nickname for overshooting convection is “hot tower”, as it rises high because of a large amount of latent heat released.

Overshooting convection is horizontally small, with a particular scale of approximately 10 km across (Ray, 1986), and lasts approximately 30 to 60 minutes (Hendricks et al. 2004). It is shown that overshooting convection tends to be concentrated within certain areas such as the west Pacific, central Africa, South America, the Inter Tropical Convergence Zone (ITCZ), and the South Pacific Convergence Zone (SPCZ) (Liu and Zipser, 2005). In spite of its small areal coverage, overshooting convection and its associated stratiform precipitation accounts for a disproportionately large rainfall in the tropics.

1.2.2 Tropical Cyclone

A tropical cyclone (TC) is defined as a warm-core, non-frontal, low-pressure systems that develops over the warm tropical oceans. As a synoptic-scale low-pressure system, TCs must spin cyclonically. In other words, they spin counter-clockwise in the Northern Hemisphere and clockwise in the Southern Hemisphere. Tropical cyclones derive their energy from the latent heat in evaporating tremendous amounts of water vapor from the underlying warm ocean surface. The intensity of a TC is measured by its maximum sustained winds at a height of 10 meters above the surface. The formation stage is called a tropical depression (TD), which is designated when a cluster of thunderstorms persist for a long enough time (> 24 hours) in tropical or subtropical regions. If the maximum 10-

minute average winds reach 34 knots (1 knot ≈ 0.51 m/s), the storm is classified as a tropical storm (TS). The storm is upgraded to a hurricane (over the North Atlantic) or a typhoon (over the North Pacific Ocean) when the maximum 10-minute average winds reach 64 knots. Particularly, hurricane intensity is commonly classified into five categories by the Saffir-Simpson scale, with each category covering about a 20-knot interval of wind speed.

As the current wind intensity of a TC is difficult to measure or even to estimate during post-analysis, it is reasonable to try instead to infer the change in wind intensity from the structure of TCs. A TC distinguishes from a mid-latitude synoptic cyclone in that it has a warm core, namely, the air at its center is significantly warmer than the surroundings at the same altitude. Around the cloud-free, warm-core eye is an arc of tall, vigorous, organized band of thunderstorms defined as the eyewall, which contains the strongest tangential winds (winds that swirl about the center) and updraft velocities, and the heaviest rain rates. An eyewall is recognized as a closed eyewall if it is completely surrounding the storm center, and it can be a partial eyewall and/or concentric eyewalls in many cases. Willoughby et al. (1982, 1984) proposed that the storm's radar structure can be identified as the stationary band complex (SBC) that consists of an eyewall, a principal rainband, connecting bands, and several secondary rainbands outside the eyewall. The principal rainbands is the most prominent member of the family, which spirals outward from either the eyewall or the region of stratiform precipitation in the inner rainband region surrounding the eyewall.

Accurate forecasting of both track and intensity of a TC is critical to mitigation of disasters potentially caused by an approaching storm. The change of TC intensity involves

a complex interaction among processes varies from environmental-scales to convective-scales. Most pertinent to the present study is the precipitation and convection in TCs and whether it plays an important role on the intensification, especially rapid intensification (RI), of TCs. Steady precipitation implies a steady addition of energy into the TCs in the form of latent heat released as water vapor condenses, and thus, is a helpful quantity to measure. In contrast, persistent clouds do not provide any information of the amount of energy being added to TCs. The following section gives an overview of the remote sensing technique and how it can be applied to rainfall estimation.

1.3 Remote Sensing Background

Remote sensing is a term that is used to describe the measurements of the physical properties of an object without making actual contact with it. Satellite technology, which is applied in this study, is an example of remote sensing. Through measuring the electromagnetic radiation (EMR) emitted from the object of interest, the physical properties of the earth's surface, atmospheric gases, and atmospheric hydrometers (cloud and rain droplets, ice, hail, or snow) can be inferred from the parameters derived from satellite observations.

1.3.1 Electromagnetic Radiation

Electromagnetic radiation (EMR) is the basis for all remote sensing of the Earth. As its name suggests, EMR has both electric and magnetic components, each component of which is like an electric wave and a magnetic wave oscillating through space perpendicular to each other and perpendicular to the direction of propagation. It is the energy that is

emitted in electromagnetic waves (EM-waves) by all objects with a temperature above absolute zero (-273^{o} C or -459^{o} F). The primary sources of EMR include the sun, earth, and atmosphere.

An electromagnetic wave is often described by its amplitude, its wavelength (λ), and its frequency (f). Amplitude is the height (depth) from the equilibrium point to the highest (lowest) point of a crest (trough) and measures the magnitude of the wave. Wavelength is defined as the distance between two successive wave crests or troughs. Frequency is determined by the number of waves that pass a certain point in a given period of time. The relationship between wavelength and frequency follows the equation $\lambda = c / f$, where c represents the speed of light at approximately 3×10^{8} m s^{-1}.

Generally, objects do not emit radiation in only one wavelength but in specific ranges of wavelengths, which is often referred to as spectrum. The electromagnetic spectrum is a continuum of all types of EMR ordered by wavelength, from Gamma rays with the shortest wavelengths to radio waves at the longer-wavelength at the end of the spectrum. The present study focuses on the microwave spectrum, with EM wavelengths ranging from one meter to one millimeter. Most commonly, EM waves in this spectrum are referred to by their frequency, which is between 300 MHz (100 cm) and 300 GHz (0.1 cm).

1.3.2 Blackbody Radiation

The earth is considered an opaque surface, that is, when radiation strikes on the earth's surface, it is either absorbed or reflected away from it. An object that absorbs all incident EM radiation, regardless of frequency or angle of incidence, is called a "black body". It is an idealized physical body and does not exist in the natural world, however,

scientists often apply this concept of blackbodies when studying radiation theory. A blackbody is also an ideal and diffuse emitter, which emits the theoretical maximum radiation compared with any other objects at the same temperature and radiates the energy isotropically in all directions. The EM radiation emitted by a blackbody is described in Planck's law:

$$B_\lambda(\lambda, T) = \frac{2hc^2}{\lambda^5(e^{hc/k_B\lambda T}-1)} \tag{1.1}$$

where B_λ is the spectral radiance (units of radiative intensity per unit wavelength, or W• sr^{-1}•m^{-3}), h = 6.626 × 10^{-34} J/s is the Planck constant, k_B = 1.381 × 10^{-23} J/K is the Boltzmann constant, T is the blackbody temperature, and c = 3 × 10^8 m/s is the speed of light. Given the relative longer wavelength ($\lambda \geq 1$ mm) in the microwave spectrum, the exponential in the denominator of Planck's law can be approximated by its first order Taylor expansion, resulting in:

$$B_\lambda(T) \approx \frac{2ck_B}{\lambda^4} T \tag{1.2}$$

known as Rayleigh-Jeans approximation.

Figure 1.1 (a) displays the normalized blackbody emission spectra for the sun (6000 K) and the earth (288 K) as a function of wavelength. It is shown that for a given temperature, the blackbody radiance varies with different wavelengths. The relationship between the temperature (T) and the wavelength of maximum emission (λ_{max}) can be expressed as:

$$\lambda_{max} = \frac{2897}{T} \tag{1.3}$$

known as Wien's displacement law. With a higher temperature, the sun's emission

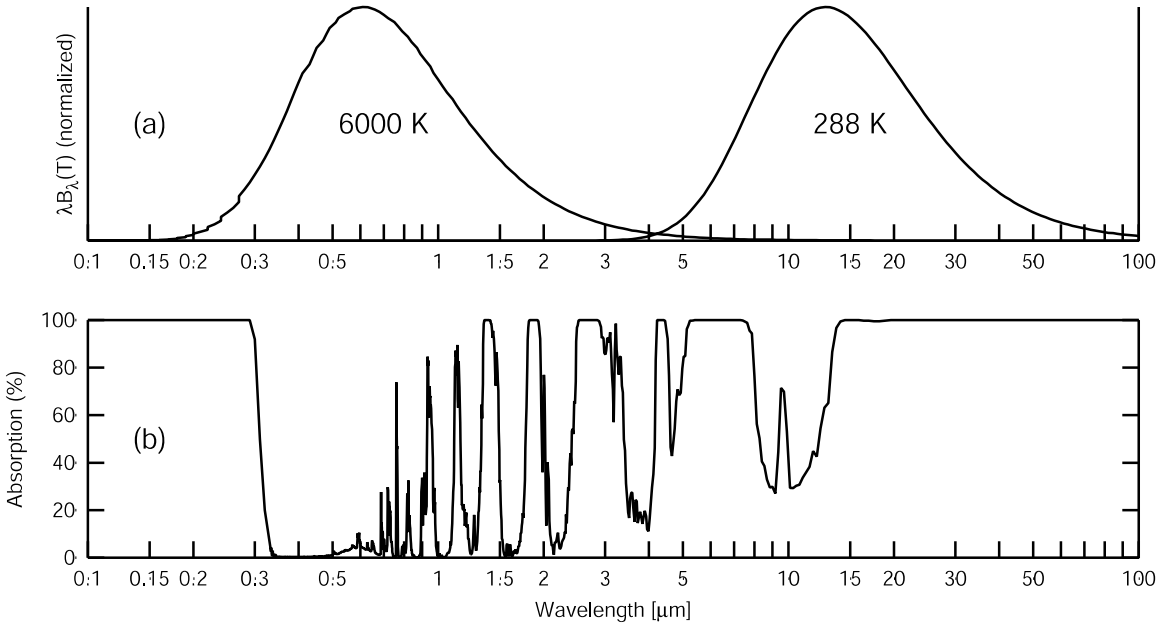

Figure 1.1: (a) The normalized spectral radiance corresponding to the approximate blackbody temperature of the sun and earth. (b) The absorption spectrum of the cloud-free atmosphere. Reprinted with permissions from *A First Course in Atmospheric Radiation, Second Edition,* G. W. Petty, p. 65.

spectrum peaks at a shorter wavelength compared with the earth. Therefore, the solar radiation is often referred to as “shortwave radiation” while the radiation from the earth is called “longwave radiation”.

The area under the Planck curve (Fig. 1.1a) represents the flux density (F) emitted by a blackbody, which can be derived by integrating the Planck's function over all wavelengths. This results in an expression called the Stefan-Boltzmann law:

$$F\ (T) = \ \sigma T^4 \tag{1.4}$$

where σ = 5.67 × 10^{-8} W• m^{-2}•K^{-4} is the Stefan-Boltzmann constant. Equation (1.4) indicates that an emitter with a higher (lower) temperature will emit higher (lower) energy radiation. Stefan-Boltzmann's function is strictly applied to blackbodies.

For imperfect emitters, also known as grey bodies, the corresponding flux intensity is a portion of the blackbody intensity, which follows:

$$F\ (T) = \ \varepsilon\sigma T^4 \tag{1.5}$$

Here, ε is the emissivity, defined as the ratio of what is emitted by an object to what would be emitted if the object were a blackbody. On the basis of the definition, it is easy to tell that $0 \ < \varepsilon < 1$ for a greybody. Similarly, absorptivity, *a*, is defined as the ratio of what is absorbed by an object to what would be absorbed if the object were a blackbody. Kirchhoff's law states that at thermal equilibrium, the emissivity of a body equals its absorptivity at a given wavelength:

$$\varepsilon_\lambda = a_\lambda \tag{1.6}$$

This implies that if a material is capable of absorbing a particular frequency, it will be a good emitter at the same frequency.

How can we apply the theory of blackbody radiation to the measurements from a satellite? Satellite sensors directly measure the spectral radiance, which is a function of a temperature the emitting object would have if it were behaving as a blackbody (Eq. 1.1). By inverting the Planck's law, the measured monochromatic radiative intensity (I_λ), or the

radiative intensity at a particular wavelength, can be easily converted to an equivalent blackbody temperature:

$$T_B = \left(\frac{hc}{k\lambda}\right) \frac{1}{ln\left[\frac{2hc^2\lambda^{-5}}{I_\lambda}+1\right]} \tag{1.7}$$

most commonly known as brightness temperature (T_B). The constants values are the same as in equation 1.1. If the observing object is close to a blackbody, the brightness temperature approximates to the object's physical temperature. In the infrared (IR) spectrum, the emissivity of most land and water surfaces and dense cloud layers is close to one, so $T_B \approx T$, where T is the actual physical temperature. In the microwave spectrum, using Rayleigh-Jeans approximation (Eq. 1.2), the relationship between the brightness temperature and the physical temperature reduces to:

$$T_B \approx \varepsilon T \tag{1.8}$$

1.4 Radiative Transfer Theory

1.4.1 Radiative Transfer Equation

Different from the earth, the atmosphere is a translucent medium. The EM radiation that strikes the atmosphere is not only absorbed or reflected, but is also transmitted. When a beam of EM radiation propagates through the atmosphere, part of the energy will be removed from the beam either by absorption or by scattering. Scattering refers to the change in direction of radiation when it interacts with the atmosphere. The combination of absorption and scattering is termed "attenuation" or "extinction". In the meantime, energy will be added into the beam through emission of the atmospheric constituents or scattering

from outside sources. Considering radiation with radiant intensity (I) passing through a layer of atmosphere with infinitesimal thickness *ds*, the change of I can be written as:

$$dI = dI_{ext} + dI_{emit} + dI_{scat} \tag{1.9}$$

The depletion that results from extinction, which includes both absorption and scattering, is given by:

$$dI_{ext} = -\beta_e I ds \tag{1.10}$$

where the extinction coefficient (β_e) is the sum of the absorption coefficient (β_a) and scattering coefficient (β_s). The second term on the right of equation 1.9 is the source from emission, written as:

$$dI_{emit} = \beta_a B(T) ds \tag{1.11}$$

where $B(T)$ is the Planck's function (Eq. 1.1). The source from radiation that is scattered from any direction θ' into the direction of the beam, θ, is given by:

$$dI_{scat} = \frac{\beta_s}{4\pi} \int_{4\pi} p(\theta', \theta) I(\theta') d\omega' ds \tag{1.12}$$

Here, the scattering phase function $p(\theta', \theta)$ yields the normalization condition:

$$\frac{1}{4\pi} \int_{4\pi} p(\theta', \theta) d\omega' = 1 \tag{1.13}$$

Combining all of the above equations (1.9,1.10,1.11,1.12), the complete differential form of the radiative transfer equation can be written as:

$$dI = -\beta_e I ds + \beta_a B(T) ds + \frac{\beta_s}{4\pi} \int_{4\pi} p(\theta', \theta) I(\theta') d\omega' ds \tag{1.14}$$

Given that the scattering source term (Eq. 1.12) complicates the calculation of the radiative transfer equation (Eq. 1.14), questions arises such as "when does scattering really matter?" and "can it be simplified under specific conditions?" The scattering coefficient and scattering phase function depend on the size, phase, and number of particles, of which the

size of a particle is the most important contributor. Generally, the source of scattering can be neglected for particles that are far smaller than the wavelength.

1.4.2 Rayleigh and Mie Theory

To indicate the relationship between the size of the particle and the wavelength of the radiation of interest, the dimensionless size parameter, *x*, is defined:

$$x = \frac{2\pi r}{\lambda} \tag{1.15}$$

where *r* is the radius of a spherical particle. According to the value of the size parameter, the scattering regimes are divided into four categories, as displayed in Figure 1.2. In the microwave spectrum, scattering from atmospheric particles smaller than cloud droplets is generally negligible ($\lambda \gg r$). Drizzle and raindrops are mostly included in the Rayleigh regime and larger particles such as hail falls in the Mie regime.

Rayleigh scattering is the scattering of the EM radiation by particles much smaller than the wavelength (*0.002 <x < 0.2*). Mathematically, the scattering (σ_s) and absorption cross-section[1] (σ_a) in Rayleigh regimes can simplify into:

$$\sigma_s = \frac{16\pi r^2}{3} x^4 \left|\frac{m^2-1}{m^2+2}\right|^2 \tag{1.16}$$

$$\sigma_a = 4\pi r^2 x Im\left\{\frac{m^2-1}{m^2+2}\right\} \tag{1.17}$$

where *x* is the size parameter, *I* is the radiative intensity, and *m* is the complex refractive index[2]. Recall the definition of the size parameter, it can be seen that the absorption cross-

[1] Cross section is analogous to the geometric area of a particle, which is used to determine how much radiation is removed from a given beam.
[2] Complex refractive index: the optical properties of the particle relative to the surrounding medium.

section is proportional to r^3 (Eq. 1.17) while the scattering cross-section is proportional to r^6 (Eq. 1.16). Therefore, the extinction cross-section approximates to the absorption cross-section, i.e. $\sigma_e \approx \sigma_a$. The Rayleigh scattering principle applies to particles in non-raining clouds with radius less than 100 μm. Equation 1.16 also implies that for Rayleigh scattering, the scattering efficiency, which is defined as:

$$K_\lambda\ (scattering) = \frac{\sigma_s}{\pi r^2} \tag{1.18}$$

is proportional to x^4, or $1/\lambda^4$. As shorter (blue) visible wavelengths are scattered more efficiently by atmospheric molecules, the sky appears blue,.

Mie theory is valid for particles similar to, or larger than the wavelength, i.e., $x \geq 1$. Different from Rayleigh scattering, the scattering efficiency (K_λ) in Mie regime exhibits a damped oscillatory behavior, as shown in Figure 1.3. The mean value of the scattering efficiency is around 2, which means that the effective scattering cross section is about twice the geometrical cross-sectional area. Mie scattering also differs from Rayleigh scattering in that Mie is generally independent of wavelength and preferential in the forward direction.

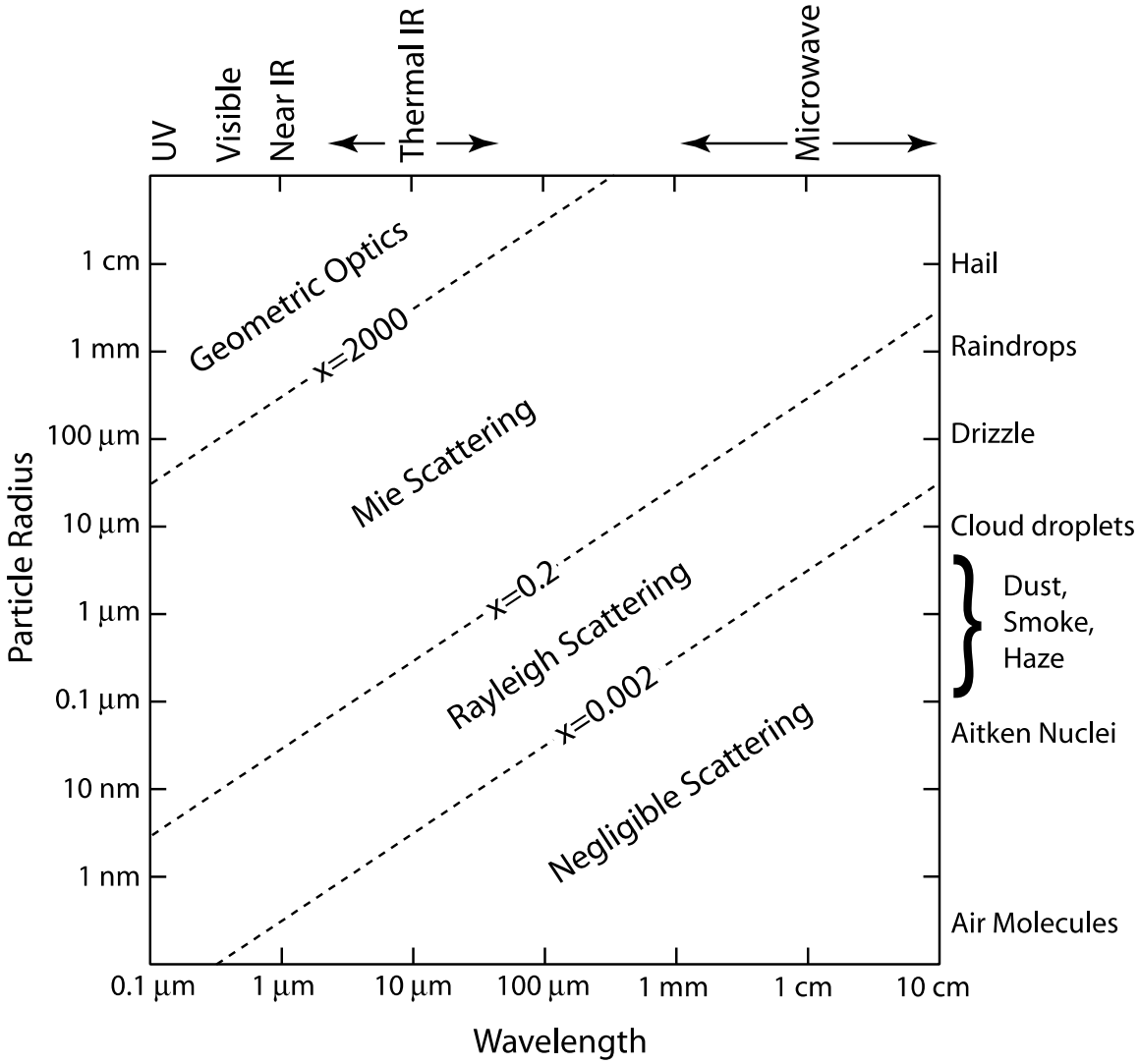

Figure 1.2: Relationship between particle size, radiation wavelength, and the size parameters for atmospheric particles. Reprinted with permissions from *A First Course in Atmospheric Radiation, Second Edition*, G. W. Petty, p. 346.

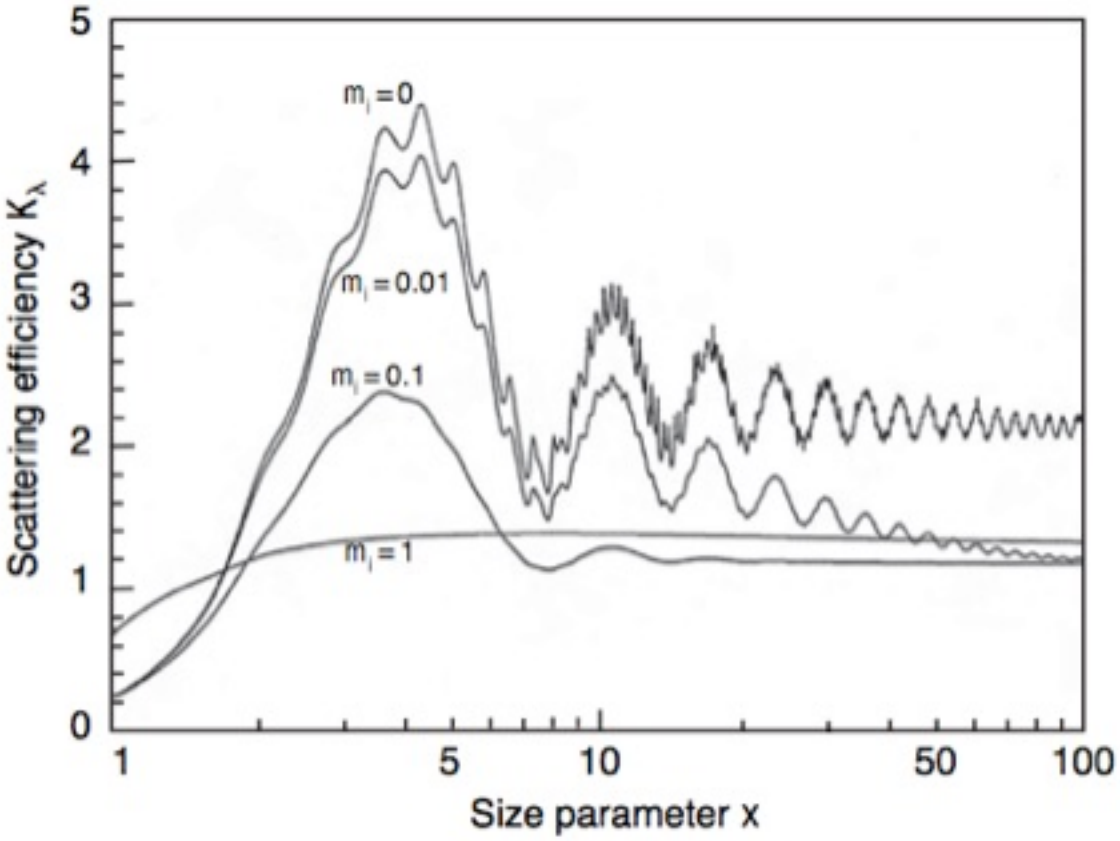

Figure 1.3: Scattering efficiency as a function of size parameter, plotted on logarithmic scale, for four different refractive indices. Reprinted with permission from *An Introduction to Atmospheric Radiation, Academic Press*, K. N. Liou, p. 191.

1.5 Passive Microwave Remote Sensing of Precipitation

Passive remote sensing (microwave radiometers in this case) measures EM energy radiated towards it from some target or area. Satellites following non sun-synchronous

orbits, which provide fairly good spatial resolution but low temporal resolution, usually carry microwave sensors. Depending on whether the scattering effect can be neglected or not, rainfall algorithms from microwave radiometers are generally divided into two categories: emission-based and scattering-based.

1.5.1 Emission-based algorithm

According to the discussion in the previous section, the ocean emits upwelling microwave radiation proportionally to its emissivity and temperature. The emissivity of ocean is uniformly low, around 0.5, making it appear much colder than its actual temperature. In contrast, raindrops have a relatively high emissivity and thus have a warm brightness temperature distinguishing it from the cold ocean surface. The difference between liquid hydrometeors and the ocean surface can be applied to estimate the rain rate. The greater the volume of rain, the larger the differences in corresponding brightness temperature. Note that the emission-based rainfall algorithm does not work properly over land because of the high emissivity of land surface.

Given that the emission-based rainfall algorithm is only applicable when scattering is not a big issue, it is commonly applied for microwave radiometers at low frequencies (i.e., large wavelength). For frequency less than 19 GHz (wavelength greater than 1.55 cm), the size parameter, x, which is proportional to $1/\lambda$ (or f), is small enough that almost all precipitation particles except large hails are in Rayleigh regimes (Fig. 1.2). Recall that the earth's Planck's curve peaks in the IR spectrum and decreases at longer wavelengths (Fig. 1.1a), a large field of view (FOV) is required for appropriate upwelling radiation, which will give rise to an systematic error, referred to as beam filling effects. The beam

filling effects will result in the underestimation of rainfall, especially in tropical regions, with more details discussed in the section 1.5.3.

1.5.2 Scattering-based algorithm

Scattering-based algorithm is applied for microwave radiometers at higher frequencies (greater than 37GHz), which is capable of inferring details of tropical convective systems due to higher resolutions. Namely, the scattering effect of frozen hydrometeors (ice crystals, hail, and graupel) in these channels is not negligible. Specifically, scattering in this case refers to the process when the upwelling radiation is deflected away from the microwave sensors by atmospheric hydrometers.

It is found that the brightness temperature is depressed markedly by the existence of frozen hydrometers at the 37 GHz and 85 GHz channels (Wu and Weinman, 1984; Kummerow and Weinman, 1988). For these channels, cloud and precipitation particles fall in Mie scattering regimes. As discussed above, Mie scattering is strongly dependent on the relationship between the scattering efficiency and the size parameter (Fig. 1.3). At the 37 GHz channel, only large, millimeter-sized ice particles scatter strongly. In other words, the significant depression of brightness temperature only occur when there is large hail and/or graupel. The 85 GHz, however, is more sensitive to smaller particles, on the order of 0.1 mm. Even the presence of small ice particles or snow crystals can sufficiently decrease the measured brightness temperature. Since the scattering-based algorithm largely relies on the scattering effect of frozen hydrometers, any raining system that does not reach the freezing level (i.e., warm rain) is not detectable. The scattering-based algorithm works both over land and over ocean.

1.5.3 Beam Filling Effects

As implied in the above section, the microwave radiometer measures an average brightness temperature, T_B, within the whole field of view (FOV) or the foot print size, and then converts it into an average rain rate. However, since the relationship between the T_B and rainrate are non-linear (Wilheit et al. 1977), when the microwave radiometer's field of view (FOV) is not filled with a uniform rain rate, a systematic error will occur. This so-called beam filling effects causes the underestimation of rain rate over a large FOV. Correcting the rainfall estimation for beam filling effects is necessary for the space-based microwave observations, as their FOV is usually larger than the typical size of rain cells, which is about 1-2 km. The difference between the retrieved rain rate and the actual rain rate can range from 30% to 50% without corrections. The magnitude of beam filling error for a specific instrument largely depends upon its FOV. The higher the spatial resolutions, the less the beam filling effects. Therefore, radiometers at lower frequencies would have more severe beam filling problems compared with higher frequencies, as a result of larger FOV.

1.6 Active Microwave Remote Sensing of Precipitation

Active remote sensing, often referred to as radar, transmits EM pulses at known frequencies and measures the strength of the returned backscattering from cloud and precipitation particles. Clouds are usually not detectable by most weather radars, as the radar echoes from clouds are very weak. But radars can detect rain and hails very easily,

which makes them extremely useful for detecting local severe storms, mesoscale convective complexes, tornadoes and TCs.

1.6.1 Radar Equations for Distributed Targets

The radar observes many raindrops or cloud particles at the same time, so the power returned to the radar are the combination of the returns from all of the individual targets within the radar beam. Mathematically, this can be expressed as:

$$\sigma_t = \sum_{i=1}^{n} \sigma_i \tag{1.19}$$

Here, σ_i is the individual backscattering cross-sectional area for all *n* particles, and σ_t is the total backscattering cross-sectional area of a meteorological target. The backscattering cross-sectional area of a target depends on the size, shape, kind of matter making up the target, and the wavelength of the radar viewing it. For most meteorological radars (wavelengths of 3 cm or larger), almost all precipitation hydrometeors can be considered small compared to the wavelength, where the Rayleigh approximation yields. Thus, the backscattering cross-sectional area of the i^{th} sphere, σ_i, can be simplified as:

$$\sigma_i = \frac{\pi^5 D^6}{\lambda^4} \left| \frac{m^2-1}{m^2+2} \right|^2 \tag{1.20}$$

where *D* is the diameter of a spherical target.

Another way to calculate the total backscattering cross-sectional area of targets (σ_t) is to multiply the backscattering cross-sectional area of a *unit* volume by the total sample volume (*V*), which is given by:

$$\sigma_t = V \sum_{vol} \sigma_i \tag{1.21}$$

Here, $\sum_{vol} \sigma_i$ is the summation of the individual backscattering cross-sectional area over a *unit* volume, most commonly known as radar reflectivity, η. For Rayleigh scattering, the radar reflectivity is expressed by:

$$\eta = \frac{\pi^5}{\lambda^4} \left| \frac{m^2 - 1}{m^2 + 2} \right|^2 z \tag{1.22}$$

Here, *z* is called the radar reflectivity factor, defined as:

$$z = \sum_{vol} D^6 = \int_0^\infty N(D) D^6 dD \tag{1.23}$$

where *N(D)* is the function of the drop size distribution (DSD).

One of the advantages of using the radar reflectivity factor, *z*, instead of radar reflectivity, η, is that the radar reflectivity factor only depends upon the number and sizes of the raindrops and is independent of the wavelength of the radar. The term "reflectivity" used in this study represents "radar reflectivity factor". Reflectivity can range from very small values such as in fog ($\sim 0.001 mm^6/m^3$) to very large values such as in very large hail ($> 30{,}000{,}000\ mm^6/m^3$). For this reason, the logarithmic radar reflectivity, *Z*, is more commonly used in meteorology, which follows:

$$Z = 10 log_{10} \left(\frac{z}{1 mm^6/m^3} \right) \tag{1.24}$$

where *Z* is measured in units of dBZ (decibels relative to a reflectivity of 1 mm^6/m^3) and *z* is the linear radar reflectivity factor in mm^6/m^3. Typical weather radar measures reflectivity ranging from -20 to 70 dBZ.

1.6.2 Radar Rainfall Retrieval

If all of the parameters associated with specific radar are combined together as a constant, *c*, the amount of energy detected by the radar, P_r, can reduces to

$$P_r = \frac{c|K|^2 z}{r^2} \tag{1.24}$$

Here, $|K|$ is the magnitude of the parameter related to the complex index of refraction, and is given by

$$K = \frac{m^2-1}{m^2+2} \tag{1.25}$$

The value of $|K|^2$ most significantly depends upon the kind of material of a target. Generally, $|K|^2$ is 0.93 for water and 0.20 for ice particles.

From equation 1.24, it can be seen that the power returned to the radar is a function of the radar reflectivity factor, which in turn, is dependent upon the number and diameters (6^{th} power) of the raindrops present in the radar's sample volume (Eq. 1.23). Rainrate is also dependent upon the number and diameters (3^{th} power) of the raindrops as well as their terminal velocities. The relationship between radar reflectivity factor (z) and rainrate (R, in mm/h) is called the Z-R relationship, which can be expressed by

$$z = aR^b \tag{1.26}$$

where a and b are empirical constants for a specific DSD. Since DSD varies with different environmental conditions and precipitation types, there are diverse experimentally determined Z-D relationships. The most commonly used Z-R relationship is $z = 200R^{1.6}$, based on the Marshall-Palmer DSD model. The TRMM Precipitation Radar (PR) applies different empirically derived DSD models for convective and stratiform rain.

1.6.3 Rain Attenuation

As discussed in section 1.4.1, an amount of energy will be removed from the original beam of EM radiation when passing through any medium (the atmosphere in this case).

This interaction between the beam and atmospheric constituents, referred to as attenuation, is dependent upon the kind of material present and its density. Attenuation in the cloud- and precipitation-free atmosphere is generally negligible, however, it should be carefully considered in the situation of rain. Radars with shorter wavelengths (i.e., higher frequencies) are more capable of detecting smaller particles, but they are also associated with higher attenuation rates. For example, the attenuation rates for X-band radars are high enough to cause severe attenuation in thunderstorms. The frequency of the TRMM precipitation radar (PR) falls in the K_u band (12-18 GHz), where attenuation correction is important for heavy rain (Iguchi et al. 2000).

1.7 TRMM Satellite

The Tropical Rainfall Measuring Mission (TRMM) satellite, a joint mission between the United States and Japan, was primarily proposed to provide precise measurement of rainfall over global tropical and subtropical regions, where more than two-thirds of global precipitation occurs (Simpson et al. 1988). It TRMM came to an end in April, 2015 and through 17+ years since launched, it has been proven to be extremely useful for rainfall and climate research. Figure 1.4 illustrates the scan geometries of the Precipitation Radar (PR), TRMM Microwave Imager (TMI), and Visible and Infrared Radiometer System (VIRS) onboard the TRMM satellite. These instruments are designed to obtain rainfall and other relevant information such as rain type, height of the bright band, cloud type, cloud top height, etc.

1.7.1 Precipitation Radar

The TRMM Precipitation Radar (PR) is a 13.8 GHz (wavelength of 2.17 cm) electronically scanning radar that constructs a three dimensional observation of precipitation along its path. It is also the first space-borne radar, with the vertical resolution of 250 m from the surface up to a height of 20 km. The TRMM satellite was boosted in August, 2001 to extend its lifetime. In the meantime, the width of PR swath increased to 247 km (215 km before boost) and the horizontal resolution enlarged to approximately 5 × 5 km (4 × 4 km before boost). The PR scans nadir with the cross-track scanning angle ranging from -17^{o} to $+17^{o}$. The minimum detectable signal is around 17-18 dBZ, which corresponds to a rain rate around 0.25 mm/hr. The PR can also be applied to estimate the liquid water concentration and the latent heating rate that results with the condensing water vapor (Tao et al., 2006).

1.7.2 Microwave Imager

The TRMM Microwave Imager (TMI) is a nine-channel passive microwave radiometer, operating at frequencies of 10.65 GHz, 19.35 GHz, 21.3 GHz, 37.0 GHz and 85.5 GHz. Dual polarization at all frequencies except 21.3 GHz, which is vertically polarized only. The TMI has an 878 km swath width (760 km before boost in 2001) and

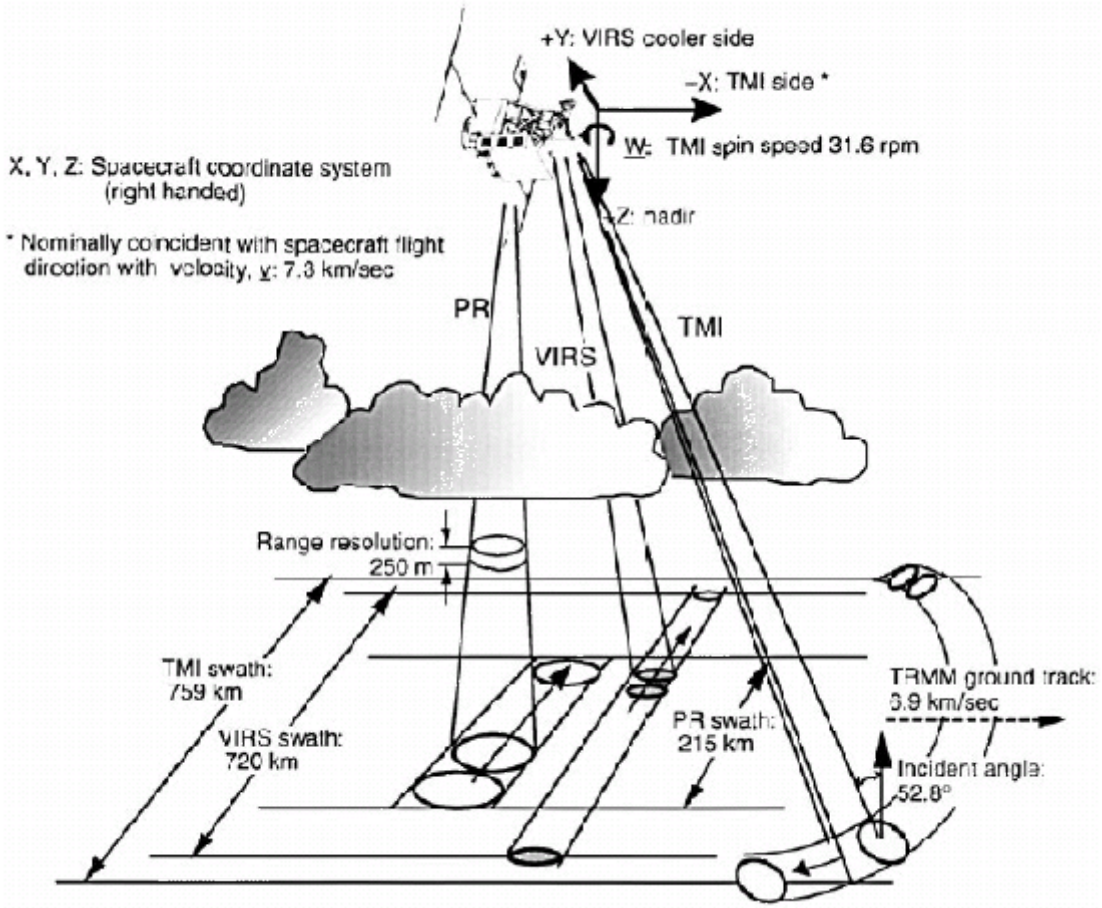

Figure 1.4: A schematic view of the scan geometries of the TRMM PR, TMI, and VIRS (Kummerow et al. 1998).

views the earth at a 52.8^{o} conical angle (Fig. 1.4). To distinguish the ambiguity between low brightness temperatures due to ice scattering and those due to low surface emissivity, Spencer et al. (1989) derived Polarized corrected Brightness Temperature (PCT) for 85 GHz and 37 GHz channels as:

$$PCT_{85} = 1.8T_{85v} - 0.8T_{85h} \quad (1.27)$$

$$PCT_{37} = 2.2T_{37v} - 1.2T_{37h} \quad (1.28)$$

where T_v, T_h are the vertically and horizontally polarized bright temperature for 85GHz and 37 GHz, respectively. The constants are derived empirically from models. The PCT can be used as a proxy for rain rate and for convective intensity. The FOV for 37 GHz is 16 × 9 km and the FOV for 85 GHz is 7 × 5 km.

1.8 Outline

This dissertation consists of two main sections, each of which addresses separate but related issues involving the distributions and properties of overshooting convection, defined with TRMM precipitation radar, in TCs. The first section (chapter 2) uses a global database of TCs over ocean to study the geographical and seasonal variations of overshooting convection in TCs. The distribution and overshooting properties of overshooting convection is also examined for different TC regions, intensities and intensity change stages. The second section (chapter 3) focuses on the rapid intensification of TCs. The role of overshooting convection in rapidly intensifying TCs is compared with three other kinds of precipitation/convection. Both the percent occurrence of various kinds of precipitation/convection and their relative contribution to total volumetric rain and total latent heating are statistically quantified.

2. GLOBAL DISTRIBUTION OF HOT TOWERS IN TROPICAL CYCLONES BASED ON 11-YR TRMM DATA

2.1 Abstract

Global distribution of hot towers in tropical cyclones (TCs) is statistically quantified using an 11-yr Tropical Rainfall Measuring Mission (TRMM) Tropical Cyclone Precipitation Feature (TCPF) database. From 6003 individual TRMM overpasses of 869 TCs, about 1.6% of TC convective systems are found to penetrate 14 km and about 0.1% of them even reach the 380-K potential temperature level. Among six TC-prone basins, the highest population of TC convective systems and those with hot towers are found over the northwest Pacific (NWP) basin. However, the greatest percentage of TCPFs that are hot towers [overshooting TCPFs (OTCPFs)] is found over the North Indian Ocean basin. Larger overshooting distance and ice mass are also found in this basin. The monthly variation of OTCPFs resembles that of TC activities in each basin. The percentage of OTCPFs is much higher in the inner core (IC) region (10%) than that in the inner rainband (IB; 2%) and outer rainband (OB; 1%) regions. OTCPFs in the IC region have much larger overshooting distance, area, volume, and ice mass than those in the IB and OB regions. The percentage of OTCPFs in the IC region increases as both TC intensity and intensification rate increase. About 17% of IC features in rapidly intensifying storms penetrate over 14 km, while the percentage is down to 11% for slowly intensifying, 9% for neutral, and 8% for weakening storms. A very good linear relationship is found between TC intensification rate and the percentage of TCPFs that are hot towers in the IC region.

2.2 Introduction

Hot towers are horizontally small, deep tropical cumulonimbus clouds with intense rapidly rising cores that reach or penetrate the tropopause. Several decades of studies have shown that they play a crucial role on the maintenance of global circulation (Yulaeva et al. 1994; Rosenlof 1995). They are also an essential agent for heat and moisture transportation (Riehl and Malkus 1958; Simpson 1990) as well as mass exchange between tropopause and stratosphere (Holton et al. 1995; Dessler 2002).

In the past decades, radar, passive microwave, and infrared (IR) observations have been used to investigate the geophysical, seasonal, and diurnal distribution of deep convection in the tropics (Hall and Vonder Haar 1999; Petersen and Rutledge 2001; Gettelman et al. 2002; Jiang et al. 2004; Liu and Zipser 2005, hereafter LZ05). Based on IR and visible satellite data, deep convective clouds were identified using a -65^{o}C cloud-top brightness temperature threshold, and the diurnal cycle of west Pacific deep convection was examined by Hall and Vonder Haar (1999), who noted that ‘‘the diurnal cycle of deep convective cloud is driven by the internal variation of large clusters.’’ Based on IR brightness temperatures from satellites and contemporaneous reanalysis temperatures, Gettelman et al. (2002) found out that convection penetrating the tropopause is most common in Northern Hemisphere winter globally, while regionally the strongest and deepest convection is found over the central and western Pacific in February and over the Indian monsoon in August. Also, a relationship between cold tropopause temperatures and deep convection is discovered: convection penetrates most frequently at the places where the tropopause is coldest. LZ05 studied the common properties of global deep convection

penetrating the tropical tropopause and noted that overshooting convection is much more frequent over land than over ocean, and the most in- tense deep tropical convection was detected over central Africa using a 5-yr Tropical Rainfall Measurement Mission (TRMM) database.

However, existing studies mostly focused on deep convection in general convective systems. Since there are moist ascents regions within tropical cyclones (TCs), an interesting question in TC research is whether these deep convective systems in TCs are subject to a different amount of entrainment drying compared with other mesoscale systems. Romps and Kuang (2009) examined deep convection penetrating the tropopause in TCs using 23 years of satellite IR, best-track, and reanalysis data. In their study, an overshooting cloud is identified when its infrared brightness temperature is below the monthly averaged tropopause temperature. They suggested a disproportionate percentage of global over- shooting cloud tops occurred in TCs.

On the other hand, some previous studies suggested that hot towers occurring within the inner core region are related to the intensification of TCs (Hendricks et al. 2004; Kelley et al. 2004, 2005; Montgomery et al. 2006; Houze et al. 2009; Jiang 2012). Kelley et al. (2004), using 6 years of the well-centered overflights of TCs observed by the TRMM precipitation radar (PR), argued that the chance of TC intensification increases when one or more tall precipitation cells exist in the eyewall. An extremely tall convective tower in their study is identified when the 20-dBZ reflectivity signal reaches or penetrates 14.5 km. Hendricks et al. (2004) analyzed a high-resolution near-cloud-resolving numerical simulation of Hurricane Diana (1984). They demonstrated that the cores of deep

cumulonimbus convection possessing strong vertical vorticity (they called these ‘‘vortical hot towers’’) are the preferred mode of convection and they are of great importance in the formation of the tropical storms via a two-stage process. Montgomery et al. (2006), using a nonhydrostatic cloud mode, examined the role of vortical hot towers in the process of transforming a midtropospheric cyclonic vortex into a warm core tropical depression. They proposed that these intense vortical hot towers may initiate TC genesis. Using 11 years of TRMM data, Jiang (2012) examined the hypothesis of hot towers in the inner core as an indicator of RI. In her study, hot towers are defined when the 20-dBZ radar echo height is at or above 14.5 km. She found that for samples with hot towers in the inner core, the probabilities of rapid intensification (RI) and slow intensification (SI) increase, but hot towers are neither a necessary nor a sufficient condition for RI.

With the first-ever satellite-based precipitation radar, TRMM is not only invaluable for global precipitation estimates (Adler et al. 2000; Schumacher and Houze 2003); it also can be used to quantify the properties of cloud systems and their distributions throughout the global tropics (Nesbitt et al. 2000; Cecil et al. 2002, 2005). In this study, the global distribution of hot towers in TCs is quantified using 11-yr TRMM data. There are two main goals of this study. The first goal is to examine how hot towers in TCs are distributed geographically and seasonally and to determine the fraction of hot towers out of total TC convective systems. The second goal is to find out the distribution of hot towers in different TC regions, intensities, and intensity change stages. In addition, the overshooting distance, area, volume, mass, and convective proxies of hot towers in TCs are examined. The key questions to be addressed are the following: 1) what are the geographical distribution of

population and overshooting properties of hot towers in TCs? Is the overshooting activity more frequent and intense over the northwest Pacific basin? 2) What are the patterns of seasonal variation of population and overshooting properties of hot towers in TCs? 3) How are hot towers distributed in different TC regions? Is overshooting convection most intense in the inner core region? 4) Are hot towers within the inner core region related to TC intensity and intensity change? In section 2.3, the data and methodology applied to identify hot towers in TCs and selected overshooting properties used in this study are described. Section 2.4 examines the geographical and seasonal distribution of population and overshooting properties of precipitating systems with hot towers. The distribution of population and overshooting properties for hot towers in different TC regions, TC intensities, and TC intensity change categories are discussed in section 2.5. Convective properties of hot towers are analyzed in section 2.6, and the conclusion is presented in section 2.7.

2.3 Data and Methodology

2.3.1 TRMM TCPF database

The data for this study include 11-yr (January 1998– December 2000 and January 2002–December 2009) observations by TRMM. In August 2001, the altitude of TRMM satellite was boosted from 350 to 402 km to lengthen its lifetime in orbit. Considering that the quality of radar data is questionable during the orbit boost, we exclude the data from year 2001. Grouping continuous pixels satisfying certain criteria into precipitation features

(PFs), a University of Utah (UU) TRMM database has been built (Nesbitt et al. 2000; Liu et al. 2008) and successfully applied to many global and regional climatological studies (Cecil et al. 2002, 2005; Zipser et al. 2006). Currently, three levels of processing of the TRMM data are constructed in the database, including various TRMM observed properties such as feature size, mean rain rate, maximum 20-dBZ height, etc. The environmental sounding for each PF are obtained by interpolation from 6-h interval National Centers for Environmental Prediction (NCEP) reanalysis data described by Kistler et al. (2001).

To focus on TCs specifically, a TC subset of the UU TRMM PF database based on the collaboration between Florida International University (FIU) and UU has been generated (Jiang et al. 2011). This FIU–UU TRMM TC precipitation, cloud, and convective cell feature (TCPF) database is built by interpolating the global TC best-track data into the UU TRMM PF database. A TCPF is identified when the distance between TC center and the TRMM PF center is within 500 km. Besides existing TRMM observed properties in the UU TRMM PF database, a series of storm- related parameters are calculated and linearly interpolated into TRMM observation time—for example, land–ocean flags of TC center, storm 12-, 24-, 36-, and 48-h future intensity changes, etc. Furthermore, based on this FIU-UU TRMM TCPF database, three subregions— the inner core (IC), inner rainband (IB), and outer rainband (OB)—are subjectively sorted for each individual TRMM TC overpass (Jiang et al. 2013).

This study uses the TRMM TCPF database to identify TC convective systems. The comprehensive database contains 13 precipitation feature definitions based on different grouping criteria [see Jiang et al. (2011) for details]. In this study, each TCPF is grouped

by contiguous pixels with TRMM PR 2A25 (Iguchi et al. 2000) near-surface rain rate greater than zero. To minimize noise, the minimum near-surface four adjacent pixels with rain rate greater than zero (about 80 km2) were required for every TCPF. Here, we only consider TCPFs over ocean. As a result, more than 150 000 TCPFs were found within the 11-yr period from 6003 individual TRMM overpasses of 869 TCs. The TRMM observation is between 368S and 368N. Six TC-prone basins are considered in this study following Jiang and Zipser (2010): Atlantic (ATL), east central Pacific (EPA), northwest Pacific (NWP), North Indian Ocean (NIO), South Indian Ocean (SIO), and South Pacific (SPA).

2.3.2 Methodology of defining Hot Towers in TCPFs and selection of Overshooting properties

Five reference heights are selected to identify TCPFs with overshooting tops (OTCPFs; i.e., hot towers), following the criteria of LZ05. These include 1) 14 km, 2) level of NCEP reanalysis tropopause (Z_{trop}), 3) level of potential temperature u equal to 380 K (Z_{380K}) calculated from NCEP sounding, 4) level of neutral buoyancy (LNB) calculated using NCEP soundings and surface equivalent potential temperature θ_e (LNB_{sfc}), and 5) level of neutral buoyancy calculated using θ_e at 925 and 1000 mb, whichever is greater ($LNB_{925\&1000}$). Then OTCPFs are found from 150,000 TCPFs when the maximum 20-dBZ echo height observed by TRMM PR exceeds above-mentioned reference heights respectively. Therefore, one TCPF represents one precipitating system in TCs and one OTCPF represents one hot tower in TCs in this study. As pointed out by LZ05, OTCPFs

defined here are representing the area of large ice particles lifted above the reference heights by strong updrafts in convective cores. Unlike using the IR and cloud radar data, anvils clouds with small ice particles are not detectable by the PR and are not included in this study.

To describe overshooting properties of hot towers in TCs, four overshooting parameters (i.e., overshooting distance, area, volume, and precipitating ice mass) are selected and calculated for each OTCPF using the same method as LZ05. The overshooting distance for each OTCPF refers to the distance between the maximum height of 20 dBZ and the reference height. The over- shooting area of each OTCPF is calculated by multi-plying the total number of pixels with PR reflectivity greater than 20 dBZ by the size of each pixel at the reference level. Similarly, the overshooting volume and ice mass for each OTCPF are calculated by integrating the volume and precipitating ice mass of overshooting pixels above the reference height.

Table 2.1 displays the characteristics, such as population, mean overshooting distance, and overshooting area of the identified OTCPFs based on five different reference heights. The mean reference heights in TCs over oceanic regions between 36^{o}S and 36^{o}N as shown in Table 2.1 are similar to those for general tropical regions between 20^{o}S and 20^{o}N presented in LZ05. Of the five definitions for OTCPF, the mean Z_{380k} is

Table 2.1: Population, overshooting distance, and area of OTCPFs identified with respect to 5 different reference heights.

Reference heights	14km	LNB_{sfc}	$LNB_{925\&1000}$	Z_{trop}	Z_{380K}
OTCPFs population (#)	2368	1185	464	295	137

Number of orbits (#)	1690	939	388	277	130
Number of TCs (#)	686	493	268	227	119
Population percentage (%)	1.59	0.79	0.31	0.20	0.09
Mean reference height (km)	14.00	14.73	14.45	16.39	16.91
Mean Z_{20dBZ} (km)	15.29	15.88	15.80	17.20	17.91
Mean overshooting distance (km)	1.29	1.16	1.34	0.81	1.00
Mean OTCPFs overshooting area (km^2)	278	287	297	225	221
Mean overshooting area/OTCPF raining area (%)	7.45	9.53	7.65	5.40	8.47
Total overshooting area/total raining area (%)	0.32	0.17	0.07	0.03	0.01

the highest at 16.9 km. From a total of 150,313 TCPFs, 1.59% of them have 20-dBZ radar echoes at or above 14 km, while only 0.09% of TCPFs are found reaching the level of potential temperature equal to 380 K.

Compared with LZ05's result of 1.38% overshooting PFs for the 14-km reference height, the percentage of OTCPFs is slightly higher. The mean overshooting distance of OTCPFs for the 14-km reference height is 1.29 km, slightly lower than that for general overshooting PFs presented in LZ05. However, the mean overshooting distance of overshooting above 14 km from these OTCPFs. LZ05 found that when higher reference heights were used, the PFs tend to have a larger overshooting area and smaller raining area. This is not the case for TCPFs. The difference is due to isolated severe convective storms over land included in LZ05's dataset.

Figure 2.1 demonstrates the locations of OTCPFs for different reference heights. The pattern of geographical distribution of OTCPFs shows little sensitivity to different reference heights. This is also the case when examining overshooting properties. Also

shown in Figure 2.1 are the lightning properties of the OTCPFs, where the red represents the OTCPFs with lightning, and blue are for the OTCPFs without lightning. When higher reference heights are used, fewer OTCPFs with lightning are detected. It is found that over 66% of OTCPFs have lightning when using 14 km as a reference level. And this percentage decreases to 48% for TCPFs reaching the level of 380 K potential temperature. Considering the smaller numbers of OTCPFs when using higher reference heights, in this study, the 14-km reference height is applied to examine the global and seasonal distributions of OTCPFs in different TC regions, intensity and intensity change stages. Therefore, in total, 2368 OTCPFs from 1690 TRMM overpasses of 686 TCs are included in the rest of the study.

2.4 Geographical and seasonal distribution of population and overshooting properties of OTCPFs

2.4.1 Geographical distribution

The geographical distributions of populations of total TCPFs, TCPFs without hot towers, OTCPFs, and the fraction of TCPFs that are hot towers are presented in Figure 2.2. To create this plot, populations of TCPFs, TCPFs without hot towers, OTCPFs, and the fraction of OTCPFs are summed into $5^{o}\times5^{o}$ longitude-latitude grid boxes. The general

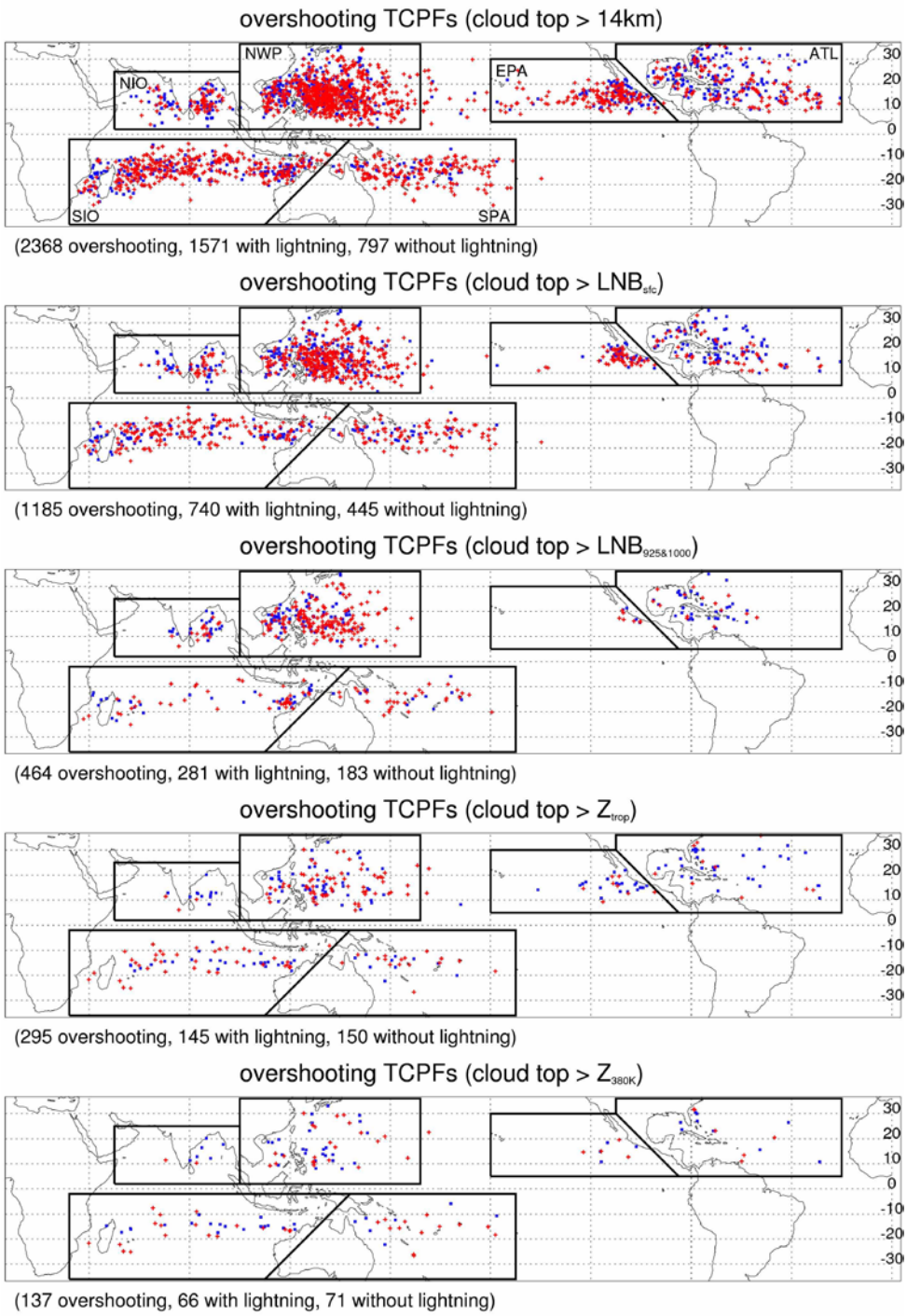

Figure 2.1: Location of identified OTCPFs at 36^{o}N-36^{o}S using different reference heights. The OTCPFs with lightning are shown in red, and the OTCPFs without lightning are shown in blue.

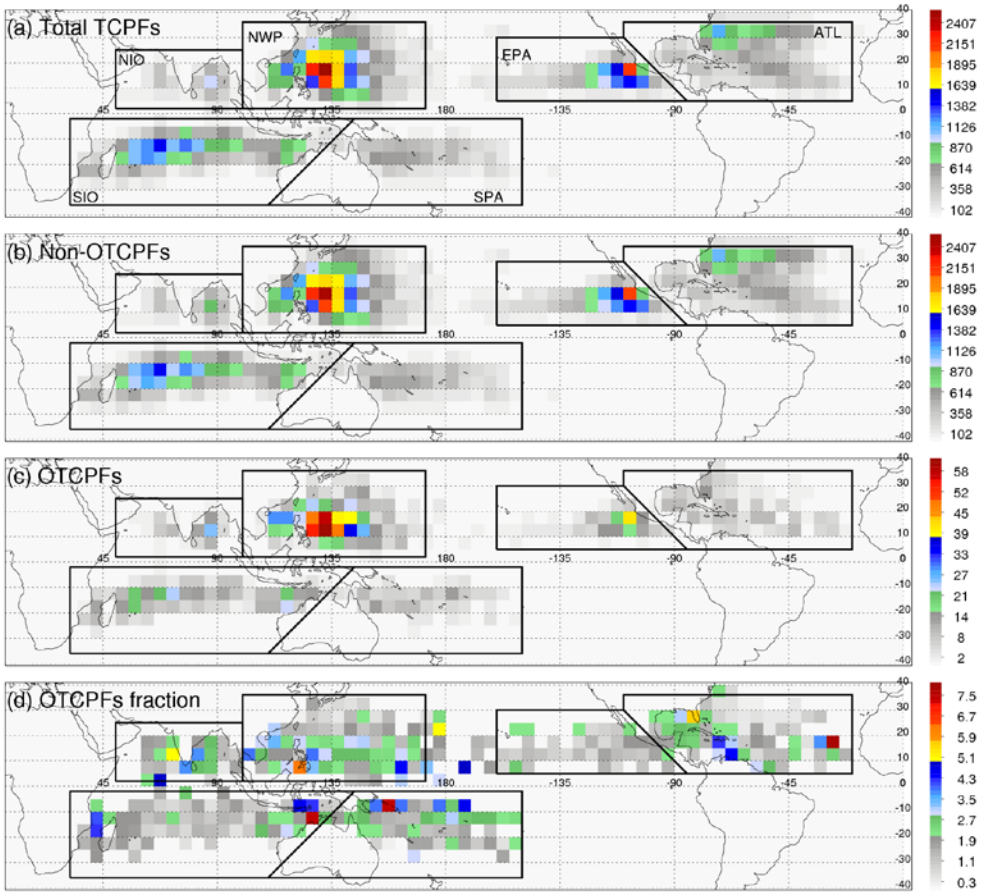

Figure 2.2: Global distribution of (a) population of total TCPFs [#], (b) population of TCPFs without hot towers [#], (c) population of OTCPFs [#], and (d) OTCPFs fraction [%] based on 5^{o} x 5^{o} grid for the years of 1998-2000 and 2002-09. Borders of six basins (ATL, EPA, NWP, NIO, SIO, and SPA) are indicated.

distribution pattern and locations of highest number concentration of total TCPFs (Fig. 2.2a) and TCPFs without hot towers (Fig. 2.2b) are very similar, indicating that majority of total TCPFs do not penetrate the 14 km height. Precipitation and convective systems in TCs have the highest number population in the NWP basin over a large area east of the Philippine Islands, followed by a smaller area in the EPA south of Baja California. Moderate number concentrations of TCPFs are seen in the SIO basin between 10°S and 20°S east of Madagascar Island and northwest coast of Australia and in the ATL basin near the east coast of the US between 20°N and 30°N. The overall pattern is very similar to the patterns of global TC number density, accumulated cyclone energy (ACE), and precipitation presented in Jiang and Zipser (2010).

The geographical distribution of population of OTCPFs (Fig. 2.2c) is similar to that of total TCPFs (Fig. 2.2a) and TCPFs without hot towers (Fig. 2.2b). The highest concentration of OTCPFs is over NWP and EPA around the same locations as in total TCPFs. Moderate number concentrations of OTCPFs are also seen in the SIO basin between 10°S and 20°S east of Madagascar Island and northwest coast of Australia. But unlike total TCPFs, the population of OTCPFs across the whole ATL basin is relatively low. Consistent with the results here, previous studies have shown that the deepest and strongest oceanic tropical convection (Gettelman et al., 2002; LZ05) and TC convection (Jiang et al. 2011) are most common over NWP according to IR, radar, and 85 GHz passive microwave measurements. Several previous studies from the perspective of large-scale environmental factors also indicate that NWP has higher SST, lower wind shear (Gary

1968), higher Convective Available Potential Energy (CAPE) and LNB (Liu et al., 2007), and therefore is more favorable for development of both TC and deep convection.

It is reasonable that OTCPFs concentrate over the places where precipitation and convective systems in TCs occur most frequently. The fraction of TCPFs that are hot towers is calculated for each $5^o \times 5^o$ grid boxes, and its distribution is shown in Figure 2.2d. This plot gives us information about where TCPFs have higher opportunity to penetrate over 14 km. The pattern shown in Figure 2.2d is very different from the distribution of population of TCPFs and OTCPFs seen in Figure 2.2a-c. Higher fractions seem randomly scattered over the map, although there are several high values near the coastal regions.

Table 2.2 shows the population of TCPFs, TCPFs without hot towers, and OTCPFs, and the overall percentage of TCPFs that are hot towers in six TC basins. After dividing the total number of OTCPFs by the population of TCPFs in each basin, it is found that hot towers contribute, respectively, 2.10%, 1.96%, 1.66%, 1.47%, 1.20% and 1.13% of TCPFs in NIO, NWP, SPA, SIO, EPA, and ATL. NIO has the highest

Table 2.2: Population of TCPFs, TCPFs without hot towers, OTCPFs and fraction of OTCPFs in different TC basins.

Basin	ATL	EPA	NWP	NIO	SIO	SPA	Total
# TCPFs	26697	20751	49019	6040	34681	13125	150313
# non-OTCPFs	26394	20501	48060	5913	34170	12907	147945
# OTCPFs	303	250	959	127	511	218	2368
% OTCPFs	1.13	1.20	1.96	2.10	1.47	1.66	1.58

percentage of OTCPFs, although populations of both total TCPFs and OTCPFs are low in this basin. NWP has the second highest percentage, just slightly lower than that in NIO.

Also, the height of tropopause in the NIO basin is the lowest among six TC-prone basins with a mean value of 13.4 km, indicating that the highest percentage of OTCPFs found in the NIO basin is not because of a higher tropopause.

The cumulative distribution functions (CDFs) of overshooting distance and ice mass for each TC-prone basin are presented in Figure 2.3. From Figure 2.3a, it can be seen that OTCPFs over the NIO basin have the greatest overshooting distance, followed by SIO, NWP, SPA, EPA, and ATL basins. The difference of the median overshooting distances between OTCPFs in NIO and ATL basins is about 0.5 km. The distributions separate into roughly two groups, with higher overshooting distances in NIO, SIO, NWP and SPA and smaller distances in ATL and EPA. As for the overshooting ice mass (Fig. 2.3b), it can be seen clearly that these properties are the highest for OTCPFs in the NIO basin, while the differences among other five TC basins are small. Note that unlike overshooting distance, the overshooting ice mass not only depends on the overshooting convection itself but is also related to the size of the extremely deep convective systems.

Significance tests[3] have been done to determine the significant levels of the mean values for each overshooting parameter in six TC basins. It is shown that statistically significant differences exist among different TC basins for overshooting distance at the 99% level while for overshooting ice mass at the 95% level. For overshooting area and volume, none of the differences among various TC basins is significant (not shown). From

[3] A one-way analysis of variance (function KW_TEST in Interactive Data Language (IDL) version 8.0) has been applied to Figures 3, 4, 5, 7 and 9 to test the hypothesis that three or more sample populations have the same mean of distribution against the hypothesis that they differ.

Figure 2.2 and 2.3, it is obvious that the NIO basin have the greatest percentage of TCPFs that are hot towers and the greatest overshooting properties although NIO basin has the least population of OTCPFs. This may because that the NIO basin has a much smaller amount of small features with low maximum 20 dBZ echo height relative to other oceanic basins as pointed out by Jiang et al. (2011).

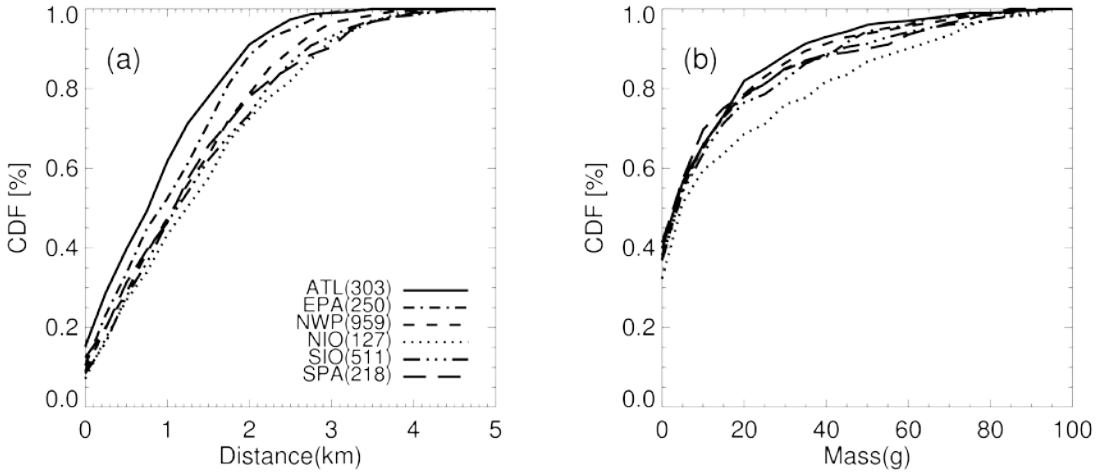

Figure 2.3: Cumulative Density Functions (CDFs) of (a) overshooting distance, and (b) overshooting precipitating ice mass for ATL, EPA, NWP, NIO, SIO, and SPA OTCPFs.

2.4.2 Seasonal distribution

To study the seasonal variations of the population of hot towers in TCs, monthly populations of TCs, TCPFs, and OTCPFs are first calculated for each basin. After dividing each monthly population by the corresponding total population, percentage monthly populations of TCs, TCPFs, and OTCPFs over six oceanic basins are presented in Figure 2.4a-f. For each basin, the monthly percentages for TCs, TCPFs, and OTCPFs sum up to 100%, respectively. There is a strong seasonal variation of OTCPFs in each basin, which is similar to the seasonal variation of TC and TCPF populations. Two exceptions exist, one in NIO and one in SPA, where the monthly variation of OTCPFs shows significant difference from that of TCPFs and TCs. However, A Pearson's chi-squared test shows that these differences among monthly fractions of OTCPFs, TCPFs, and TCs in NIO and SPA basins are not statistically significant. This indicates that in all TC basins, the seasonal variation of OTCPFs is driven by the seasonal variation of TCs and convective systems in TCs.

The monthly variations of overshooting distance, area, volume, and ice mass for six TC basins are displayed in Figure 2.5a-f. Similar to Figure 2.4, the value of overshooting property for each OTCPF are added up together for each basin monthly and then divided by the corresponding total value in the same basin. For example, to get the variation of overshooting distance for OTCPFs in the ATL basin, the value of overshooting distance of each ATL OTCPF are summed up together for each month, and then divided by the total overshooting distance for identified OTCPFs in the ATL basin.

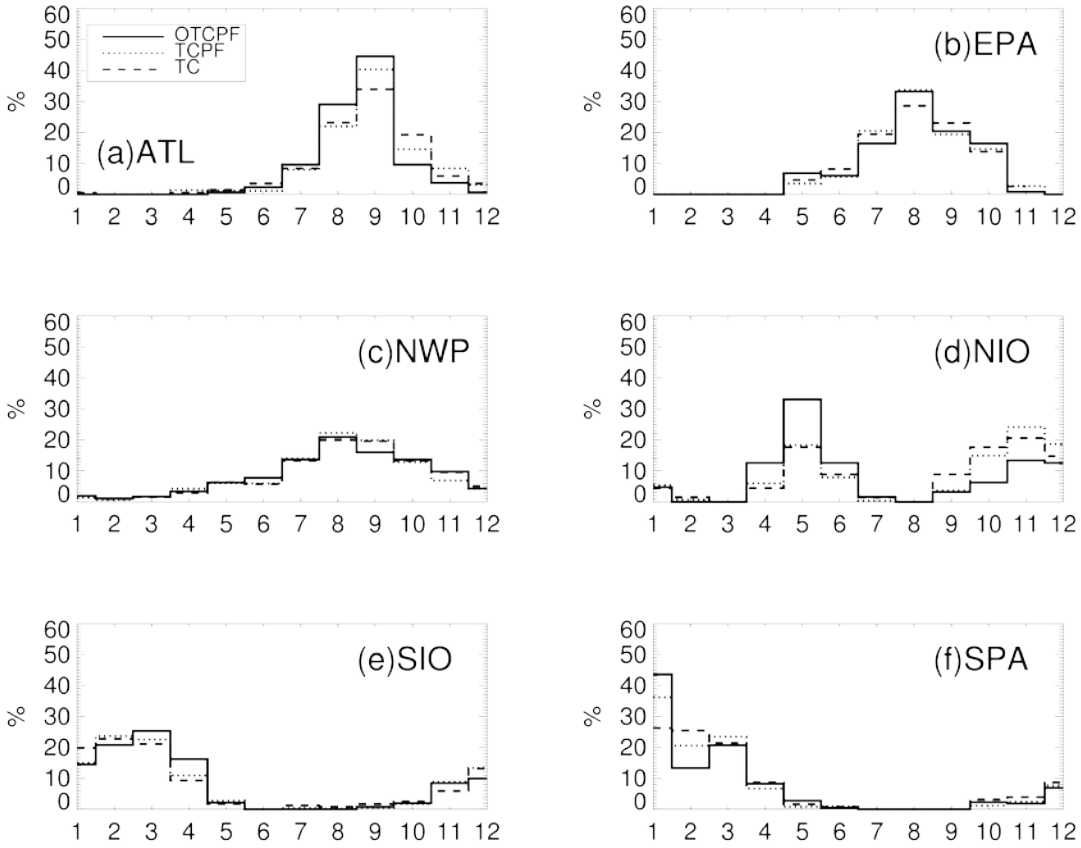

Figure 2.4: Monthly variation of population of OTCPFs, TCPFs, and TCs in (a) ATL, (b) EPA, (c) NWP, (d) NIO, (e) SIO and (f) SPA basins.

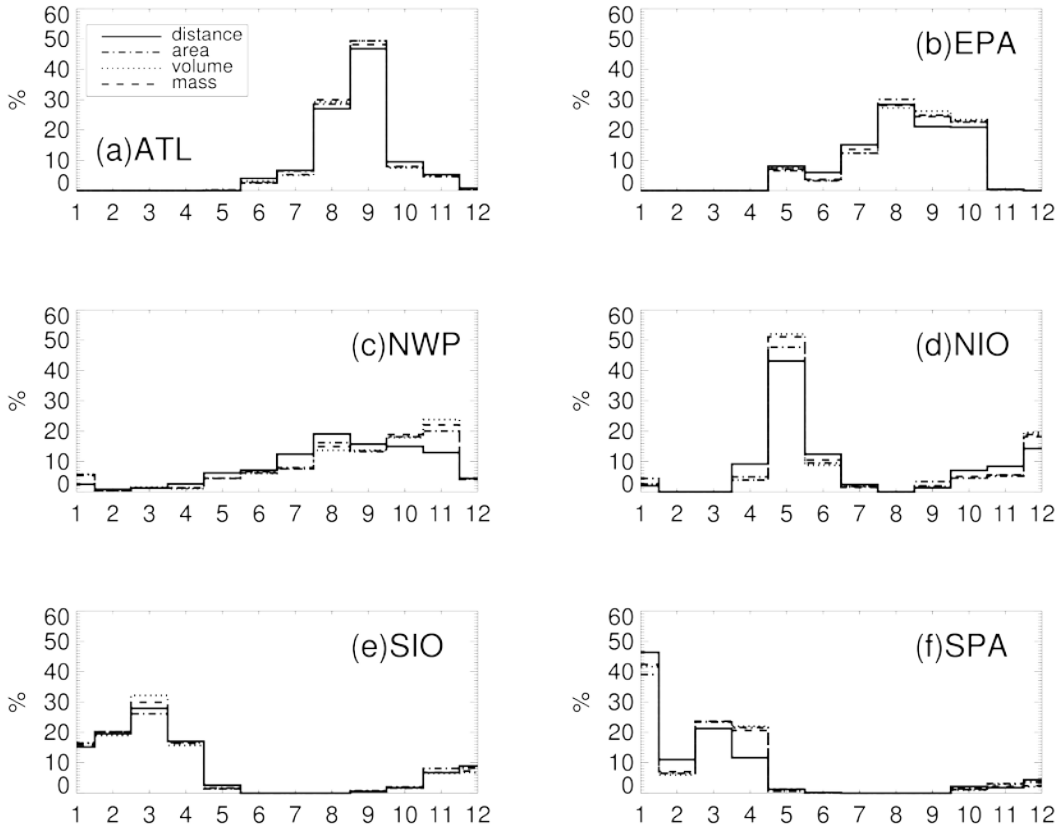

Figure 2.5: Monthly variation of overshooting distance, area, volume and precipitating ice mass of OTCPFs in (a) ATL, (b) EPA, (c) NWP, (d) NIO, (e) SIO and (f) SPA basins.

The monthly percentage for each overshooting property in Figure 2.5 sums up to 100% for each basin. The general patterns for different overshooting properties are similar to each other for each basin, and are similar to the monthly variation for the population of OTCPFs shown in Figure 2.4. For the NIO basin, over 40-55% of overshooting distance, volume, and mass concentrates in May. The second peak is in December with 15-20% magnitude. Over the NWP basin, the percentages of overshooting area, volume, and ice mass peak in November, while that of overshooting distance peaks in August and September. This is different from the seasonal variation of the OTCPF population shown in Figure 2.4c. Other than that, the overall result suggests that the monthly variation of overshooting properties is driven by monthly TC activities.

2.5 The distribution of population and overshooting properties of OTCPFs as a function of TC regions, TC intensities, and TC intensity change stages

2.5.1 TC regions

Fixed radii have been used to study different TC regions in many previous studies. To account for varying TC sizes, a semi-manual separation of inner core (IC), inner rainband (IB), and outer rainband (OB) regions for all the TRMM TC overpasses during 1998-2009 has been accomplished by Jiang et al. (2012). This separation is based on the concept described by Cecil et al. (2002) using TRMM TMI and PR observations. Different from Cecil et al. (2002), TC overpasses with or without eyewalls are both included. The IC region includes complete eyewalls and all near-center convection for

Table 2.3: Mean radius of IC, IB, and OB regions, and populations of TCPFs and OTCPFs and the percentage of OTCPFs in the IC, IB, and OB regions.

Region	Mean Radius (km)	Population of OTCPFs (#)	Population of TCPFs (#)	Percentage of OTCPFs (%)
IC	82	615	6119	10.05
IB	162	337	17568	1.92
OB	502	1416	126626	1.19

storms without eyewalls. The IB region includes banded or blob-like precipitation immediately outside of the IC boundary. The OB region includes outward spiraling banded precipitation and any TC-related precipitation features located about 150-200 km beyond the storm center.

Table 2.3 lists the mean radius, populations of TCPFs and OTCPFs, and the percentage of OTCPFs in IC, IB, and OB regions for the 11-yr TRMM TCPF data used in this study. The mean extents of the IC, IB and OB region are 82, 162, and 502 km, respectively. There are 615, 337, and 1416 hot towers (OTCPFs) found in the IC, IB and OB regions, respectively. It is not surprising that the OB region has most OTCPFs since it has the largest area. However, the percentage of OTCPFs in the OB region is the lowest. While 10.05% of TCPFs in the IC region penetrate over 14 km, only 1.92% and 1.19% of TCPFs are OTCPFs in the IB and OB regions, respectively.

The percentage of TCPFs that are hot towers calculated for each TC basin in different TC regions is presented in Figure 2.6. It can be seen that although in all TC regions, the largest percentage of TCPFs reaching 14 km is found in the NIO basin, but

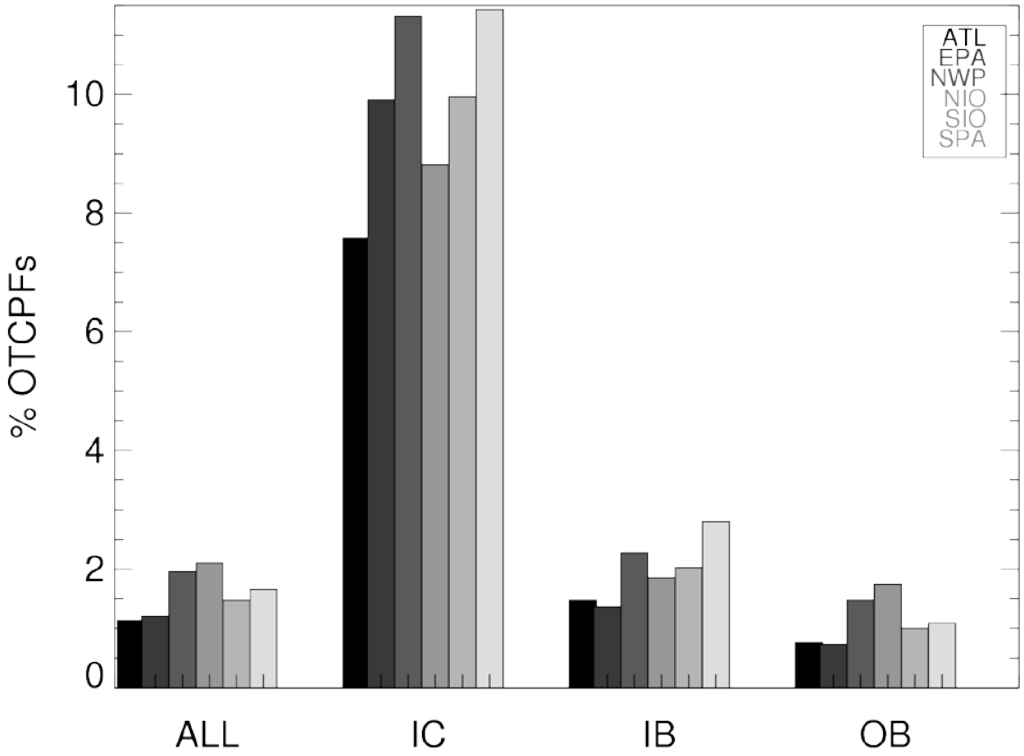

Figure 2.6: The percentage of OTCPFs for six TC-prone basins in all TC regions, and in inner core (IC), inner rainband (IB), and outer rainband (OB) region only. For each group, from left to right are percentage of OTCPFs in the ATL, EPA, NWP, NIO, SIO and SPA basin, respectively.

that's not the case for the IC and IB regions. In the IC region, TCPFs over the SPA and NWP basin have the highest chance to penetrate over 14 km with a percentage of OTCPFs of ~ 11%. A lower percentage of IC OTCPFs is found in the EPA and SIO basins, which is about 10%. The IC TCPFs in the ATL and NIO basins have the lowest percentages of hot towers, which are 7.6% and 8.8%, respectively. In the IB region, the highest percentage of OTCPFs is found in SPA, followed by NWP, SIO, NIO, ATL, and EPA in the decreasing order. In the OB region, TCPFs in the NIO basin have the highest opportunity to penetrate over 14 km (1.74%), followed by NWP, SPA, SIO, ATL, and EPA. This indicates that the greatest percentage of hot towers found over NIO basin in all TC regions is mostly contributed by the OB region, which has the largest amount of TCPFs. A Pearson's chi-squared test[4] has been done and it shows that statistically significant differences exist among the percentages of TCPFs that are hot towers for various TC intensity stages in all TC regions and in IC, IB, and OB region only at the 95% level.

Figure 2.7 presents the Cumulative Density Functions (CDFs) of overshooting properties for OTCPFs in the IC, IB and OB regions. From Figure 2.7a, we can see that IC OTCPFs have the highest overshooting distance with a median value of 1.5 km. CDFs of overshooting distances in the IB and OB regions are very similar (with a median of about 0.9 km), and both are much lower than that in the IC region. About 56% of IC OTCPFs have overshooting distance greater than 1.5 km, while only 33% and 38% of

[4] A Pearson's chi-squared test for independence is to determine whether there is a significant association between two or more variables. In this study, it is used to determine whether there is a significant association between the percentages of TCPFs that are hot towers in different TC basins (Fig. 6), TC intensity stages (Fig. 8), and TC intensity change stages (Fig. 10).

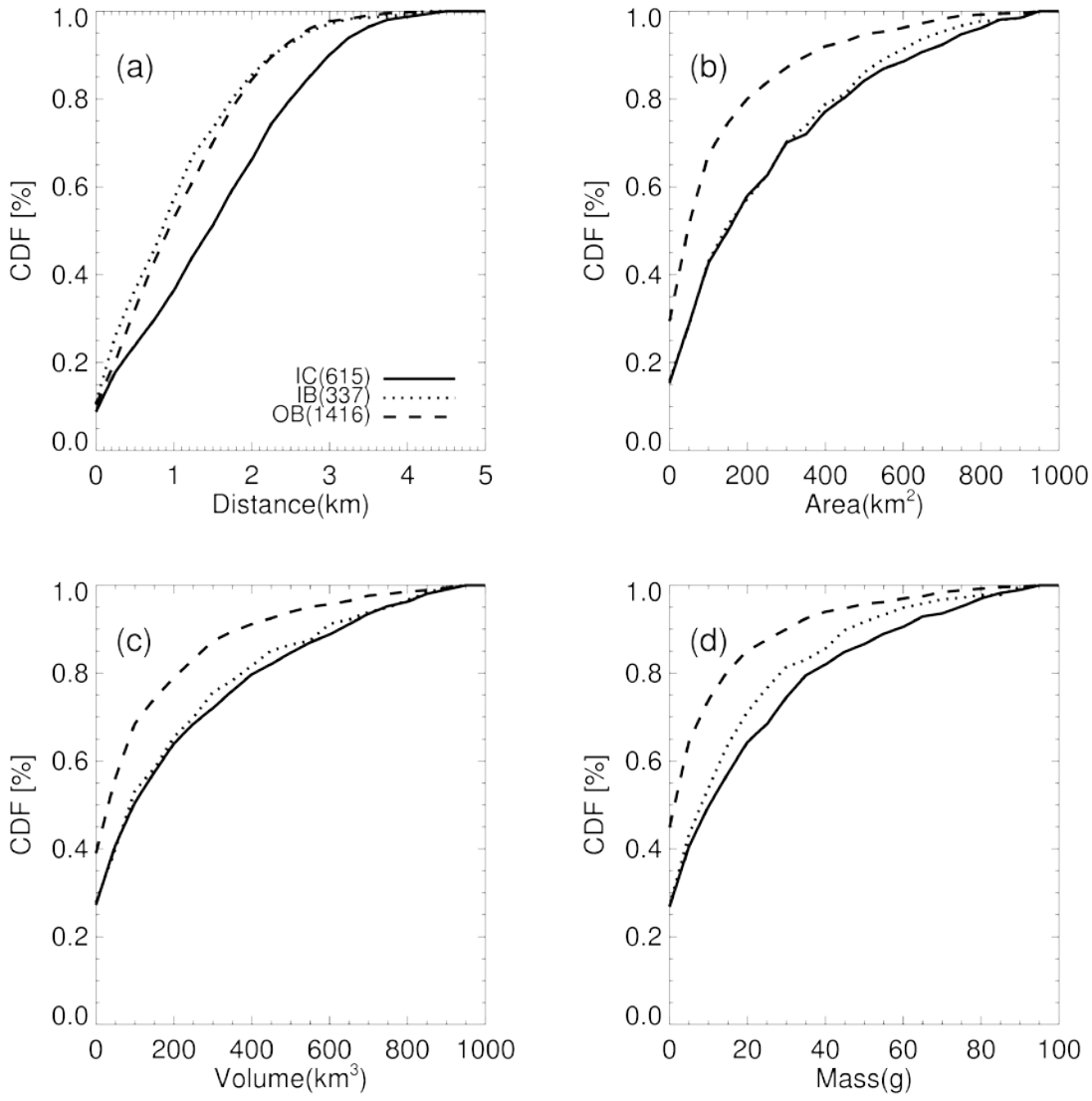

Figure 2.7: CDFs of (a) overshooting distance, (b) overshooting area, (c) overshooting volume and (d) overshooting precipitating ice mass for OTCPFs in the inner core (solid line), inner rainband (dotted line), and outer rainband (dashed line) regions.

those in the IB and OB regions, respectively, achieve that distance. As for the overshooting area (Fig. 2.7b), the distribution for IC and IB features are very similar while much lower values are found for OTCPFs in the OB region. As for overshooting volume and ice mass (Fig. 2.7c-d), IC features produce the largest overshooting properties, followed by IB features. OB features produce the least overshooting volume and ice mass. Based on the significant test using analysis of variance, the differences among various TC regions for each overshooting parameter are statistically significant at the 99% level.

This is consistent with several previous studies. Cecil et al. (2002) studied the convective properties of 45 hurricanes observed by TRMM and indicated that convective precipitation is most often in the eyewall while stratiform precipitation is most readily found in the rainband regions. Using 10-yr TRMM data, Hence and Houze (2011) studied the vertical structure of hurricane eyewalls, and indicated that the eyewall contains higher reflectivity and higher echo tops compared with rainband regions.

2.5.2 TC intensity stages

To study the relationship between hot towers and TC intensity, the identified OTCPFs are classified into four TC intensity groups based on the Saffir-Simpson scale. They are tropical depression (TD), tropical storm (TS), category 1-2 hurricane (CAT 1-2), and category 3-5 hurricanes (CAT 3-5) as shown in Table 2.4. The percentage of TCPFs that are hot towers is 1.83%, 1.66%, 1.20%, and 1.17%, respectively, for TD, TS, category 1-2 and category 3-5 hurricanes. It is interesting to note that this percentage decreases as TC intensity increases.

Table 2.4: Populations of TCPFs and OTCPFs, and the percentage of OTCPFs associated with tropical depression (TD), tropical storm (TS), category 1-2 hurricanes (CAT1-2), and category 3-5 hurricanes (CAT 3-5).

Intensity	Maximum Wind Speed Range (kts)	Population of OTCPFs (#)	Population of TCPFs (#)	Percentage of OTCPFs (%)
TD	$V_{max} < 34$	909	49561	1.83
TS	$64 > V_{max} \geq 34$	922	55544	1.66
CAT 1-2	$64 \leq V_{max} \leq 95$	326	27239	1.20
CAT 3-5	$V_{max} > 95$	211	17969	1.17

However, for different TC regions, the results are very different. As shown in Figure 2.8, in the IC region, the percentage of OTCPFs associated with hurricanes is higher (13% for CAT1-2 and 12% for CAT3-5 hurricane) than that for TS (11%), which is higher than that for TD (7%). This indicates that as TC intensity increases, the percentage of IC features that are hot towers increases generally. However, when looking at IB, OB, and all TCPFs, the reverse is true (Fig. 2.8). A Pearson's chi-squared test has
been done and the result indicates that statistically significant differences exist among different TC intensity stages in all TC regions, and in IC, IB, and OB region only at the 95% level.

CDFs of overshooting properties for identified OTCPFs associated with various TC intensity stages are presented in Figure 2.9. From Figure 2.9a, we can see that at lower frequencies (between 0% and 65% frequency), the greatest overshooting distance is found for OTCPFs related to TS, with lower values for TD and category 1-2 hurricanes features,

and the lowest for OTCPFs associated with category 3-5 hurricanes. The median values for TD, TS, category 1-2 and category 3-5 hurricanes OTCPFs are 1.1 km, 1.2 km,

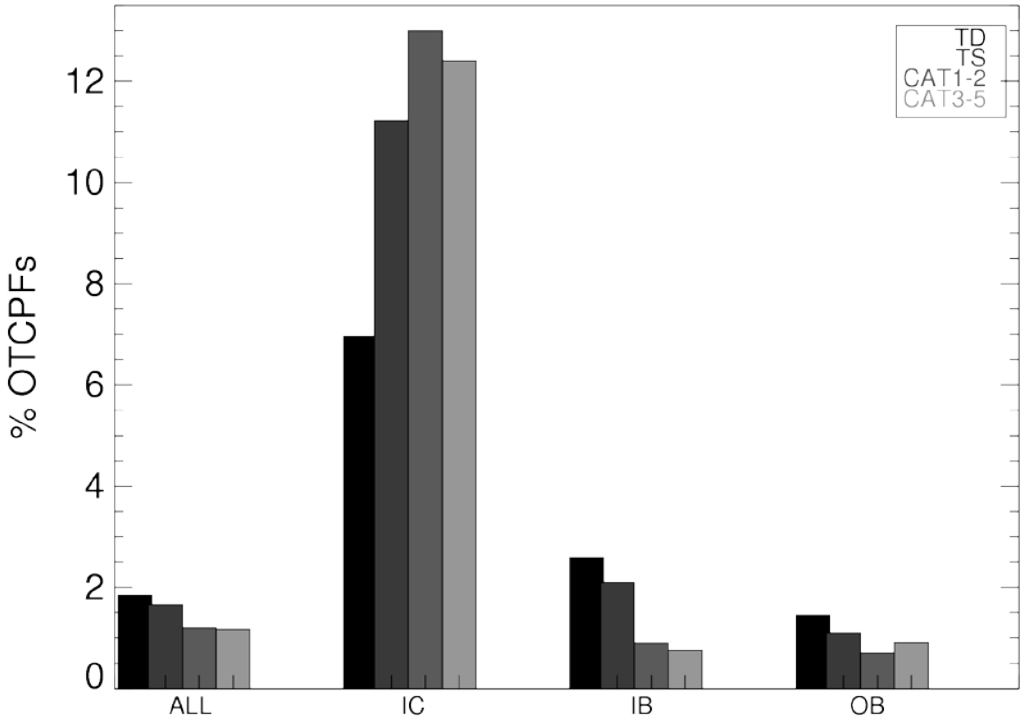

Figure 2.8: The percentage of OTCPFs for different TC intensity stages in all TC regions and in the inner core, inner rainband, and outer rainband region only. For each group, from left to right are percentage of OTCPFs for tropical depression (TD), tropical storm (TS), category 1-2 hurricanes (CAT 1-2), and category 3-5 hurricanes (CAT 3-5), respectively.

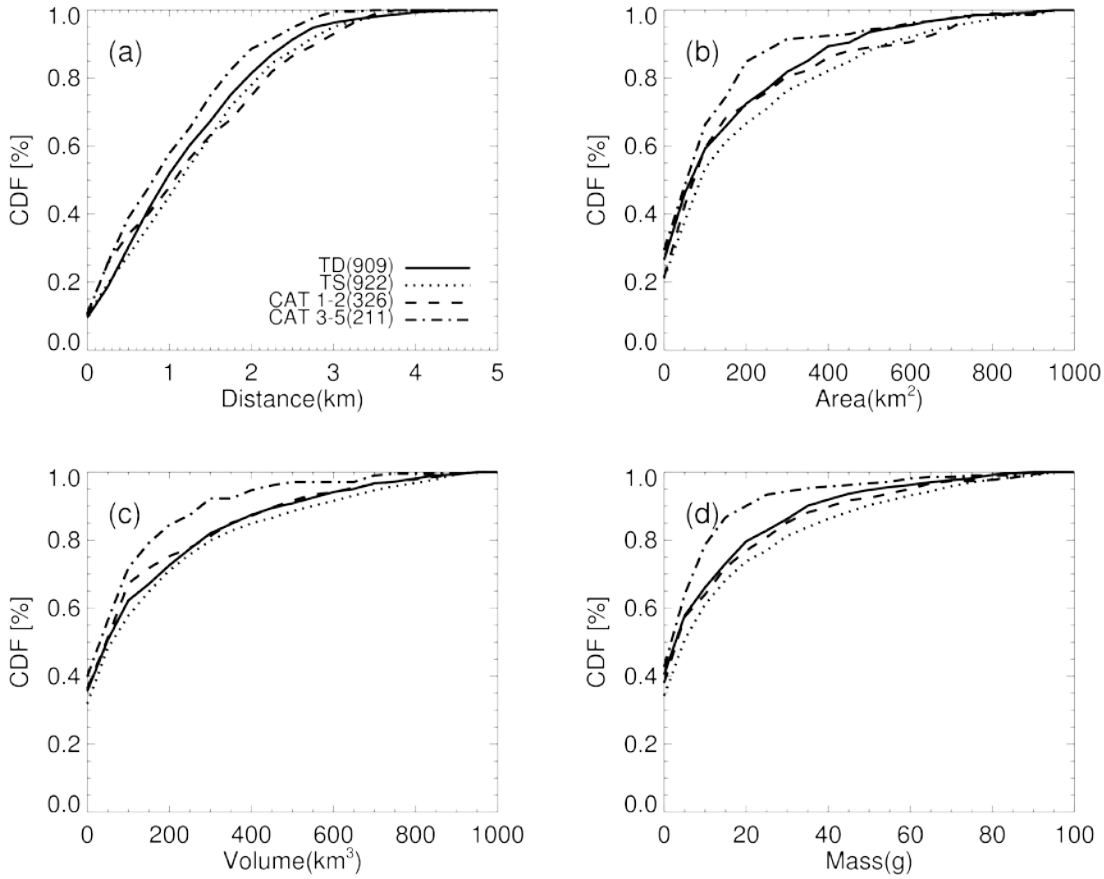

Figure 2.9: CDFs of (a) overshooting distance, (b) overshooting area, (c) overshooting volume and (d) overshooting precipitating ice mass for OTCPFs associated with tropical depression (solid line), tropical storm (dotted line), category 1-2 hurricanes (dashed line), and category 3-5 hurricanes (dash dot line).

1.0 km, and 0.8 km, respectively. At higher frequencies (between 65% and 100%), the highest overshooting distance is found for OTCPFs associated with category 1-2 hurricanes, followed by TS, TD, and category 3-5 hurricanes features.

The largest overshooting area is found for OTCPFs related to TS, lower values for TD and category 1-2 hurricane features, and the lowest for category 3-5 hurricane features (Fig. 2.9b). Similar results are also found for overshooting volume and precipitating ice mass (Fig. 2.9c-d). Overall, category 3-5 hurricane features are found to have the weakest overshooting properties. This may be because TCs reaching the strongest intensity stage have mostly fully developed thus have less intense convection than weaker storms. According to the results from significance tests using analysis of variance, the differences among various TC intensity stages for each overshooting parameter are statistically significant at the 99% level.

2.5.3 TC intensity change stages

Jiang (2012) examined the probability of RI for TCs with or without hot towers in the inner core using TRMM data. Her statistics are based on each TRMM TC observation, that is, only the most convectively intense precipitation feature in the inner core is used. She found that the probability of RI is a factor of 2 higher for TCs with hot towers in the inner core than those without. In this study, our dataset contains all precipitation features not only in the inner core, but also in the inner rainband and outer rainband regions. Our goal here is to examine the percentage of TCPFs that are hot towers in different TC regions for different TC intensity change stages.

Table 2.5: Populations of TCPFs and OTCPFs, and the percentage of OTCPFs associated with rapidly intensification (RI), slowly intensification (SI), neutral (N), and weakening (W) storms.

Intensity change	Maximum Wind Speed Range (kts)	Population of OTCPFs	Population of TCPFs	Percentage of OTCPFs
RI	V_{max24}- $V_{max} \geq 30$	248	12147	2.04
SI	$30 > V_{max24}$- $V_{max} \geq 10$	919	49176	1.87
N	V_{max}-$V_{max24} < 10$, V_{max24}-$V_{max} < 10$	996	66994	1.49
W	V_{max}- $V_{max24} \geq 10$	205	21996	0.93

The rapidly intensifying (RI) threshold used in this study is 30 kt (15.4 ms^{-1}) per day by following Kaplan and DeMaria (2003). As described in section 2.3.1, here the 24h future intensity change interpolated from the 6 hourly best track data into TRMM overpass time is used to define intensity change categories. Three more intensity change categories, i.e., slowly intensifying (SI), neutral (N), and weakening (W), are defined using equal-sized bins (Table 2.5). As a result, 248, 919, 996, and 205 OTCPFs are found associated with RI, SI, neutral, and weakening storms, respectively. The fraction of TCPFs that are hot towers in different TC regions for different TC intensity change stages is presented Figure 2.10. It can be seen that in all TC regions, TCPFs associated with RI has the highest percentage (2.04%) to overshoot 14 km, followed by SI (1.87%), N (1.49%) and W (0.93%). The percentage increases as the intensification rate increases. In the IC region, the trend is even more obvious. About 17% of IC features in RI storms penetrate over 14 km, while the percentage is down to 11% for SI, 9% for neutral, and 8% weakening storms. This suggests

that a good correlation exists between the TC intensification rate and percentage of features that are hot towers in the inner core region.

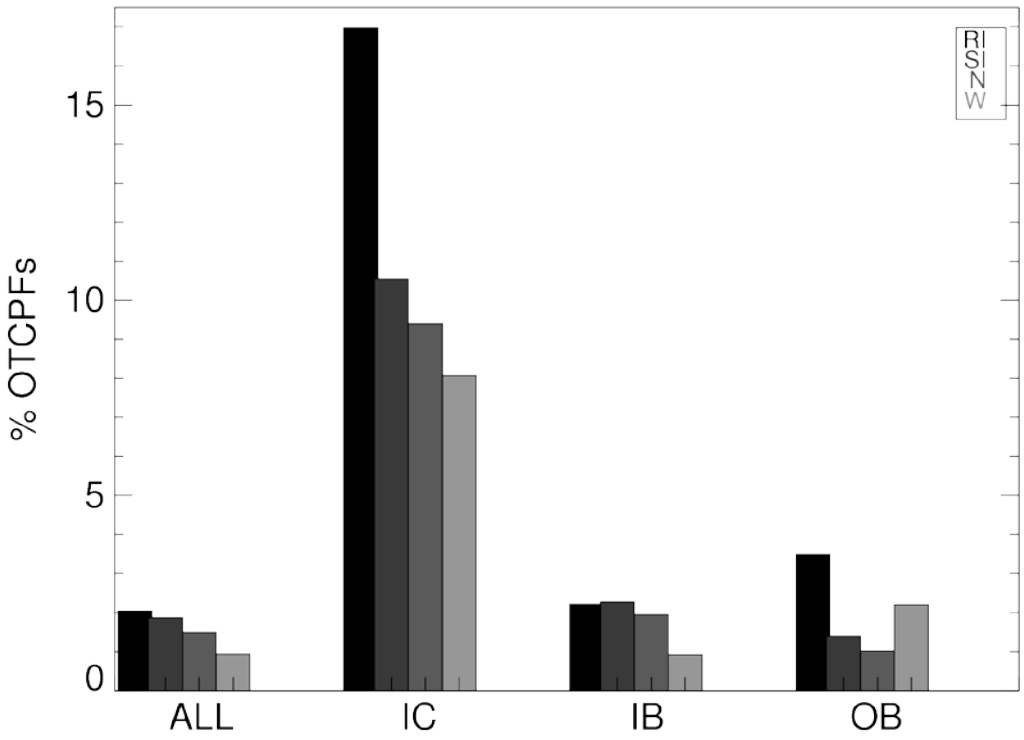

Figure 2.10: The percentage of OTCPFs for different TC intensity change stages in all TC regions and in the inner core, inner rainband, and outer rainband region only. For each group, from left to right are percentage of OTCPFs associated with rapidly intensification (RI), slowly intensification (SI), neutral (N), and weakening (W).

To determine the correlation quantitatively, the IC OTCPFs are first classified into several groups according to different TC intensification rate. Considering the sample size, here a bin of 10 kts per day is applied for each group. Then the fraction of OTCPFs for each TC intensification rate is calculated by dividing the number of OTCPFs by the number of TCPFs. To make the results more reliable, a threshold of at least 10 OTCPFs and 100 TCPFs is required for each qualified point. The result is shown in Figure 2.11. It can be seen that with the fraction of OTCPFs increases from 6.87% to 13.43%, the TC intensification rate increases from -25 kts to 35 kts per day. Furthermore, the linear regression reveals a very good linear relationship between TC intensification rate and the percentage of features that are hot towers in the IC region with a correlation coefficient of 0.94. Significance tests show that this correlation is statistically significant at the 99% level.

Back to Figure 2.10, in the IB region, similar percentages of TCPFs that are hot towers are seen for RI and SI storms, smaller percentage for neutral storms, and the smallest for weakening storms. However, in the OB region, although the percentage of OTCPFs is the highest for RI storm (3.5%), the second highest is for weakening storms (2.2%), followed by SI (1.4%) and neutral (1.0%) storms. Results from Pearson's chi-squared tests for Figure 2.10 show that statistically significant differences exist for the percentages of TCPFs that are hot towers among different TC intensity change stages in all TC regions, and in IC, IB, and OB region only at the 95% level.

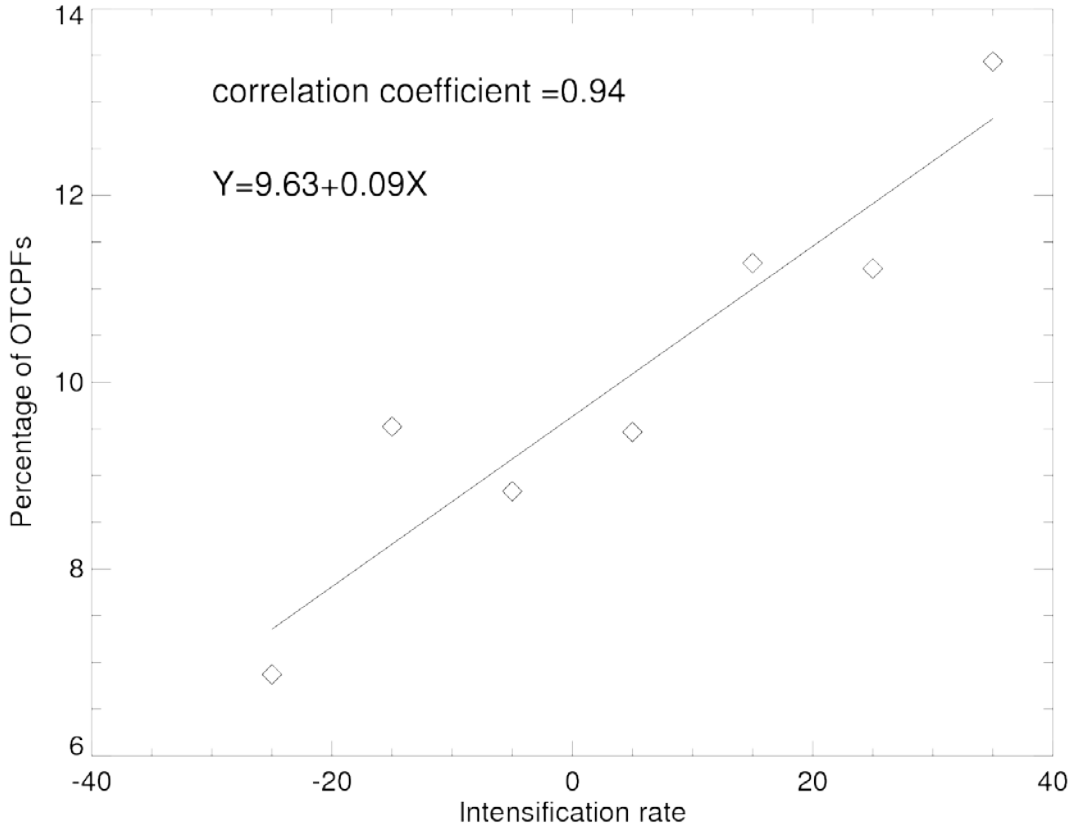

Figure 2.11: Scatterplot of TC intensification rate vs. percentage of OTCPFs in the inner core region. Correlation coefficient as well as the linear equation is shown on the top left.

2.6 Convective properties of OTCPFs

To study the relationship between convective properties and overshooting properties of OTCPFs, four convective proxies, i.e., minimum 11 μm brightness temperature (T_{B11}) from the TRMM Visible and Infrared Scanner (VIRS), minimum 85 and 37 GHz Polarization Corrected Temperature (PCT, Spencer et al. 1989) from the TRMM Microwave Imager (TMI), and maximum height of 40 dBZ radar echo from the TRMM PR, are selected to examine. The minimum T_{B11} here indicates how high a convective cloud can reach. The microwave brightness temperatures at 85 and 37 GHz respond to scattering of upwelling radiation by precipitation-sized ice particles, which reduce the observed brightness temperature. However, the low brightness temperature due to ice scattering could be confused with the sea surface, which also appears cold due to low sea surface emissivity in 85 and 37 GHz channels. The PCT at 85 GHz (Spencer et al. 1989) and 37 GHz (Cecil et al. 2002) is defined to remove the ambiguity in such a way that PCTs are cold for ice scattering and warm for the sea surface regions. The minimum 85 and 37 GHz PCT depends on the optical path of frozen hydrometeors. The 85 GHz channel responses to smaller ice particles, while the 37 GHz weights more toward larger particles. The 85 GHz channel responses to smaller ice particles, while the 37 GHz channel is influenced more by larger particles.

The correlation coefficient is calculated between four overshooting properties and four convective parameters (Table 2.6). Generally, a moderate correlation exists between overshooting properties and convective parameters with correlation coefficients ranging from 0.33 to 0.61. The convective intensity increases as the overshooting distance, area, volume, and ice mass increase. For overshooting distance, the highest correlation

Table 2.6: The correlation coefficients between each overshooting property (including overshooting distance, area, volume and ice mass) and convective parameter (including minimum 11 μm brightness temperature [Min. T_{B11}], minimum 85 and 37 GHz Polarization Corrected Temperature [Min. PCT_{85} and Min. PCT_{37}], and the maximum heights of PR 40 dBZ [Max. Z_{40dBZ}]) for identified OTCPFs.

coefficient correlations	Min. T_{B11}	Min. PCT_{85}	Min. PCT_{37}	Max. Z_{40dBZ}
Distance	-0.61	-0.55	-0.52	0.46
Area	-0.38	-0.52	-0.59	0.33
Volume	-0.40	-0.51	-0.59	0.35
Ice mass	-0.44	-0.52	-0.60	0.36

coefficient is found with minimum T_{B11}, with a correlation coefficient of -0.61. Since T_{B11} indicates the cold cloud top height, it is expected that this parameter is well correlated with the overshooting distance. The overshooting area, volume and precipitating ice mass correlate the best with minimum 37-GHz PCT with correlation coefficients of -0.59, -0.59, and -0.60, respectively. This suggests that OTCPFs with larger overshooting area, volume, and ice mass tend to have greater ice water path contributed by larger ice particles.

2.7 Conclusion

Using the 11-year TRMM TCPF database, TCPFs that are hot towers (OTCPFs) are identified based on five reference levels. It is found that only 1.59 % of deep convective systems in TCs have 20 dBZ radar echoes reaching 14 km and only 0.09% of them even reach the 380 K potential temperature level. Given the geographical distribution of OTCPFs show little sensitivity to various reference heights and considering the smaller

sample sizes when using higher reference levels, 14-km is chosen to identify hot towers in the rest of the study. Emphasis is placed on the geographical and seasonal variations of hot towers in TCs and how hot towers are distributed in different TC regions and intensity and intensity change stages.

Among six TC-prone oceanic basins, the highest population of TC convective systems (TCPFs) and TCPFs that are hot towers (OTCPFs) is found over the northwest Pacific basin. However, the greatest percentage of TCPFs that are hot towers is found over the north India Ocean basin. OTCPFs in this basin also have larger overshooting distance and ice mass, although it has the lowest population of both TCPFs and OTCPFs. The analysis of seasonal variations shows that both the population and overshooting properties of OTCPFs is driven by the monthly activities of TCs.

For different TC regions, it is found that TCPFs in the IC region have the highest chance (11%) to overshoot above 14 km, while the percentage of OTCPFs is only 2% and 1% in the IB and OB regions, respectively. OTCPFs in the IC region have much larger overshooting distance, area, volume, and ice mass than those in the IB and OB regions. It is also shown that the highest fraction of OTCPFs found in the NIO basin is mostly contributed by OTCPFs in the OB region. In the IC and IB region, higher percentages of TCPFs with hot towers are in the SPA and NWP basins.

In the IC region only, the percentage of TCPFs that are hot towers increases as TC intensity increases. However, when looking at IB, OB, and all TCPFs, the reverse is true. It is also interesting to note that the smallest overshooting distance, area, volume, and ice mass are found for OTCPFs in category 3-5 hurricanes. This may be because TCs reaching

the strongest intensity stage have mostly fully developed thus have less intense convection than weaker storms.

For different TC intensity change categories, it is found that the percentage of TCPFs that are hot towers increases as the intensification rate increases, especially in the inner core region. About 17% of IC features in RI storms penetrate over 14 km, while the percentage is down to 11% for SI, 9% for neutral, and 8% weakening storms. A linear regression has been applied to determine the correlation between the TC intensification rate and the percentage of TCPFs that are hot towers in the IC region quantitatively. The result shows a very good linear relationship between these two parameters with a correlation coefficient of 0.94.

The relationship between convective properties and overshooting properties of OTCPFs are examined. The overshooting distance correlates best with minimum 11 μm brightness temperature. For overshooting area, volume, and ice mass, the best correlations are found with minimum 37 GHz PCT. This suggests that OTCPFs with larger overshooting area, volume and ice mass tend to produce larger ice particles.

3. DISTRIBUTIONS OF SHALLOW TO VERY DEEP PERCIPITATION-CONVECTION IN RAPIDLY INTENSIFYING TROPICAL CYCLONES

3.1 Abstract

Shear-relative distributions of four types of precipitation/convection in tropical cyclones (TCs) are statistically analyzed using 14-yr of Tropical Rainfall Measuring Mission (TRMM) Precipitation Radar (PR) data. The dataset of 1139 TRMM PR overpasses of tropical storms through category 2 hurricanes over global TC-prone basins is divided by future 24-h intensity change. It is found that increased and widespread shallow precipitation (defined as where the 20-dBZ radar echo height < 6 km) around the storm center is a first sign of rapid intensification (RI) and could be used as a predictor of the onset of RI. The contribution to total volumetric rain and latent heating from shallow and moderate precipitation (20-dBZ echo height between 6 and 10 km) in the inner core is greater in RI storms than in non-RI storms, while the opposite is true for moderately deep (20-dBZ echo height between 10 and 14 km) and very deep precipitation (20-dBZ echo height ≥ 14 km). The authors argue that RI is more likely triggered by the increase of shallow to moderate precipitation and the appearance of more moderately to very deep convection in the middle of RI is more likely a response or positive feedback to changes in the vortex. For RI storms, a cyclonic rotation of frequency peaks from shallow (downshear right) to moderate (downshear left) to moderately and very deep precipitation (upshear left) is found and may be an indicator of a rapidly strengthening vortex. A ring of almost 90% occurrence of total precipitation is found for storms in the middle of RI, consistent with the previous finding of the cyan and pink ring on the 37-GHz color product.

3.2 Introduction

Prediction of tropical cyclone (TC) intensity change, especially rapid intensification (RI), has shown relatively little improvement over the last three decades compared with forecasts of TC motion, in spite of the availability of advanced satellite observations and the development of sophisticated numerical models. One of the most fundamental reasons is a lack of understanding of the physical processes and mechanisms that govern the TC intensity variability.

Intensity forecasting is challenging since the inner- core evolution involves a complex interaction among processes occurring on spatial scales varying over many orders of magnitude (Marks and Shay 1998). Several environmental conditions associated with RI have been identified, including warm sea surface temperatures SSTs) and a deep warm oceanic mixed layer, low vertical wind shear, high lower-tropospheric relative humidity, conditional instability, large-scale upper-level divergence, and low-level convergence patterns (Merrill 1988; Kaplan and DeMaria 2003; Wang and Wu 2004). Although these environmental and oceanic factors are reasonably well predicted owing to improvements in dynamical models and have proved to be useful in forecasting RI (Kaplan et al. 2010), the false-alarm ratio still remains undesirably high, suggesting that these external processes play only a partial role in RI. It is thus reasonable to hypothesize that internal processes operating on scales smaller than the environmental scales may be much more important in distinguishing RI and slowly intensifying storms (Hendricks et al. 2010).

Convective-scale processes within the inner-core region of TCs are widely believed

to be one of the most important subsynoptic-scale contributors to TC intensification. Previous modeling studies have argued the importance of rotating, asymmetric deep convection in the inner core, termed vortical hot towers (VHTs), to TC intensification (Hendricks et al. 2004; Montgomery et al. 2006; Nguyen et al. 2008). Montgomery and Smith (2011) proposed that asymmetric convection/heating was the preferred spin up mechanism. However, it is noted that these VHTs were mainly reported in tropical depressions by observational studies (e.g., Reasor et al. 2005; Houze et al. 2009), while RI usually occurs in storms ranging in intensity from tropical storms through category 2 hurricane systems (Kaplan and DeMaria 2003; Kieper and Jiang 2012).

In contrast, early theoretical studies have shown that symmetric convection/heating was the preferred mechanism at spinning up the inner-core winds (e.g., Ooyama 1969; Shapiro and Willoughby 1982). More recently, Nolan and Grasso (2003) and Nolan et al. (2007) revisited the issue and examined the evolution of a symmetric, balanced vortex perturbed by asymmetric, unbalanced heat sources based on an improved linearized primitive equation model. They indicated that the intensity of the vortex changes as a symmetric response to the azimuthally averaged latent heating re- lease and found that heating inside the radius of maximum winds (RMW) has a much higher efficiency with which diabatic heating released within the storm core is converted into the kinetic energy of the storm-scale primary circulation (e.g., Vigh and Schubert 2009; Rogers 2010). This suggests that asymmetric, intense convective cells do not play any specific role in intensification other than to the extent to which they add to the symmetric mean heating.

Particularly for RI, several observational case studies have shown horizontally

small-scale, asymmetric deep convection (such as convective bursts and hot towers) within the inner core of TCs undergoing RI (Reasor et al. 2009; Guimond et al. 2010; Molinari and Vollaro 2010; Nguyen and Molinari 2012; Reasor and Eastin 2012; Stevenson et al. 2014; Rogers et al. 2015; Susca-Lopata et al. 2015), especially when the storm was experiencing moderate-to-high vertical wind shear. For example, Nguyen and Molinari (2012) argued that Hurricane Irene (1999) rapidly intensified because the diabatic heating produced by asymmetric, intense convection was strong enough to dramatically increase the azimuthally averaged heating. Reasor et al. (2009) and Reasor and Eastin (2012) illustrated that the rapid intensification of Hurricane Guillermo (1997) under moderate shear coincided with the formation and cyclonic rotation of strong convective bursts through the left-of-shear semicircle. A series of observational studies on Hurricane Earl (2010) (Stevenson et al. 2014; Rogers et al. 2015; Susca-Lopata et al. 2015) showed that asymmetric deep convective bursts and lightning strikes occurred before Earl's rapid intensification.

However, statistical studies using long-term satellite observations have shown different results. To test the VHT theory hypothesized by modeling studies (e.g., Montgomery and Smith 2011), Jiang (2012) examined the inner-core convection, especially hot towers (defined as maximum 20-dBZ radar echo height $\geq$ 14.5 km), in different TC intensity change categories. It was shown that the probability of 24-h future RI does not significantly increase when hot towers exist in the inner-core region, and it was suggested that hot towers are neither a necessary nor a sufficient condition for RI. Several other satellite-based statistical studies supported the symmetric mechanism of TC

intensification with a focus on RI. Kieper and Jiang (2012) indicated that a symmetric ring feature on the Naval Research Laboratory (NRL) 37-GHz color composite microwave satellite product (Lee et al. 2002) is a very good predictor of RI in the following 24 h. They subjectively defined the ring to be at least 90% closed around the storm center with either cyan color or pink color on the NRL 37-GHz color product. Lee et al. (2002) indicated that qualitatively warm rain or low-level water clouds appear cyan and deep convection appears pink. However, by reviewing a large number of TRMM TC overpasses, we found that any precipitation with ice aloft appears pink, which could be either strati- form or convective, and not necessarily deep convection. Although it is often claimed that the ring is ‘‘precipitative’’ (Zagrodnik and Jiang 2014, hereafter ZJ14), it has never been proven with direct quantitative information. As an indirect proof, using a 10-yr dataset from the Tropical Rainfall Measuring Mission (TRMM) satellite, Jiang and Ramirez (2013) determined that RI in the future 24 h requires a minimum threshold for the current inner-core raining area and volumetric rain that is appreciably higher than non-RI storms.

By compositing a large number of passive microwave satellite overpasses relative to vertical wind shear direction, Harnos and Nesbitt (2011) claimed that they found a convective ring forming 6 h before RI begins and intensifying over the following 24-h RI period. The ring at the onset of RI had a 50% occurrence of an ice- scattering signature defined by the 85-GHz polarization-corrected brightness temperature (PCT; Spencer et al. 1989) < 250 K, indicating at least moderate convection in TC eyewalls with TRMM PR 17-dBZ radar echo-top heights around 9–10km (Cecil and Zipser 2002, their Fig. 10). However, Harnos and Nesbitt’s (2011) study did not mirror the Southern Hemisphere TC

overpasses relative to shear direction before compositing them with Northern Hemisphere TC overpasses. This could cause a severe overestimate of the percent occurrence of convection, especially in the right-of-shear quadrants. Indeed, Harnos and Nesbitt's (2011) Figure 3 showed that the occurrence of 85-GHz PCT ≤ 250 K is downshear-right dominant during RI, RI + 6 h, and RI + 12 h, which is contradictory to many previous studies that have confirmed the downshear-left regions s the preferred regions for total precipitation and convection (Corbosiero and Molinari 2002, 2003; Chen et al. 2006; Cecil 2007; Hence and Houze 2012).

A more careful study, conducted by ZJ14, composited the 14yr of TRMM Precipitation Radar (PR) overpasses only from Northern Hemisphere TCs. Not surprisingly, they showed a ring of only 5% occurrence of radar reflectivity > 20 dBZ at or above 10-km elevation, which is a moderately intense convection definition slightly stronger than that used in Harnos and Nesbitt (2011), for storms that have undergone RI for at least 12h and will continue to rapidly intensify during the following 24 h (see their Fig. 8e). Although ZJ14 were not able to directly prove that the 37-GHz cyan and pink ring found by Kieper and Jiang (2012) is precipitative, ZJ14's Fig. 6e does show a closed ring of 70% occurrence of near-surface PR reflectivity > 20dBZ for storms that have undergone RI for at least 12 h and will continue to rapidly intensify during the following 24 h. Note that the 20-dBZ level is closely analogous to the raining area and was used to define precipitation features in Nesbitt et al. (2000). Because of the larger footprint size of the 37-GHz channel than that of the PR, it is highly possible that a ring at a larger percent occurrence would be seen if the PR data used in ZJ14 were degraded to the 37-GHz

equivalent footprint size. ZJ14 concluded that the rainfall frequency and latent heating distributions were more symmetric near the onset of RI and continued to be more symmetric as RI continues and the rainfall coverage expands upshear.

While these satellite-based statistical studies implied that the symmetry of widespread precipitation containing a much lower percentage of asymmetric deep convection is important in initiating RI in the following 24 h, observational case studies mentioned above (Reasor et al. 2009; Guimond et al. 2010; Molinari and Vollaro 2010; Nguyen and Molinari 2012; Reasor and Eastin 2012; Stevenson et al. 2014; Rogers et al. 2015) emphasized the role of asymmetric very deep convection in RI. An important question raised from this is, what is the relative importance of precipitation–convection of different depths– intensities to RI? In this study, we consider the inner-core precipitation–convection in more detail by separating it into four categories according to its radar echo-top height from very deep, moderately deep, moderate, to shallow. The latent heat release in the inner core is the primary driving force of TC intensification. ZJ14 found that total rainfall amount is closely correlated with total latent heat release, and the rainfall frequency is best correlated to future intensity change. In this study, we focus specifically on the frequency of four kinds of precipitation–convection and their corresponding contribution to total volumetric rain in different TC future 24-h intensity change stages. Our primary goal is to identify whether there are significant differences in the distributions of different kinds of inner-core precipitation–convection between storms at the beginning of RI, the middle of RI, and those that do not undergo RI. We also focus on quantifying the relative contribution to total volumetric rain in the inner core from moderately deep–very deep

convection versus shallow–moderate precipitation.

This study extends ZJ14's work by using an extended version of their TRMM PR dataset that exclusively includes storms in at least moderately favorable environments (see section 2a). ZJ14 focused on the distributions of rainfall frequency, moderately deep convection, and latent heating, while this study focuses on the frequency of four types of precipitation–convection and their relative contributions to total rainfall. Similar to ZJ14, we consider the distribution of precipitation–convection relative to the TC center and relative to the vertical wind shear. The organization of TC convection and precipitation within the inner core is primarily dominated by the environmental vertical wind shear, while the impact of storm motion on the eyewall convective asymmetry appears to be secondary (Corbosiero and Molinari 2002, 2003; Reasor et al. 2013). Both numerical model simulations (e.g., Rogers et al. 2003) and observational studies (Corbosiero and Molinari 2002, 2003; Chen et al. 2006; Cecil 2007; Hence and Houze 2012) have confirmed that the downshear to downshear-left regions are favored for upward motion and precipitation.

The TRMM spectral latent heating (SLH) estimates (Shige et al. 2004, 2007) were analyzed intensively in ZJ14. In this study, we analyze both latent heating and total rainfall, but results shown below focus mainly on total rainfall. As pointed out by Park and Elsberry (2013), the SLH algorithm significantly underestimates convective-scale cooling rates in tropical mesoscale convective systems. Therefore, the latent heating results in both ZJ14 and this study likely overestimate the heating rates at lower levels in convective pixels.

3.3 Data and methodology

3.3.1 TRMM PR overpasses selection

The dataset used in this study is an extended version of the 14-yr TRMM PR dataset (from 1998 to 2011) used by ZJ14. ZJ14's dataset is derived from the TRMM Tropical Cyclone Precipitation Feature database (TCPF; Jiang et al. 2011). TCPF includes the overpasses of all global TCs viewed by the TRMM satellite that reached tropical storm intensity during their lifetimes. The storm center, storm intensity, and storm translation speed of each overpass are interpolated from the National Hurricane Center (NHC) and Joint Typhoon Warning Center (JTWC) best-track data. As the PR has a narrow 247-km swath (215 km before the TRMM orbital boost in August of 2001), ZJ14 have manually filtered all PR overpasses so that at least some portion of the TC center or near-center area is within the PR swath. The best-track storm center of each overpass was also manually adjusted by ZJ14 when the PR or TRMM Microwave Imager (TMI) 37-GHz data suggest that the center should be moved.

Geographically, overpasses used in ZJ14 were restricted to the Northern Hemisphere, including the Atlantic, North Pacific (eastern and western), and north Indian Ocean basins. In this study, overpasses in the Southern Hemisphere (including south Indian and South Pacific Ocean basins) are also included. We use version 7 of the TRMM PR 2A25 algorithm (Iguchi et al. 2009) reflectivity and rain rate and 2H25 latent heating data (Shige et al. 2007). As indicated by ZJ14, 2H25 latent heating is closely correlated with PR 2A25 rain rates with a linear correlation coefficient of 0.89. The PR reflectivity has a vertical resolution of approximately 250 m (at nadir) and a horizontal resolution of 5×5

km^2 (4.3×4.3 km^2 before the orbital boost). To compare the 37-GHz cyan and pink ring with the radar reflectivity and 85-GHz PCT field, the TMI 1B11 37- and 85-GHz brightness temperatures are also used in this study.

It is well known that RI rarely occurs in an unfavorable environment, such as during movement to a region with cold sea surface temperature (SST) or strong vertical wind shear, or during landfall (Kaplan and DeMaria 2003). To focus on the role of inner-core convection in RI, ZJ14 have applied several criteria to the selection of PR overpasses to exclude the impacts of both external factors and other internal factors, such as eyewall replacement cycles (Willoughby et al. 1982). These criteria are as follows: SST > 26°C, vertical wind shear < 16 m s^{-1}, mean inner-250-km total precipitable water (TPW) .> 50 mm, storm translation speed < 11 m s^{-1}, the TC center is located over water both at the time of the overpass and 24 h in the future, and the intensity of the storm at the time of the overpass is be- tween tropical storm and category 2 hurricane. According to ZJ14, the cutoff criteria for SST, TPW, shear, and storm motion were derived from a larger dataset of several thousand TRMM TMI overpasses. All storms that underwent RI in that larger dataset had environmental conditions that met or exceeded these minimum criteria.

The SST is derived from the 0.25° Reynolds daily SST grid point nearest to the storm center (Reynolds et al. 2007). The vertical wind shear is calculated by averaging the 200- and 850-hPa wind vectors from the European Centre for Medium-Range Weather Forecasts (ECMWF) interim reanalysis dataset (Simmons et al. 2007) within a ring of 500–750km from the TC center and subtracting the averaged 200-hPa wind vector from the averaged 850-hPa wind vector. The 500–750-km ring is used to eliminate the influence of the storm's

circulation as much as possible by following the method of Hence and Houze (2011). The TPW data from the ECMWF has a resolution of $0.75^{o}\times0.75^{o}$ and was averaged for the innermost 250 km around the TC center. More details of the dataset are described by ZJ14.

3.3.2. Selection of intensity change categories

The final dataset contains a total of 1139 PR TC overpasses from 489 storms in global TC-prone basins between 1998 and 2011. In this study, the intensity of a TC is defined as the maximum sustained surface wind. Based on the difference in the maximum surface wind between the time of the overpass and 24 h in the future, all overpasses are classified into four intensity change categories: weakening (W), neutral (N), slowly intensifying (SI), and rapidly intensifying (RI), following the method of Jiang (2012) and Jiang and Ramirez (2013).

Table 3.1 lists definitions and final sample sizes in each category. It should be noted that the RI definition in Table 3.1 depends only on the difference between the current and future 24-h intensity. However, an RI event (defined as multiple, continuous, and overlapping 24-h periods in which the intensity increased in each period by 30 kt or more; see Kieper and Jiang 2012) can continue for as long as 48–60 h. This indicates that the time of the overpasses in the RI category does not necessarily correspond to the onset of the RI event. Therefore, based on the intensity change in the 12, 18, and 24 h prior to the TRMM overpass, RI cases are subdivided into RI initial and RI continuing by following ZJ14.

Table 3.1: Definition of intensity change categories and sample size of selected PR overpasses for each category. V_{max} and V_{max+24} represent the current and future 24-h maximum surface wind speeds, respectively.

Category	24 h future maximum wind speed change range (kt)	# of PR overpasses
W	$V_{max+24} - V_{max} \leq -10$	191
N	$-10 < V_{max+24} - V_{max} < 10$	449
SI	$10 \leq V_{max+24} - V_{max} < 30$	360
RI	$V_{max+24} - V_{max} \geq 30$	139
Total	-	**1139**

Table 3.2: Definition of initial and continuing rapid intensification (RI), and the number of sampled PR overpasses.

Category	Max. wind speed range (kt)	PR over-passes	Passes with a 85-GHz PCT ≤ 250 K ring	Passes with a 37-GHz cyan+pink ring	Passes with a 37-GHz ring within PR swath
RI initial	$V_{max+24} - V_{max} \geq 30$ and $V_{max}(0,+6,+12) - V_{max}(-24, -18, -12) < 30$	59	5	42	30
RI continuing	$V_{max+24} - V_{max} \geq 30$ and $V_{max}(0,+6,+12) - V_{max}(-24, -18, -12) \geq 30$	80	23	70	53
RI total	$V_{max+24} - V_{max} \geq 30$	139	28	112	83

The RI initial storms began an RI event within 12h of the overpass, while the RI continuing storms had a previous 24-h RI period beginning at 12, 18, or 24 h prior to the overpasses. It is important to note that the RI event in both subcategories continues for at least 24 h following the overpass. Therefore, both subcategories are important in the forecast of RI, although the RI initial storms are near the onset of an RI event, while the RI

continuing storms are in the middle of an RI event. The definition and the corresponding sample sizes of RI initial and RI continuing overpasses are summarized in Table 3.2. There are 59 out of 139 RI overpasses (42%) during which the storms did not rapidly intensify (> 30 kt per 24 h increase) in the past 12, 18, or 24 h, therefore being categorized as RI initial.

Figure 3.1 displays the frequency distributions of initial intensity, intensity change during the past 12h, SST, TPW, environmental vertical wind shear, and storm motion for different intensity change categories. The corresponding means are summarized in Table 3.3. Student's t tests show that RI continuing storms have higher initial intensity and lower environmental shear than RI initial storms, which are significant at the 99.9% and 95% confidence levels, respectively. However, the differences of the two parameters between SI and RI initial storms, and the differences of all other parameters among various TC intensity change categories, are not significant at any confidence level. This indicates that, under minimally favorable environmental conditions, it is difficult to predict RI based on the environment alone.

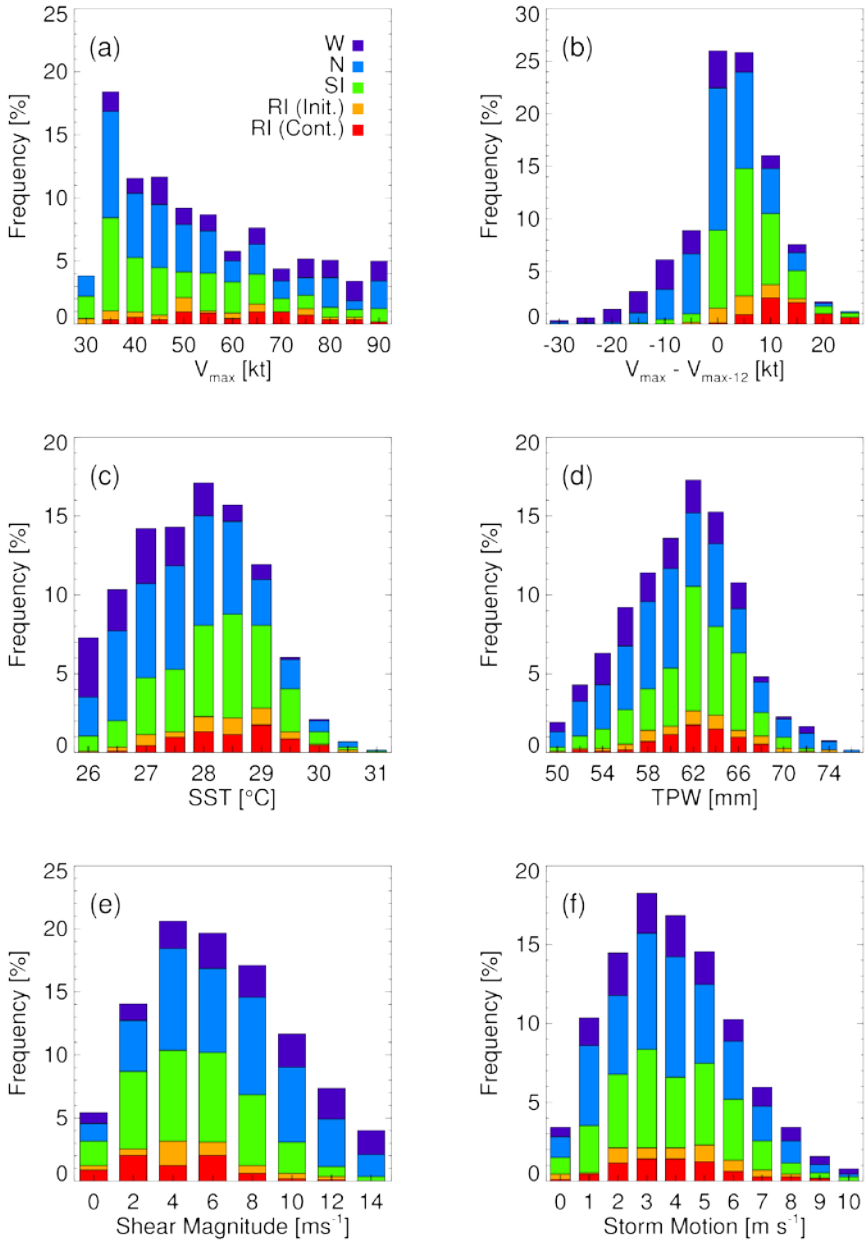

Figure 3.1: Frequency distribution of (a) maximum sustained surface wind speed intensity (Vmax) at the time of the TRMM overpass, (b) the change of Vmax during the 12 h before the overpass, (c) SST, (d) TPW, (e) shear magnitude, and (f) storm motion. Each

distribution is divided into colors representing the five future 24-h intensity change categories shown in (a).

Table 3.3: Mean values of current V_{max}, the change of V_{max} during the 12 h before the overpass, SST, TPW, vertical wind shear magnitude, storm motion, and the difference in the direction of the vertical wind shear and the storm motion vector parameters for the total dataset and different intensity change categories. Asterisks in the RI, RI initial, and RI continuing columns represent the statistical significance between SI and RI, SI and RI initial, and RI initial and RI continuing storms, respectively, at the 90% (*), 95% (**), 99% (***), and 99.9% (****) confidence levels.

Mean values	W	N	SI	RI	RI (initial)	RI (continuing)	Total
V_{max} [kt]	63.5	53.8	52.6	60.4****	56.1	63.4****	55.9
$V_{max} - V_{max\text{-}12}$ [kt]	-2.7	2.8	8.0	12.1	7.0	15.7	4.6
SST [^{o}C]	27.4	28.0	28.4	28.7	28.6	28.7	28.1
TPW [mm]	60.6	61.7	62.9	63.3	63.5	63.2	62.1
Shear [m s^{-1}]	8.9	7.9	6.3	5.5**	6.3	5.0**	7.3
Motion [m s^{-1}]	4.6	4.2	4.4	4.5	4.5	4.4	4.4
Shear – Motion [^{o}]	-60.5	-53.1	-55.5	-61.7	-51.0	-69.7	-56.2

3.3.3 Definition of four kinds of precipitation–convection

Hot towers have been defined in many ways, with cloud-top brightness temperatures colder than a given threshold from satellite infrared (IR) images (e.g., Gettelman et al. 2002; Jiang and Tao 2014), extremely low polarization-corrected temperature (PCT; e.g., Spencer et al. 1989) measured by microwave radiometers owing to the large amount of frozen hydrometeors, high radar reflectivity at high altitude (e.g., Kelley et al. 2004; Liu and Zipser 2005; Tao and Jiang 2013; Jiang and Tao 2014), or strong mean upward motion

within the midtroposphere (e.g., Rogers 2010; Reasor et al. 2009). In this study, very deep precipitation (i.e., a hot tower) is defined as the 20-dBZ radar echo height ≥ 14km, consistent with Tao and Jiang (2013) and Jiang and Tao (2014). A better name would be ‘‘very deep convection.’’ However, different types of precipitation–convection are defined using the height of 20-dBZ radar echo in this study. For pixels with higher echo-top heights, they are more likely to be convection (or convective precipitation). But for lower echo tops, they could be either convective or stratiform precipitation. In any case, the 20-dBZ radar echo indicates precipitating clouds. Therefore, in the following text, the name of each type of precipitation–convection is referred to as precipitation instead of convection, although it might be more appropriate to refer to the very deep and moderately deep types as convection.

To further examine the relative importance of very deep precipitation versus shallow–moderate precipitation in initiating RI, three more types of precipitation are identified based on the height of 20-dBZ radar echo (Z_{20dBZ}), including moderately deep precipitation ($14 > Z_{20dBZ} \geq 10$ km), moderate precipitation ($10 > Z_{20dBZ} \geq 6$ km), and shallow precipitation ($Z_{20dBZ} < 6$ km). At the top of the cloud, the radar reflectivity is approximately 20 dBZ (note that the PR's minimum detectable signal is about 17 dBZ), which corresponds to a precipitation rate of approximately 1 mm h^{-1} of ice hydrometeors (Kelley 2008). Here we use the height of the 20-dBZ radar echo as a proxy for convective/precipitative intensity.

The hot tower hypothesis proposed that tall convective clouds with undiluted cores play important roles in heat and moisture transport between the upper troposphere and

lower stratosphere (Riehl and Malkus 1958; Simpson 1978). A recent study by Fierro et al. (2009), however, indicated that the cores that transport a considerable amount of moist static energy were diluted by entrainment. From their model simulations, over 60% of the air parcels originating near cloud base penetrated over 10-km altitude, while only 5% exceeded the 14-km level. Thus, it was suggested that the definition of hot towers be re-defined as deep convective clouds that reach 10km or above, the upper levels of the troposphere. Although Fierro et al.'s (2009) study was of a convective line in the Tropical Ocean and Global Atmosphere Coupled Ocean– Atmosphere Response Experiment (TOGA COARE) and not associated with a TC, other studies also suggested that the 17–20-dBZ radar echo reaching 10 km is a good criterion for moderately intense convection in TCs (e.g., Cecil and Zipser 2002; ZJ14). Based on these studies, the 10-km level is selected to separate moderate and moderately deep precipitation–convection. The very deep precipitation and moderately deep precipitation categories collectively are equivalent to the redefined hot towers as proposed by Fierro et al. (2009).

To examine the contribution of latent heat energy attributable to liquid precipitation versus ice processes, the 6-km altitude is chosen to separate shallow and moderate precipitation. In the inner core of TCs, the freezing level is close to 5 km (Hence and Houze 2011) and perhaps higher than 5 km for more intense storms. Therefore, it is reasonable to assume that there is almost no ice in the inner core below 6 km. Even if there is some small amount of ice, results in this study focus more on the depth of the precipitation and latent heat release than on microphysics.

3.3.4 Methodology and selection of variables

This study uses two types of figures: radial distributions and two-dimensional (2D) composite images. The radial distribution plots are generated by grouping the PR pixels from different intensity change categories into bins representing 5-km annuli extending radially outward from the TC center. The 2D composite images are chosen for their advantage of allowing for the accumulation of data from numerous overpasses in a single 2D plot to display the shear-directed distributions of precipitation in TCs. To generate a composite image, the PR overpasses are first rotated with the vertical wind shear vector pointing northward (along the +y axis) and the TC center located in the center of the plot. The shear-relative pixels of Southern Hemisphere overpasses are flipped 180^{o} before compositing them with Northern Hemisphere cases, following Chen et al. (2006) and Wingo and Cecil (2010). The PR pixels, with their new coordinates relative to the TC center and vertical wind shear vector, are then compiled into 10×10 km^2 grid cells. As a result, the value of each grid cell represents either the frequency or total volumetric rain (see selection of variables in the next paragraph) of pixels satisfying each precipitation type criterion relative to total pixels that fall into each 100 km^2 box. It is noted that both RI and very deep precipitation are rare events. To ensure meaningful statistics when generating the composites, we require that at least three PR pixels meet the precipitation criterion within each 100-km^2 box from all overpasses for each intensity change category.

As described in the introduction, our main goal is to examine the frequency of four kinds of precipitation and their corresponding contribution to total volumetric rain and latent heating in different TC future 24-h intensity change stages. Therefore, three variables

are selected for this study: 1) percent occurrence of each type of precipitation (%), 2) total volumetric rain (mm h^{-1} km^2), and 3) total latent heating (Kh^{-1}). The percent occurrence of precipitation is the fraction of the number of pixels from different types of precipitation divided by the total number of PR pixels. The total volumetric rain is the sum of the pixel-based products of multiplying the PR 2A25 near-surface rain rate (mm h^{-1}) by the area of each pixel within each annulus or grid cell normalized by the number of pixels in the domain. The total latent heating is the sum of vertically integrated PR 2H25 latent heating from the surface to 18 km within each annulus or grid cell normalized by the number of pixels in the domain, following ZJ14.

3.4 Percent occurrence of precipitation

3.4.1 Radial distributions

Figure 3.2 shows the radial distributions of percent occurrence of four kinds of precipitation and total precipitation for all samples and different intensity change categories. The azimuthally averaged percent occurrence of precipitation is shown from the storm center outward to 150 km, corresponding to the inner-core and inner-rainband region (there is very little difference among various intensity change categories beyond 150 km). We are particularly interested in the difference between SI and RI initial categories to see if the precipitation distributions can help forecasters distinguish the onset of RI from SI cases. The differences among SI, RI initial, and RI continuing cases are also important because the RI continuing category not only represents the middle of an RI event but also is useful for predicting the continuation of RI in the following 24 h.

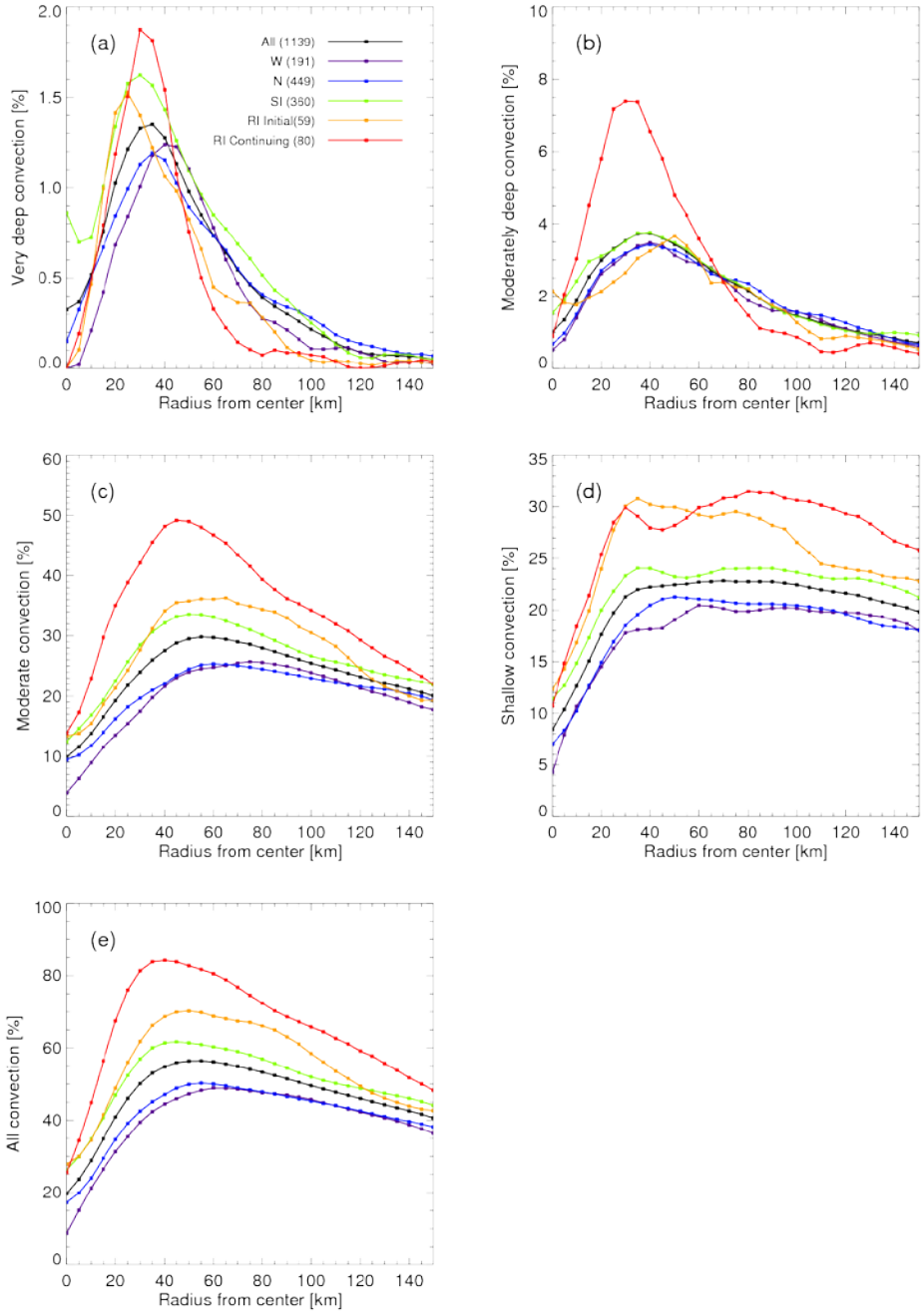

Figure 3.2: Radial distributions of azimuthally averaged percent occurrence of (a) very deep precipitation, (b) moderately deep precipitation, (c) moderate precipitation, (d) shallow precipitation, and (e) all precipitation for the total sample and different intensity change categories shown in (a).

It is quite rare for 20-dBZ reflectivity to reach the 14-km level, as the maximum percent occurrence is less than 2% (Fig. 3.2a). Overall, intensifying storms (both RI and SI) have higher peak values of percent occurrence of very deep precipitation than non-intensifying storms, consistent with the statistical study using airborne radar data in Rogers et al. (2013). RI continuing storms have the highest peak, followed by SI and RI initial storms. However, it is greater only in the 25–40-km range from the TC center. The frequencies of very deep precipitation for RI (both initial and continuing) storms drop below the other categories beyond 60km. RI initial storms have a slightly lower percent occurrence of very deep precipitation than SI storms at all radial distances (Fig. 3.2a). Averaged within the innermost 100 km, SI storms have the greatest percent occurrence of very deep precipitation (0.83%; Table 3.4), followed by N (0.65%), RI continuing (0.6%), W (0.56%), and RI initial (0.5%) storms. A Student's t test shows that SI have significantly (95% confidence level) more very deep precipitation than RI initial storms.

Within 70km from the storm center, RI continuing storms have a higher frequency of moderately deep precipitation than storms in all other intensity change categories (Fig. 3.2b). The peak of the RI continuing curve (about 7.5%) is about double the rest of the categories. But similar to very deep precipitation, the frequency of moderately deep precipitation also drops below the other categories beyond 70 km. Averaged within 100 km of the TC center, the mean percent occurrence of moderately deep precipitation for RI continuing is about 1.3% higher than that of RI initial cases, which is significant at the 99% confidence level. The percent occurrences of moderately deep precipitation for RI initial, SI, N, and W storms are very similar to each other (Fig. 3.2b; Table 3.4).

Table 3.4: Composite-mean values of the percent occurrence of precipitation in each shear-relative quadrant, averaged within 100 km of the TC center. Asterisks in the RI, RI initial, and RI continuing rows represent the statistical significance between SI and RI, SI and RI initial, and RI initial and RI continuing storms, respectively, at the 90% (*), 95% (**), 99% (***), and 99.9% (****) confidence levels.

Very deep convection	**DR**	**UR**	**UL**	**DL**	**Total**
W	0.25	0.17	0.80	1.13	0.60
N	0.40	0.13	0.64	1.41	0.65
SI	0.37	0.27	1.06	1.60	0.82
RI	0.37	0.11	0.79	0.87*	0.53**
RI (initial)	0.28	0.07	0.73	1.23	0.56**
RI (continuing)	0.45	0.14	0.83	0.61	0.51
All	0.36	0.18	0.82	1.36	0.68
Moderately deep convection	**DR**	**UR**	**UL**	**DL**	**Total**
W	1.81	1.04	2.38	4.33	2.42
N	1.92	1.17	2.58	4.53	2.56
SI	2.03	1.28	2.99	4.37	2.65
RI	2.24	1.75**	4.03**	3.67	2.91
RI (initial)	1.58	1.12	4.11	3.25	2.47
RI (continuing)	2.79	2.29**	3.98	3.98	3.27***
All	1.98	1.26	2.85	4.34	2.61
Moderate convection	**DR**	**UR**	**UL**	**DL**	**Total**
W	26.38	13.23	16.71	35.20	23.11
N	24.54	14.37	20.01	33.77	23.16
SI	31.29	20.89	25.18	42.72	30.00
RI	34.96	28.14****	39.65****	48.19**	37.60****
RI (initial)	31.55	24.09	34.43**	42.59	32.84
RI (continuing)	37.78	31.67**	43.77*	52.42**	41.46***
All	28.28	17.99	23.40	38.51	27.06
Shallow convection	**DR**	**UR**	**UL**	**DL**	**Total**
W	19.37	13.21	18.74	24.53	19.09
N	21.07	14.04	20.25	24.64	20.00
SI	24.03	19.82	23.81	25.56	23.30
RI	31.38****	27.62****	27.99*	29.72**	29.15****
RI (initial)	30.71***	25.98***	27.51	30.55**	28.60***
RI (continuing)	31.94	29.06	28.38	29.09	29.59
All	22.96	17.46	22.02	25.51	21.99

Figure 3.2c shows that RI continuing storms have the highest percent occurrence of moderate precipitation at all radial distances among all intensity change categories. The peak value is about 50%, appearing at the 40-km radius from the storm center. The mean percent occurrence within 100 km from the storm center for RI continuing storms is about 9% higher than that for RI initial storms, and the difference is significant at the 99% confidence level (Table 3.4). RI initial storms have a slightly higher percent occurrence of moderate precipitation than SI storms in the radial range of 40–120km, while SI storms have a higher percent occurrence than N and W storms at all radial distances.

A pronounced difference between RI initial and SI storms is seen in Fig. 3.2d. The percent occurrences of shallow precipitation for both RI initial and RI continuing cases are similar, which are much higher than that of SI in all radial distances from the TC center. The peaks of the RI initial and RI continuing curves reach above 30%, which is about 7%–12% higher than those of the SI, N, and W curves. Table 3.4 shows that the difference of the mean inner-100-km percent occurrence of shallow precipitation between RI initial and SI storms is about 5% and is significant at the 99% confidence level. This implies that increased and widespread shallow precipitation may be the first sign of RI and may be used to distinguish RI onset from SI. Moderate precipitation also increases slightly (Fig. 3.2c) from the SI to RI initial category, but moderately deep and very deep precipitation do not increase until the later stage of RI (i.e., the RI continuing category; Figs. 3.2a,b) and therefore are a symptom instead of an indicator of the onset of RI.

Figure 3.2e presents the radial distribution of the per- cent occurrence of total precipitation (the sum of four types of precipitation), which is very similar to the rainfall

frequency (percent occurrence of near-surface reflectivity exceeding 20 dBZ) shown in ZJ14's Figure 5a. Significant differences in the frequency of total precipitation are found between SI, RI initial, and RI continuing cases. Based on airborne Doppler observations, Rogers et al. (2013) found that intensifying TCs have a higher azimuthal coverage of precipitation than steady- state TCs. They further argued that this difference may be due to the difference in the magnitude of vertical wind shear. However, in this study, the environmental conditions (including vertical wind shear and the difference of shear direction and storm motion direction; see Table 3.3) are very similar between SI and RI initial cases. Therefore, the higher azimuthally averaged per- cent occurrence of total precipitation at the onset of RI may be due to internal factors.

Comparing Figs. 3.2a–d with Fig. 3.2e, it is found that the difference of the occurrences of total precipitation between RI continuing and RI initial storms is mainly contributed by the difference in moderate and moderately deep precipitation, while the difference between RI initial and SI storms mainly comes from shallow and moderate precipitation. This implies that the increased amount of shallow to moderate precipitation may be used to predict the onset of RI, while the increased amount of moderate to moderately deep precipitation may be used to predict the continuation of RI in the next 24 h.

3.4.2 Composite images

The corresponding shear-relative distributions of percent occurrence of four types of precipitation are presented in Figs. 3.3–3.6, with the storm center in the middle and vertical

wind shear pointing upward along the +y axis. According to the direction of the vertical wind shear vector, the upper-left, upper-right, lower- left, and lower-right quadrants are referred to as downshear left (DL), downshear right (DR), upshear left (UL), and upshear right (UR), respectively (Chen et al. 2006; ZJ14). Here, we focus only on the region within 100 km from the center. The 25-, 50-, 75-, and 100-km radii are shown as dotted rings in each panel. The quadrant- mean values of the percent occurrence of various kinds of precipitation, which are averaged in the innermost 100 km of the TC center, are shown in Table 3.4.

Figure 3.3 shows the composite shear-relative distribution of the frequency of very deep precipitation for W, N, SI, RI initial, and RI continuing storms. Previous studies have shown that the downshear-left quadrant is favored for the greatest rainfall frequency (ZJ14) and highest rain rates (Chen et al. 2006). The distributions of the very deep precipitation frequency for W, N, SI, and RI initial storms have a similar pattern as the rainfall distribution shown in Chen et al. (2006) and ZJ14, with the downshear-left quadrant containing significantly more very deep precipitation than any other quadrant (Figs. 3.3a–c, e; Table 3.4). In Fig. 3.3f for RI continuing storms, the maximum frequency of very deep precipitation shifts more toward the upshear-left quadrant with a secondary maximum located in the downshear-right quadrant. The modeling study of Hurricane Wilma (2005) by Zhang and Chen (2012) showed that convective bursts

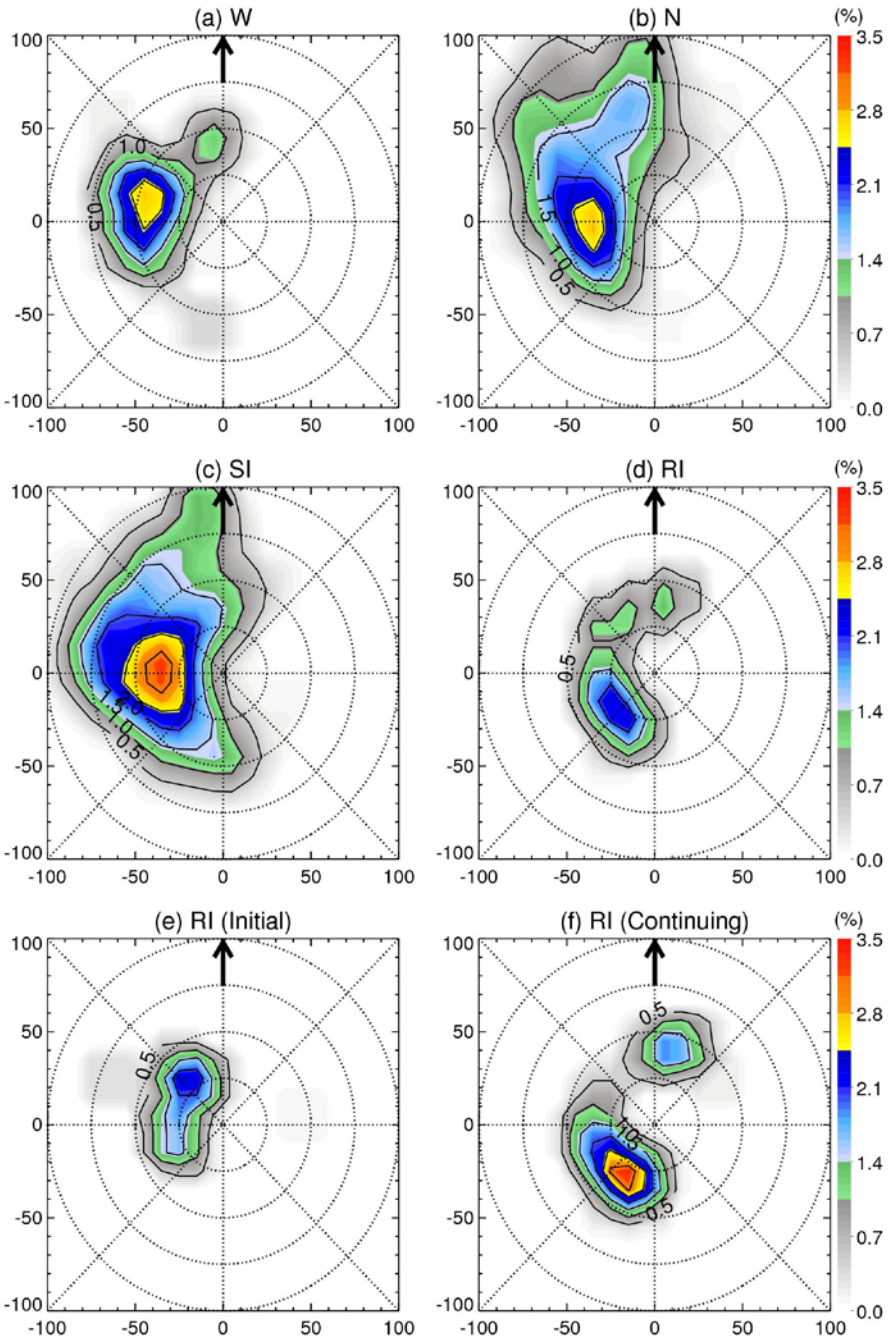

Figure 3.3: Composite shear-relative distribution of the percent occurrence of very deep precipitation for (a) W, (b) N, (c) SI, (d) RI, (e) RI initial, and (f) RI continuing. The black arrow represents the orientation of the vertical wind shear vector. The 25-, 50-, 75-, and 100-km radii are shown as dotted rings.

occurred mostly in the upshear quadrant when the storm underwent RI. The largest area of > 1% occurrence of very deep precipitation is observed in SI storms (Fig. 3.3c), followed by N (Fig. 3.3b) and W (Fig. 3.3a) storms. Very deep precipitation is less widespread in RI continuing (Fig. 3.3f) and RI initial (Fig. 3.3e) storms. However, a major difference is observed in both RI continuing and initial cases, as the occurrences of very deep precipitation are almost entirely concentrated within the innermost 50km, likely near or within the RMW. As estimated by ZJ14, in the TRMM PR dataset used in this study, the mean RMW is 49 km for SI and 38km for the combined RI (initial and continuing) storms, which compares favorably with RMW values of 43 km for intensifying and 53 km for steady-state TCs in Rogers et al. (2013).

The percent occurrence of moderately deep precipitation in Fig. 3.4 indicates a similar pattern for weakening, neutral, and slowly intensifying storms (Figs. 3.4a–c), with the downshear-left quadrant containing significantly greater moderately deep precipitation than any other shear-relative quadrant. A remarkably different distribution is observed for RI continuing (Fig. 3.4f) and RI initial (Fig. 3.4e) storms, with the maximum frequency of moderately deep precipitation appearing in the upshear-left quadrant and located closer to the center (at 25–50 km for RI continuing storms and 25–75 km for RI initial storms). Figures 3.4c,e illustrate a pronounced difference between SI and RI initial cases in the upshear-left quadrant where RI initial storms have a much greater percent occurrence of moderately deep precipitation than SI storms. The opposite is true for any other shear-relative quadrant (Table 3.4). RI continuing storms (Fig. 3.4f)

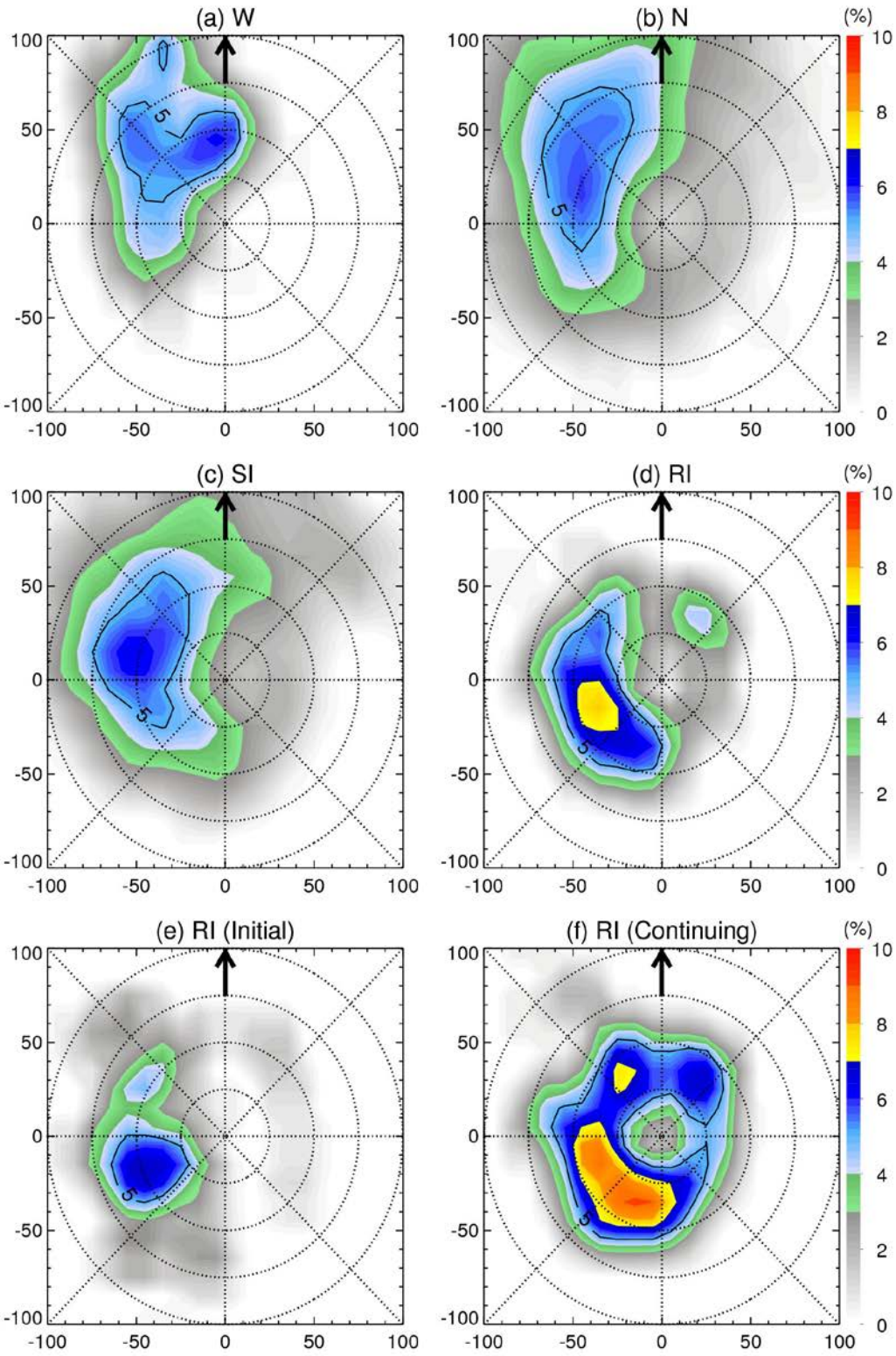

Figure 3.4: As in Figure 3.3, but for moderately deep precipitation.

have a much more symmetric distribution compared with other intensity change categories. An almost closed ring of > 5% occurrence in the innermost 50 km is found for RI continuing cases, with the maximum values located upshear left peaking around 10%.

Deep convection near or within the RMW has been linked to vortex strengthening in many studies (e.g., Vigh and Schubert 2009; Reasor et al. 2009; Molinari and Vollaro 2010; Rogers 2010; Nguyen and Molinari 2012; Rogers et al. 2013). However, Figs. 3.3–3.4 indicate that there is no more moderately deep to very deep precipitation–convection in RI initial storms than in W and N storms. This suggests that rapid intensification is likely triggered by other mechanisms and that the appearance of more deep convection in the middle of RI is more likely a response or positive feedback to changes in the vortex that occur earlier in the SI period to the beginning of the RI period.

For moderate precipitation, Fig. 3.5 shows that the downshear-left quadrant is favored in all categories. A similar pattern is observed for weakening and neutral storms, and it is more asymmetric than that of SI and RI storms. For W and N storms (Figs. 3.5a,b), the maximum frequency of moderate precipitation is 40%–50% in the downshear-left quadrant, while less than 20% is upshear right. RI initial storms, with a more symmetric distribution, have more moderate precipitation than SI storms in all shear-relative quadrants (Fig. 3.5e). Moderate precipitation becomes more widespread and symmetric around the center as RI continues. An almost-closed ring of at least 40% occurrence around the center is found for RI continuing storms (Fig. 3.5f), while only 30% is found for RI initial storms (Fig. 3.5e). This indicates a significant increase of moderate precipitation during RI from the onset of RI in all quadrants.

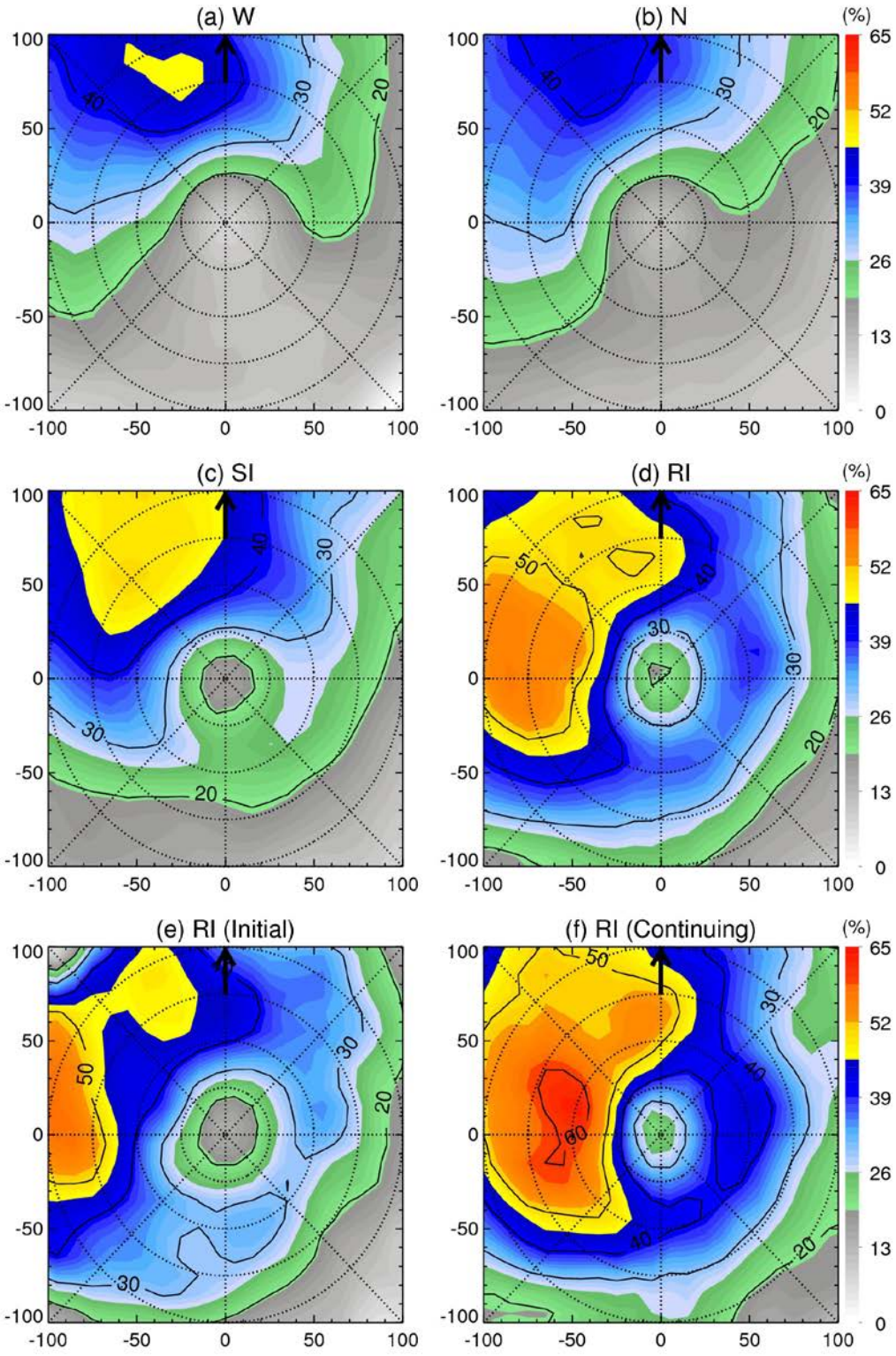

Figure 3.5: As in Figure 3.3, but for moderate precipitation.

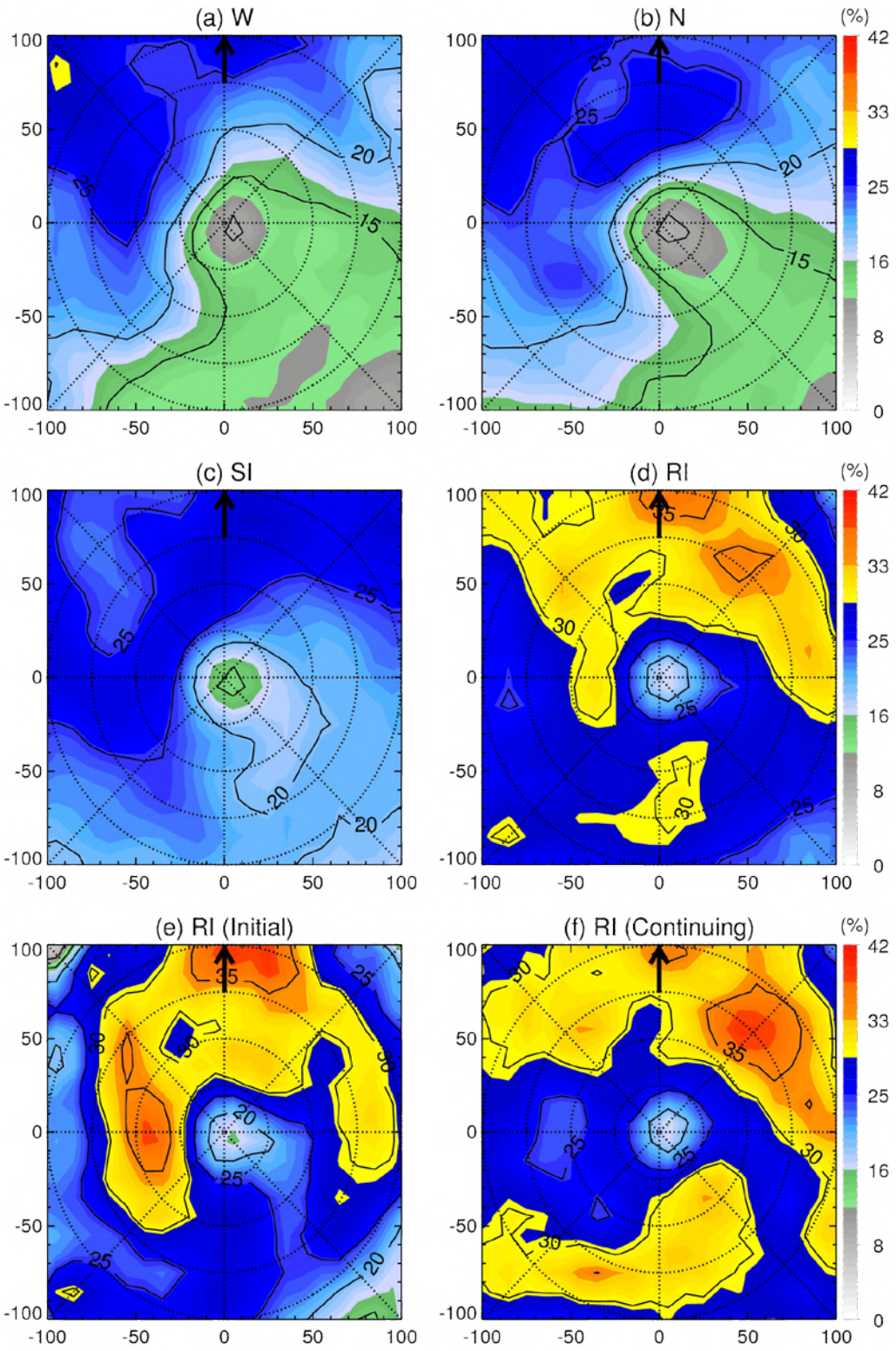

Figure 3.6: As in Figure 3.3, but for shallow precipitation.

Asymmetric distributions are also observed for both W and N storms in the percent occurrence of shallow precipitation (Figs. 3.6a,b), with a maximum of 25%–30% DL occurrence and less than 15% UR occurrence. SI storms (Fig. 3.6c) have a similar pattern to W and N storms but a higher frequency of shallow precipitation in the UR quadrant. Shallow precipitation is much more widespread for storms at the onset of RI, as a much higher percent occurrence is found for RI initial storms than SI storms in all shear-relative quadrants (Fig. 3.6e; Table 3.4). For RI initial storms, a ring of at least 25% occurrence of shallow precipitation is almost completely wrapping around the center, peaking at about 38%. As RI continues, the shallow precipitation does not in- crease as much as other types of precipitation, but the shear-relative distribution becomes more symmetric (Fig. 3.6f). Overall, Figs. 3.5–3.6 suggest that more widespread and more symmetric shallow to moderate precipitation is an indicator of either the onset, or the continuation, of RI.

From Figs. 3.3–3.6, we can see that the downshear-left quadrant is favored for all types of precipitation for W, N, and SI storms, consistent with results found by many previous studies for TCs in general (Corbosiero and Molinari 2002, 2003; Chen et al. 2006; Cecil 2007; Hence and Houze 2012). However, the shear-relative distributions for RI storms are remarkably different. For both RI initial and continuing storms (Figs. 3.6e,f), shallow precipitation peaks in the downshear-right quadrant, which is the quadrant where the triggering of convective updrafts begins, as indicated by previous studies (Black et al. 2002; Hence and Houze 2011, 2012). As precipitation becomes deeper, the location of peak precipitation rotates cyclonically for RI storms. Moderate precipitation peaks in the downshear-left quadrant, similar to all other intensity change categories (Fig. 3.5). From

the composite analysis of airborne Doppler data, Reasor et al. (2013) also confirmed that the shear- relative TC asymmetry is featured by downshear-right convective initiation and a downshear-left precipitation maximum. Moderately deep precipitation peaks at the upshear-left quadrant (Figs. 3.4e,f). Very deep precipitation has double peaks in RI continuing storms (Fig. 3.3f), with the primary peak in the upshear-left quadrant and the secondary peak in the downshear-right quadrant. For RI initial storms (Fig. 3.3e), very deep precipitation peaks in the downshear-left quadrant, similar to W, N, and SI storms. The cyclonic rotation of peaks from shallow to deep precipitation follows the wind direction around the TC center. One may argue that this rotation simply reflects the trajectory of air parcels as they ascend in cyclonic flow, as in Black et al. (2002). However, from Figs. 3.3–3.6, this rotating feature is seen only in RI storms, not in W, N, and SI storms. Therefore, we argue that this may be an indicator of the vortex rapidly strengthening. As a storm rapidly intensifies, it may be more resilient to shear, causing the fall-out of ice particles generated upstream to be increasingly prevalent azimuthally downwind (Hence and Houze 2012).

3.5 Total volumetric rain

The radial distributions of total volumetric rain and total latent heating in Fig. 3.7 illustrate similar patterns for W, N, SI, and RI initial storms, while RI continuing storms have remarkably higher azimuthally averaged total rainfall and latent heating than other intensity change categories. Similarly, previous studies (e.g., Jiang and Ramirez 2013;

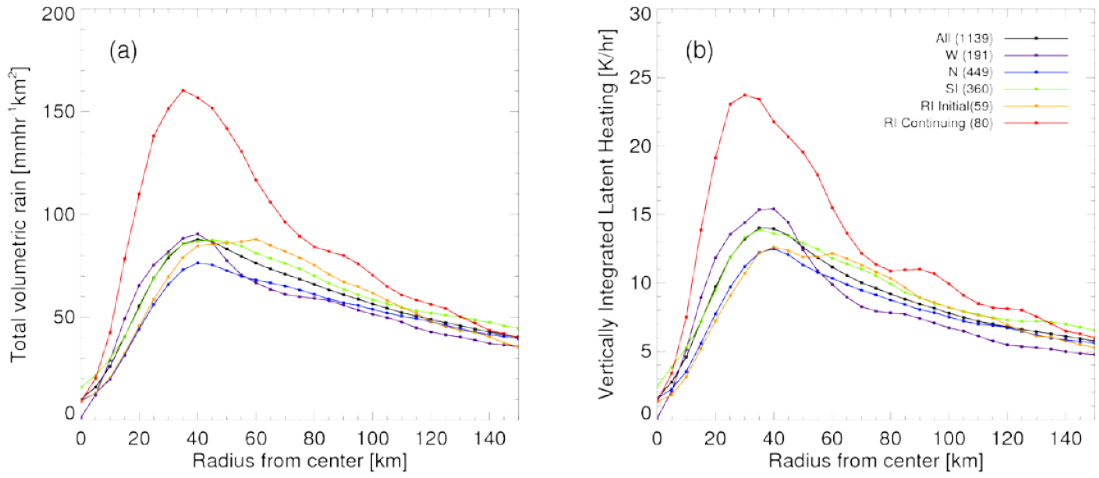

Figure 3.7: Radial distributions of azimuthally averaged (a) total volumetric rain and (b) total vertically integrated latent heating for the total sample and different intensity change categories shown in (b).

Kieper and Jiang 2012) have shown that RI storms have widespread precipitation with high total volumetric rain in the inner-core region. However, this study further indicates that it is RI continuing storms that account for the pronounced difference of total volumetric rain and latent heating between SI and RI storms, as the curves for RI initial and SI storms are very similar. Table 3.5 also shows that in the innermost 100km of the TC center, the mean differences between SI and RI initial storms in total volumetric rain and latent heating are not statistically significant. Without separating RI initial and continuing categories, Jiang and Ramirez (2013) concluded that large total raining area and total volumetric rain in the inner core are necessary conditions of RI. However, our results here indicate that this conclusion is valid only for the RI continuing category.

Table 3.5: Mean values of total volumetric rain (mm $hr^{-1}km^2$) and total vertically integrated latent heating (K hr^{-1}) in each shear-relative quadrant within **100 km** of the TC center. Asterisks in the RI, RI initial, and RI continuing rows represent the statistical significance between SI and RI, SI and RI initial, and RI initial and RI continuing storms, respectively, at the 90% (*), 95% (**), 99% (***), and 99.9% (****) confidence level.

Total volumetric rain	**DR**	**UR**	**UL**	**DL**	**Total**
W	47.00	18.19	45.63	118.03	65.65
N	47.88	20.75	46.27	109.76	62.31
SI	63.52	29.70	53.77	121.63	74.19
RI	71.84	52.15****	90.98****	117.57	92.37****
RI (initial)	61.49	35.54	73.68**	108.57	73.96
RI (continuing)	79.47	64.40***	103.74**	124.21	105.94****
All	55.60	26.98	53.99	115.85	70.29
Vertically integrated LH	**DR**	**UR**	**UL**	**DL**	**Total**
W	6.94	2.61	6.86	18.20	9.78
N	7.17	3.08	6.79	17.44	9.47
SI	9.75	4.19	8.08	19.33	11.10
RI	10.66	7.24****	12.63****	16.70	13.03**
RI (initial)	8.95	4.50	10.64	15.52*	10.34
RI (continuing)	11.92	9.27****	14.10	17.57	15.02****
All	8.37	3.86	7.92	18.08	10.47

The composite shear-relative distributions of total volumetric rain for various intensity change categories are displayed in Fig. 3.8. Consistent with previous studies, the maximum total volumetric rain is downshear and to the left of the shear vector (e.g., Chen et al. 2006; Wingo and Cecil 2010). As shown in Figs. 3.8a–d, the maximum total volumetric rain occurs in the downshear-left quadrant in all intensity change categories except in the RI continuing category, in which the maximum is mainly upshear left. These distributions are similar to the mean rain rates in Figs. 16–18 of Wingo and Cecil (2010) and the averaged vertically integrated latent heat in Fig. 9 of ZJ14. Although the

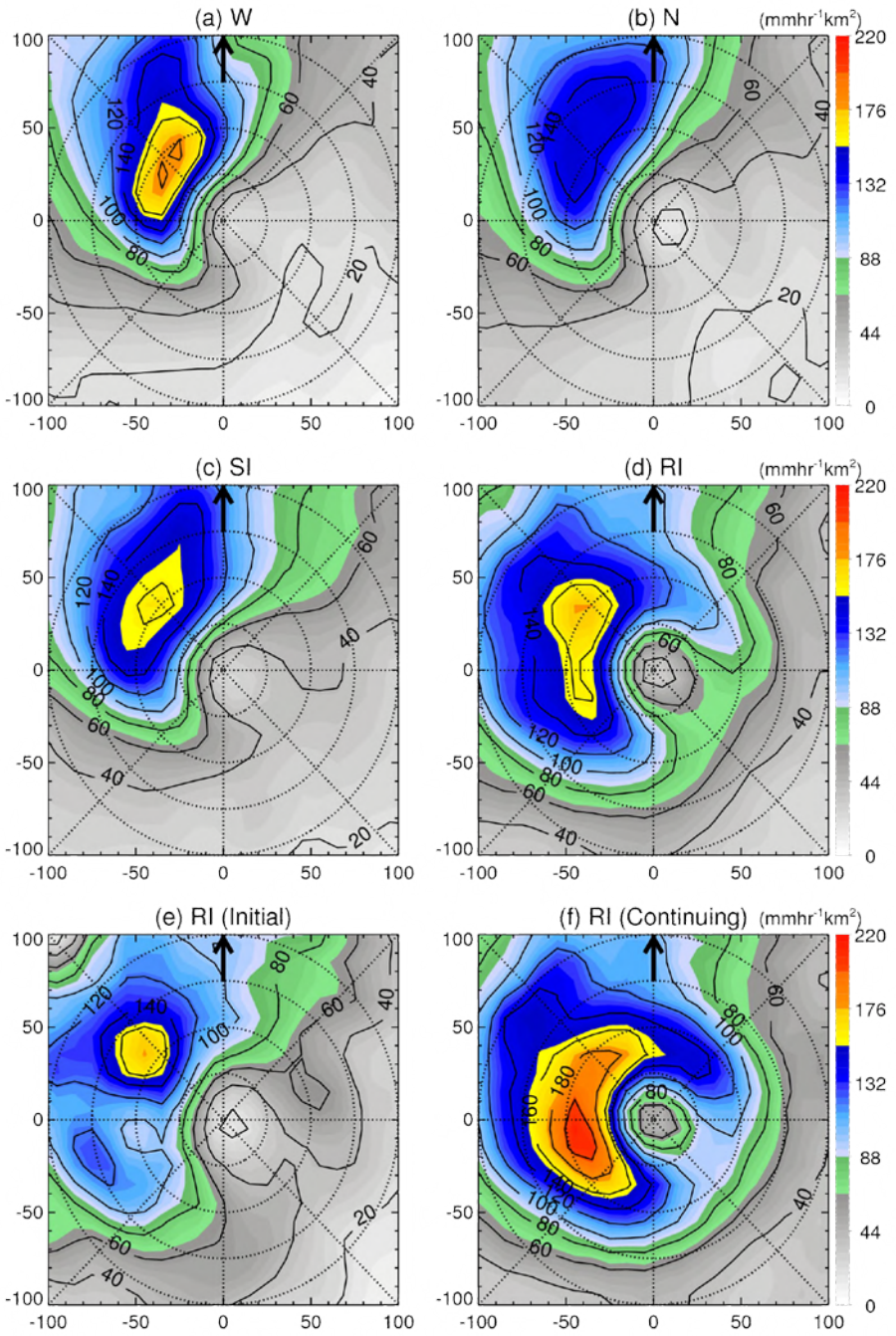

Figure 3.8: Composite shear-relative distribution of the averaged total volumetric rain for (a) W, (b) N, (c) SI, (d) RI, (e) RI initial, and (f) RI continuing. The black arrow represents the orientation of the vertical wind shear vector. The 25-, 50-, 75-, and 100-km radii are shown as dotted rings.

mean inner-100-km total volumetric rain is similar for SI and RI initial storms, a substantial difference is observed in the upshear-left quadrant. An almost-closed ring of 40mm h^{-1} km^2 total volumetric rain is found surrounding the storm center for RI initial storms, but only 20–30mm h^{-1} km^2 of total volumetric rain surrounds the storm center for SI storms. For RI continuing storms (Fig. 3.8f), the maximum total volumetric rain is located in the upshear-left quadrant between 25 and 50km of the center and peaking at about 200mm h^{-1} km^2, with a ring of at least 100mm h^{-1} km^2 extending completely around the center. The mean total volumetric rain (latent heating) within 100km of the storm center in RI continuing storms is about 30mm h^{-1} km^2 (4–5 K h^{-1}) higher than those in SI and RI initial storms (Table 3.5), similar to Fig. 3.7.

3.6 Contribution to total volumetric rain and total latent heating

To quantify the contribution of each type of precipitation to total volumetric rain, Table 3.6 shows the mean values of the percentage of total rainfall from four kinds of precipitation, which is averaged within 100 km of the TC center. It is found that moderate precipitation accounts for about 63% of total volumetric rain, while the other three kinds of precipitation together account for only 37%. Overall, the percentage of total rainfall from moderate precipitation is about 11, 5, and 3 times greater than that from very deep precipitation, moderately deep precipitation, and shallow precipitation, respectively (Tables 3.6 and 3.7). Similar results are found for the contribution to total latent heating.

Note that the total percent occurrence of all four types of precipitation within the 100-km radius is about 52% (Table 3.4). Therefore, the relative pixel-based contribution

Table 3.6: Composite mean values of the convective contribution to total volumetric rain in each shear-relative quadrant. Averaged within 100 km of the TC center. Asterisks in the RI, RI initial, and RI continuing rows represent the statistical significance between SI and RI, SI and RI initial, and RI initial and RI continuing storms, respectively, at the 90% (*), 95% (**), 99% (***), and 99.9% (****) confidence level. Unit is %.

Very deep convection	**DR**	**UR**	**UL**	**DL**	**Total**
W	1.76	4.08	7.71	4.57	4.59
N	3.50	1.87	8.21	7.70	6.38
SI	2.71	4.29	9.34	8.53	6.85
RI		0.66	4.03	3.88*	3.28**
RI (initial)	2.95	0.37**	4.13	6.17	4.15
RI (continuing)	3.31	0.80	3.97	2.44	2.79
All	2.92	2.70	7.62	6.92	5.75
Moderately deep convection	**DR**	**UR**	**UL**	**DL**	**Total**
W	9.05	8.41	12.37	12.92	11.68
N	11.50	10.04	13.85	15.82	13.96
SI	10.26	7.81	12.94	14.54	12.46
RI	9.42	6.53*	12.98	9.63	10.06
RI (initial)	7.66	4.29	16.07	8.69**	9.90
RI (continuing)	10.40*	7.62***	11.29	10.22	10.14
All	10.39	8.25	13.18	14.11	12.48
Moderate convection	**DR**	**UR**	**UL**	**DL**	**Total**
W	68.83	58.67	54.22	64.77	63.03
N	64.53	59.97	53.56	61.40	60.34
SI	68.62	63.06	57.28	64.10	63.69
RI	64.37	68.27	67.23	70.37**	67.94***
RI (initial)	63.20	63.50*	62.38**	66.46	64.30*
RI (continuing)	65.02	70.60*	69.89	72.82	70.01
All	66.57	62.83	57.63	64.00	63.08
Shallow convection	**DR**	**UR**	**UL**	**DL**	**Total**
W	20.31	28.67	25.63	17.73	20.69
N	20.41	27.98	24.31	15.06	19.32
SI	18.35	24.74	20.38	12.80	17.00
RI	22.98	24.46***	15.74	16.11	18.72**
RI (initial)	26.12	31.70	17.37***	18.65	21.65
RI (continuing)	21.24*	20.92***	14.84	14.52	17.06
All	20.06	26.10	21.52	14.95	18.68

Table 3.7: Composite mean values of the percentage of four kinds of convection to total convection and total volumetric rain. Averaged within **100 km** of the TC center. Unit is %.

% to total convection	**W**	**N**	**SI**	**RI**	**RI (initial)**	**RI (continuing)**	**Total**
Very deep convection	1.32	1.40	1.44	0.75	0.86	0.68	1.30
Moderately deep convection	5.36	5.51	4.67	4.15	3.84	4.36	4.98
Moderate convection	51.11	49.96	52.84	53.57	50.94	55.41	51.70
Shallow convection	42.21	43.14	41.04	41.53	44.36	39.55	42.03
Very deep + moderately deep convection	*6.68*	*6.91*	*6.11*	*4.9*	*4.7*	*5.04*	*6.28*
Moderate + shallow convection	*93.32*	*93.1*	*93.88*	*95.1*	*95.3*	*94.96*	*93.73*
% to total volumetric rain	**W**	**N**	**SI**	**RI**	**RI (initial)**	**RI (continuing)**	**Total**
Very deep convection	4.59	6.38	6.85	3.28	4.15	2.79	5.75
Moderately deep convection	11.68	13.96	12.46	10.06	9.90	10.14	12.48
Moderate convection	63.03	60.34	63.69	67.94	64.30	70.01	63.08
Shallow convection	20.69	19.32	17.00	18.72	21.65	17.06	18.68
Very deep + moderately deep convection	*16.27*	*20.34*	*19.31*	*13.34*	*14.05*	*12.93*	*18.23*
Moderate + shallow convection	*83.72*	*79.66*	*80.69*	*86.66*	*85.95*	*87.07*	*81.76*
% to total latent heat	**W**	**N**	**SI**	**RI**	**RI (initial)**	**RI (continuing)**	**Total**
Very deep convection	7.21	9.47	10.71	4.90	6.32	4.09	8.83
Moderately deep convection	14.52	17.14	15.23	12.99	13.25	12.85	15.47
Moderate convection	63.21	60.10	62.10	68.14	65.07	69.89	62.46
Shallow convection	15.06	13.29	11.96	13.97	15.35	13.18	13.24
Very deep + moderately deep convection	*21.73*	*26.61*	*25.94*	*17.89*	*19.57*	*16.94*	*24.3*
Moderate + shallow convection	*78.27*	*73.39*	*74.06*	*82.11*	*80.42*	*83.07*	*75.7*

to total precipitation of very deep precipitation, moderately deep precipitation, moderate

precipitation, and shallow precipitation is about 1%, 5%, 52%, and 42%, respectively (Table 3.7). Comparing these numbers with the percentage contributions to total volumetric rain and total latent heating shown in Table 3.7, we can see that both very deep precipitation and moderately deep precipitation have a disproportionately higher contribution to total volumetric rain and total latent heating. In the innermost 100km, about 1% (5%) of total convective pixels is very deep precipitation (moderately deep precipitation), but these pixels contribute about 6% and 9% (12% and 15%) to the total rainfall and total latent heating, respectively. However, for RI versus non-RI categories, Table 3.7 indicates that the percentage of total volumetric rain (total latent heating) contributed by moderately to very deep precipitation is smaller in RI storms (including RI initial and RI continuing) than in non-RI storms (including W, N, and SI), while the opposite is true for shallow to moderate precipitation. This suggests that the contribution of shallow to moderate precipitation to the total rainfall and latent heating is more important to the initiation and maintenance of RI.

The corresponding composite shear-relative distributions of the percentage of the total volumetric rain from four kinds of precipitation are shown in Figs. 3.9–3.12. The distributions for the total latent heating are quite similar and thus not shown here, as mentioned in the introduction. Figure 3.9 illustrates that the maximum contribution of very deep precipitation to total volumetric rain is located in the upshear-left quadrant for all intensity change categories except for the RI initial category, in which the maximum is located downshear- left. RI continuing storms (Fig. 3.9f) have a second maximum

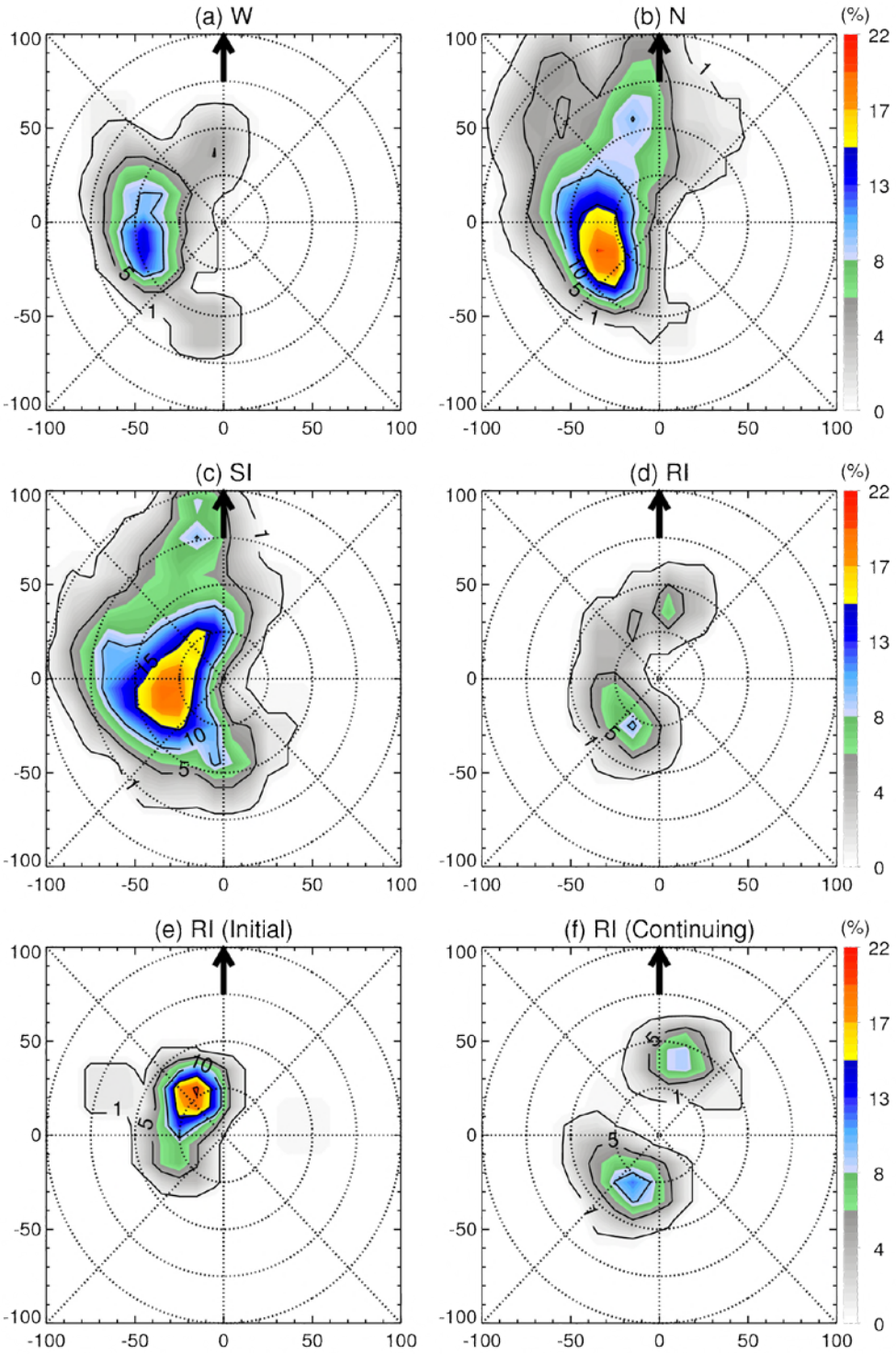

Figure 3.9: As in Figure 3.8, but for the percentage of total volumetric rain from very deep precipitation.

located in the downshear-right quadrant. Averaged within the innermost 100 km of the TC

center, RI continuing storms have the lowest percentage of total volumetric rain from very deep precipitation. The difference between SI and RI storms in the convective contribution to total rainfall is about 3.5%, which is significant at the 95% confidence level (Table 3.6).

Figure 3.10 displays the shear-relative distribution of the percentage of total volumetric rain from moderately deep precipitation. The maximum convective contribution is upshear-left for all intensity change categories except for the weakening storms (Fig. 3.10a), in which the maximum is downshear left. Overall, RI storms have higher contributions closer to the storm center. From Table 3.6, we can also see that when averaged for all quadrants, moderately deep precipitation accounts for similar percentages of total volumetric rain for RI initial, RI continuing, and SI, but some differences are seen in individual quadrants.

Within the innermost 100 km, moderate precipitation accounts for about 68% of total volumetric rain for all RI storms but only 60%–64% for neutral, weakening, and SI storms (Table 3.6). A pronounced difference (about 4%, significant at the 99% confidence level) is observed between SI and RI storms. The quadrant-mean values of the contribution to total rainfall in Table 3.6 indicates that in the upshear-left quadrant, moderate precipitation accounts for approximately 62% to the total volumetric rain for RI initial storms, which is about 5% higher than SI storms (significant at the 95% confidence level). In the upshear-right quadrant, the contribution is 7% higher for RI continuing storms than RI initial storms (significant at the 90% confidence level). The corresponding

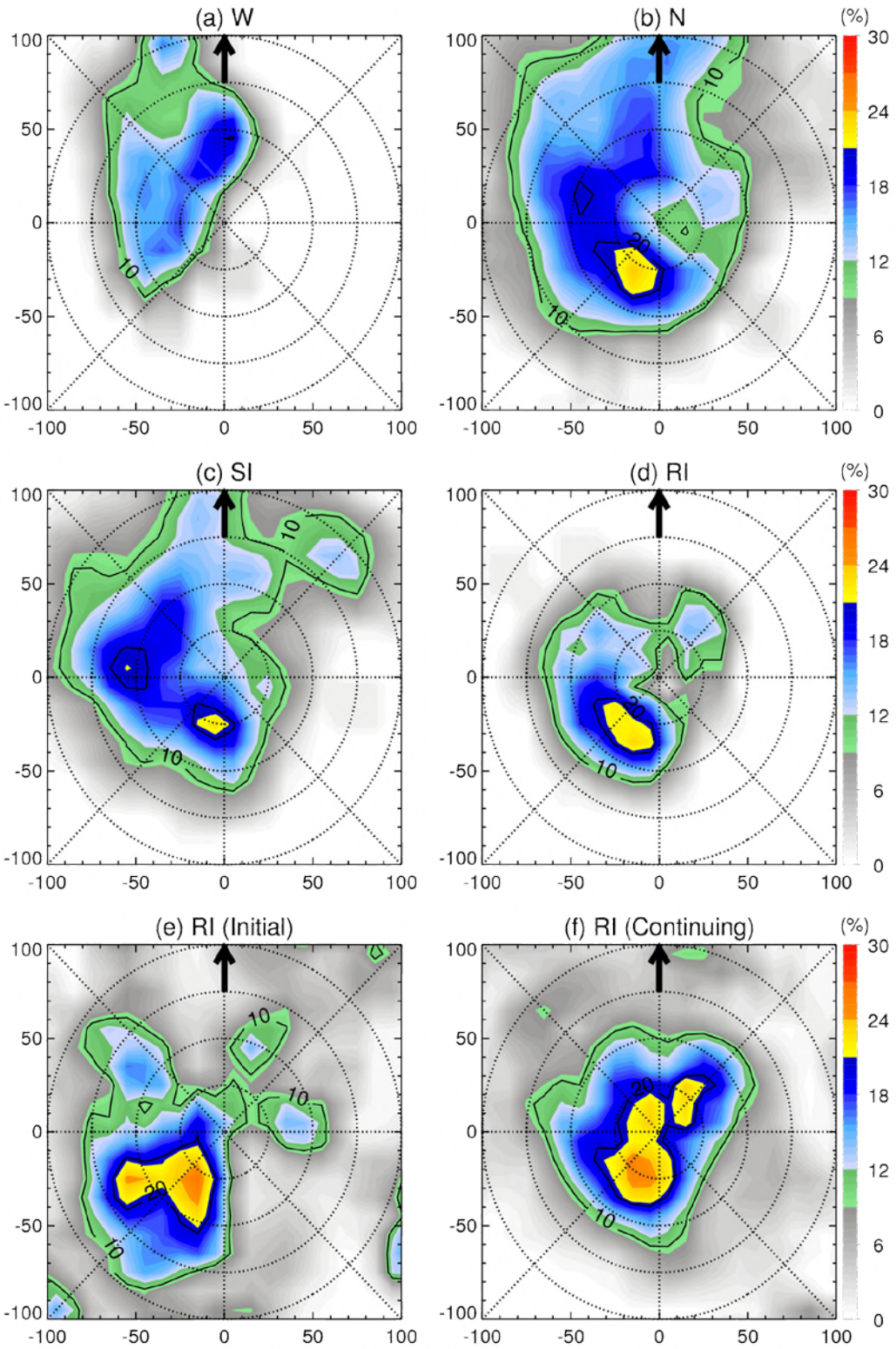

Figure 3.10: As in Figure 3.9, but for moderately deep precipitation.

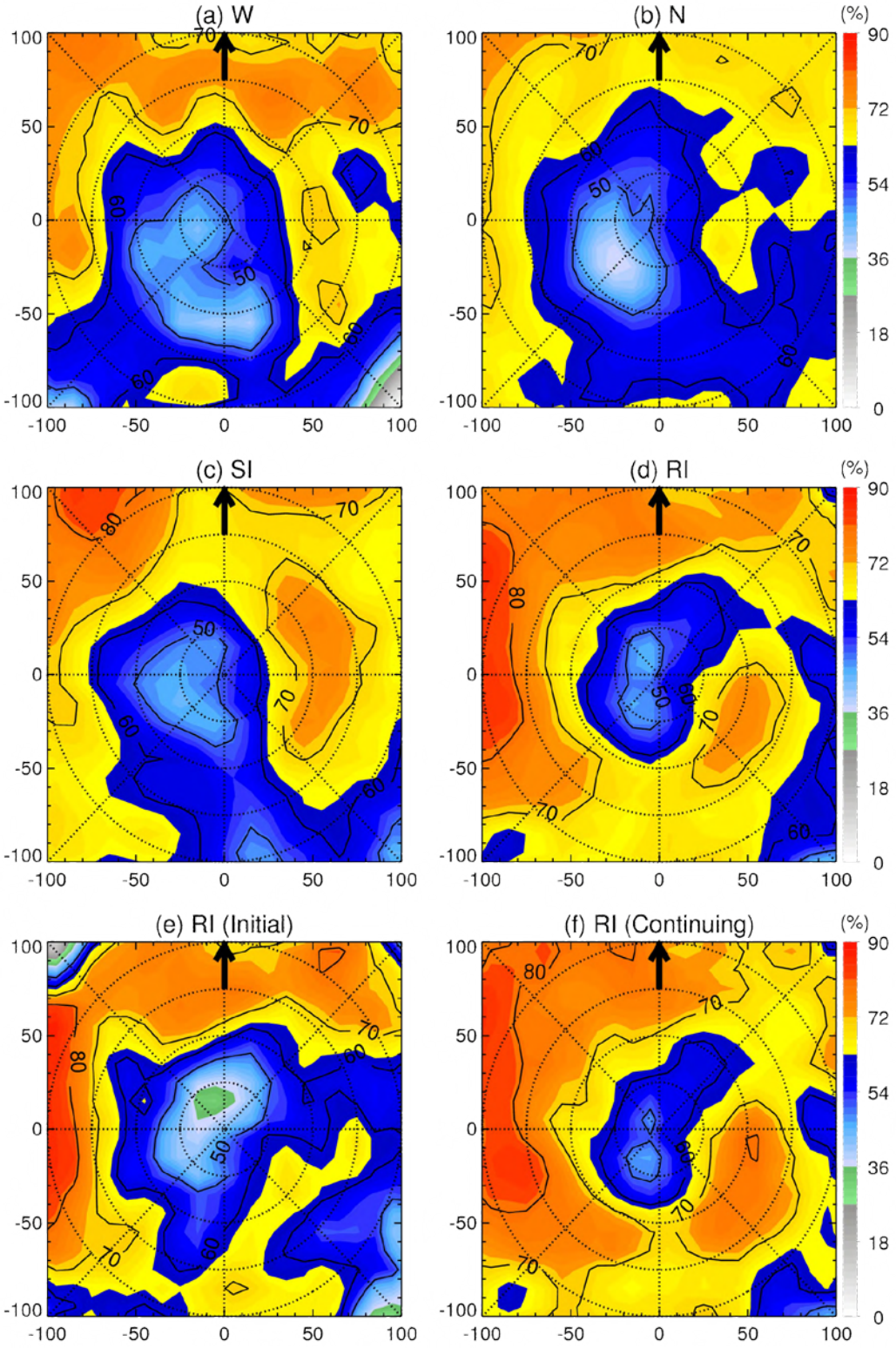

Figure 3.11: As in Figure 3.9, but for moderate precipitation.

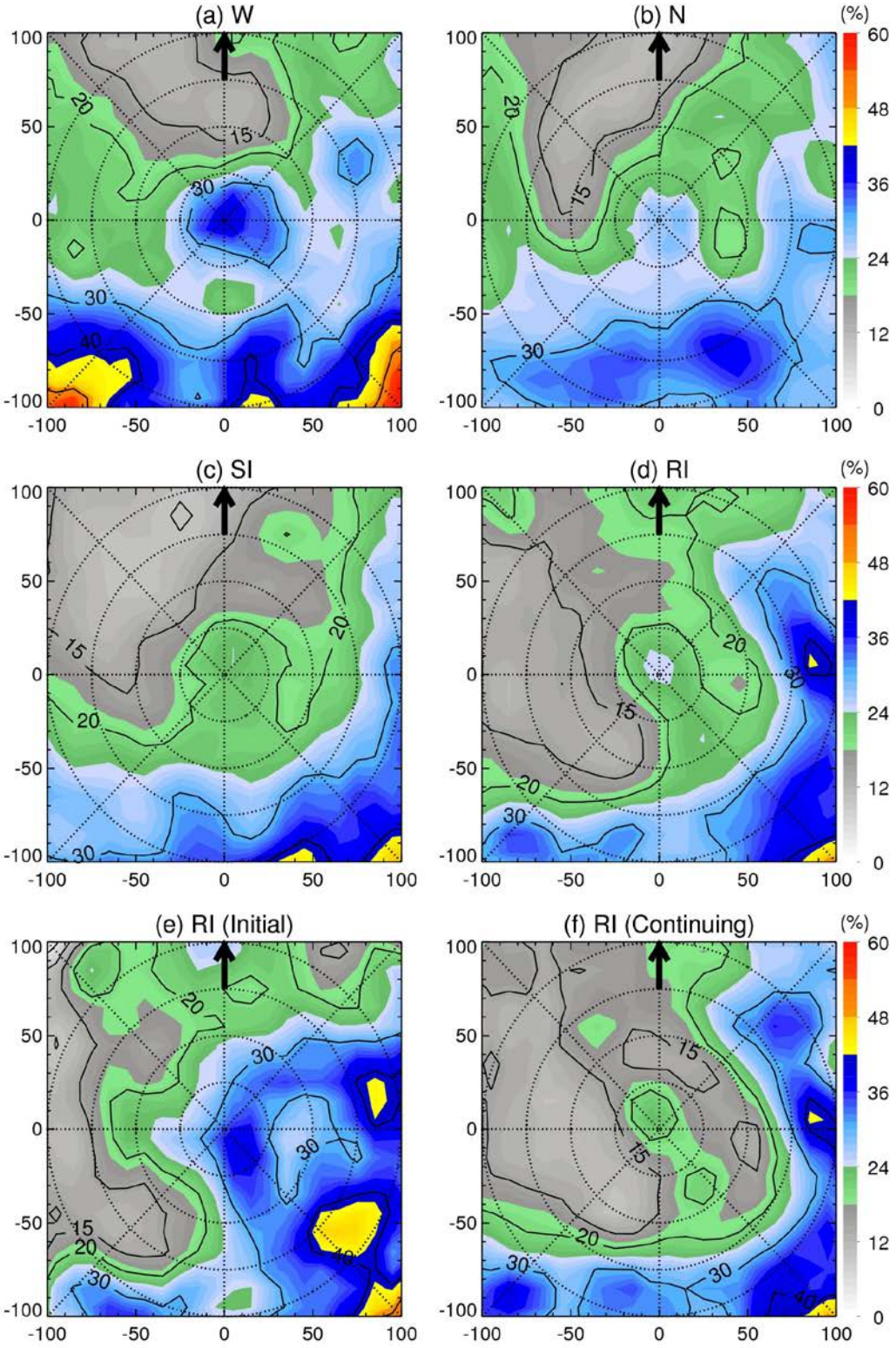

Figure 3.12: As in Figure 3.9, but for shallow precipitation.

shear-relative distribution in Fig. 3.11 illustrates that both RI initial (Fig. 3.11e) and RI continuing storms (Fig. 3.11f) have a much larger area with at least 70% total volumetric rain from moderate precipitation than other intensity change categories. A more symmetric pattern is seen for RI continuing storms (Fig. 3.11f).

Averaged within the innermost 100km of the TC center, about 19% of the total volumetric rain is from shallow precipitation (Table 3.5). But it should be noted hat the definition of shallow precipitation in this study does not involve any ice phase. Thus, the rain rate from shallow precipitation may be underestimated as a result of the TRMM PR 2A25 algorithm (Iguchi et al. 2000). Although the percent occurrence of shallow precipitation is much higher in RI storms than non-RI storms, shallow precipitation accounts for similar percentages to the total volumetric rain for RI and non-RI storms. This is mainly because of the higher contribution to the total volumetric rain from moderate precipitation for all RI storms. The corresponding composite shear- relative distribution in Fig. 3.12 illustrates that the upshear or upshear-right quadrants are favored in all intensity change categories in the contribution to the total rain- fall. For weakening storms (Fig. 3.12a), a large area of 30% rainfall from shallow precipitation is observed within the innermost 25-km region.

3.7 Discussion

Consistent with previous satellite-based statistical studies (Jiang 2012; Kieper and Jiang 2012; Jiang and Ramirez 2013; ZJ14), results in this study suggest that widespread relatively symmetric shallow to moderate precipitation is more important in initiating and

maintaining RI in the next 24 h than moderately to very deep convection. This seems to conflict with the observational case studies mentioned in the introduction (Reasor et al. 2009; Guimond et al. 2010; Molinari and Vollaro 2010; Nguyen and Molinari 2012; Reasor and Eastin 2012), which emphasized the role of asymmetric very deep convection in RI. However, after careful scrutiny, it is found that in all of these observational case studies, the occurrence of very deep convection was observed within 24h before an RI event ends. This is totally different from the definition of RI used in this study and previous satellite-based statistical studies mentioned above.

As mentioned in section 3.3.2, RI typically occurs as an event, which is defined as multiple, continuous, and over- lapping 24-h periods in which the intensity increases in each period by 30 kt or more (Kieper and Jiang 2012). Each 24-h period within an RI event corresponds to one RI case as defined by Kaplan and DeMaria (2003). Based on a statistics using 1998–2013 global best-track data, the mean and median duration of all RI events is about 36 h with a minimum of 24 h [this is by the definition of Kaplan and DeMaria (2003)] and a maximum of 78 h. Figure 3.13 illustrates a schematic of a typical RI event, with the corresponding RI initial and RI continuing periods as defined in this study and an additional period called RI ending. The RI ending category includes the period during which an RI event will end within 24h. Unlike RI initial and RI continuing categories, which require at least 24h before an RI event ends, the RI ending category has no predictive power and may correspond to the weakening, neutral, or SI category as defined in this study.

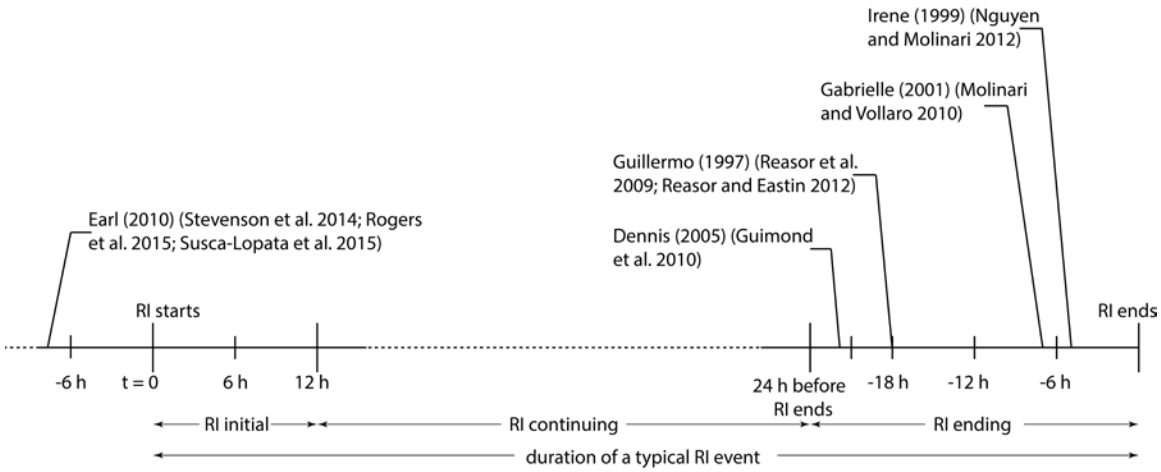

Figure 3.13: Schematic of RI initial, RI continuing, and RI ending periods within a typical RI event. The relative time when the very deep convection was observed in each of the observational studies mentioned in section 4 is placed on the timeline in the RI ending period and before RI. Please see text for details.

In the above-mentioned observational case studies, very deep convection that was claimed to play a role in RI was all in the RI ending period. As illustrated on the timeline in Figure 3.13, deep convection observed in Hurricane Guillermo (1997) by aircraft during 1845 UTC 2 August– 0012 UTC 3 August was only observed about 18 h before the RI event ended (Reasor et al. 2009; Reasor and Eastin 2012). Guimond et al. (2010) reported that the ER-2 aircraft observed a hot tower in Hurricane Dennis (2005), but it occurred around 22 h before the RI event ended. A hot tower occurred 5h before the RI ended for Hurricane Irene (1999) in Nguyen and Molinari (2012). A vortical hot tower was observed 7 h before the RI event of Tropical Storm Gabrielle (2001) ended (Molinari and Vollaro 2010). There are several recent studies about Hurricane Earl (2010) (Stevenson et al. 2014; Rogers et al. 2015; Susca-Lopata et al. 2015) showing asymmetric deep convection around 6–9h be- fore the onset of RI (Fig. 3.13). At that time Earl was in the slowly intensifying

stage. As seen in Figure 3.3c of this study, very deep convection does increase in SI storms. So the findings of these Earl studies are consistent with the current study.

Based on the findings of this study and above-mentioned observational case studies, Figure 3.14 presents a hypothesized sequence of events providing some mechanisms to describe the importance of shallow–moderate precipitation, as opposed to deep–very deep convection, to RI. Before a storm undergoes RI, it is usually in the slowly intensifying or steady-state stage. At this time, isolated very deep convection is often observed (Fig. 3.3c; Stevenson et al. 2014; Rogers et al. 2015; Susca-Lopata et al. 2015), which is possibly due to high wind shear (Molinari and Vollaro 2010; Susca-Lopata et al. 2015), vortex misalignment (Stevenson et al. 2014; Rogers et al. 2015; Susca-Lopata et al. 2015), or dry environment (Stevenson et al. 2014). At the onset of RI (RI initial stage), increased shallow and moderate precipitation is seen, especially in the upshear quadrants (Figs. 3.5e and 3.6e; Susca-Lopata et al. 2015), inducing moistening and preconditioning for deep convection (Johnson et al. 1999), vortex alignment (Chen and Gopalakrishnan 2015), axisymmetrization (Kieper and Jiang 2012; Susca-Lopata et al. 2015), and more latent heat release. As RI continues, increased moderate to very deep precipitation is observed, producing much higher total volumetric rain and latent heating release (Figs. 3.4f, 3.5f, and 3.6f; Table 3.5). The factors of very deep convection closer to the storm center (Figs. 3.3f and 3.4f) and the axisymmetrization of the precipitation

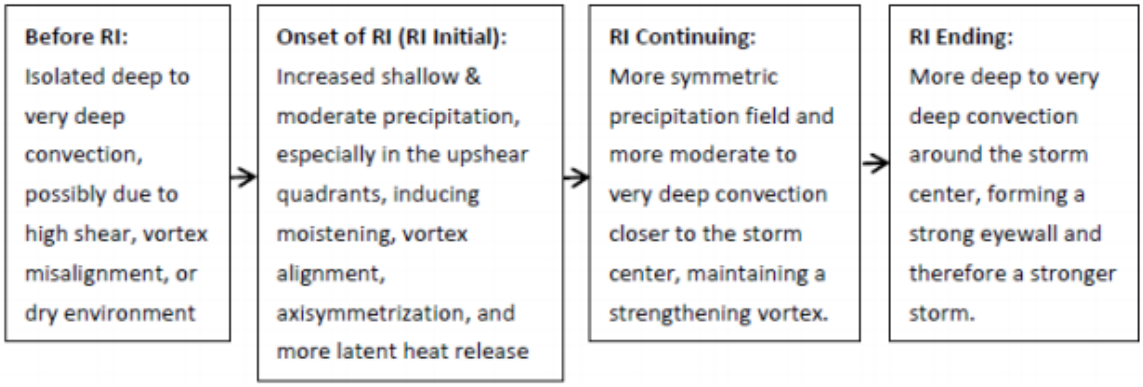

Figure 3.14: A hypothesized sequence of events providing some mechanisms before and during RI that describes the importance of shallow–moderate precipitation as opposed to deep–very deep convection. Please refer to Figure 13 for the definition of RI initial, RI continuing, and RI ending.

field (Fig. 3.8f) help maintain the vortex's rapid strengthening for more than 24 h following. At the RI ending stage (< 24 h before RI ends), there is a higher chance of having more deep to very deep convection around the storm center (Reasor et al. 2009; Guimond et al. 2010; Molinari and Vollaro 2010; Nguyen and Molinari 2012; Reasor and Eastin 2012), which helps form a strong eyewall and lead to a stronger storm.

Using aircraft Doppler radar data, Rogers et al. (2013) found that intensifying storms have a larger percentage of convective bursts within 1 to 2 times of the RMW than steady-state storms. Their definition of intensifying storms contains RI and part of the SI categories in this study. From Figures. 3.2–3.3 in this study, we can see that very deep precipitation (similar to their convective burst definition) does have higher peaks, which are located closer to the center in RI and SI storms than in neutral and weakening storms (similar to their steady-state definition). However, after integrating with the 100-km radius [about two RMW; see section 3.4.2 for details], we found that both the frequency of very

deep precipitation and its contribution to total volumetric rain and total latent heating are much less in RI storms than those in neutral and weakening storms (Table 3.7). More interestingly, Table 3.7 does show that SI storms have a higher frequency and larger percent contributions to total volumetric rain and total latent heating from very deep precipitation than RI, neutral, and weakening storms. This suggests that 1) Rogers et al.'s (2013) intensifying storms might contain more SI storms than RI storms, which is possibly true owing to the limitation of aircraft data, and 2) very deep convection seems to play a more important role in slowly intensifying storms than in RI storms.

Another important point from the introduction is to examine the percent occurrence of total precipitation (including shallow, moderate, moderately deep, and very deep precipitation as defined in section 3.3.3) in order to test if the cyan and pink color ring in the NRL 37-GHz color product found by Kieper and Jiang (2012) is precipitative. To do this, it was necessary to degrade the PR pixel size into TMI 37-GHz equivalent footprint size. The shear-relative distributions of the percent occurrence of total precipitation degraded to the 37-GHz footprint size are shown in Figure 3.15. As expected, the downshear-left quadrant is favored for all TC intensity change categories (e.g., Corbosiero and Molinari 2002; Chen et al. 2006). The precipitative/convective frequency, as well as the degree of symmetry, increases in order from weakening/neutral, SI, RI initial, to RI continuing storms. A ring of about 90% occurrence of all precipitation is observed for RI continuing storms (Fig. 3.15f), which is analogous to the cyan and pink

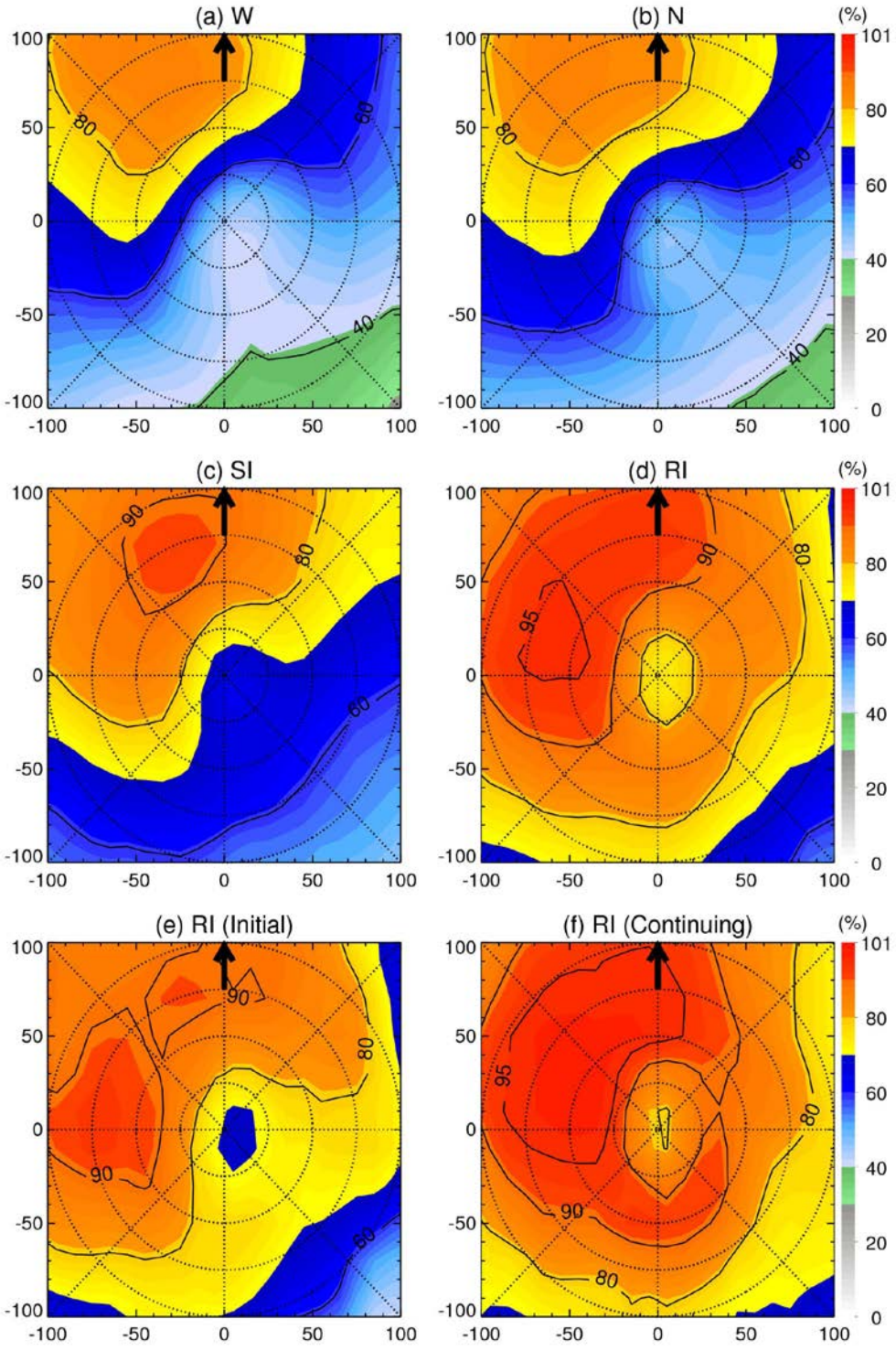

Figure 3.15: As in Figure 3.3, but for total precipitation degraded to the 37-GHz footprint size.

ring feature recognized in Kieper and Jiang (2012) for RI storms. In this study, at least 20-

dBZ PR reflectivity at different levels is required for all four types of precipitation. Therefore, all the precipitation defined in this study contains precipitation-sized particles.

One may ask how many cases that make up the RI composites in Figures. 3.3–3.6 and 3.15 have a 37-GHz cyan and pink ring. As shown in Table 3.2, 42 (70) out of the 59 (80) RI initial (continuing) cases have a 37-GHz ring within the TMI swath. Therefore, 112 out of 139 total RI cases (about 80%) have the ring feature for the 14-yr global TC data from the TRMM PR. The percentage is similar to what Kieper and Jiang (2012) found for Atlantic TCs during 2002–07. To carefully compare the 37-GHz cyan and pink ring with the PR reflectivity field, a subset of overpasses is further selected for cases with the cyan and pink ring directly covered by the PR swath. As shown in Table 3.2's last column, a total of 83 cases meet this criterion, including 30 RI initial and 53 RI continuing overpasses.

Two examples of such overpasses are shown in Figures. 3.16 and 3.17 for an RI continuing case and an RI initial case, respectively. The Atlantic Hurricane Danielle (2004) case shows a 37-GHz cyan ring in the inner edge around the storm center with a pink arc on top of the eastern half of the cyan ring (Fig. 3.16a), while the northwestern Pacific Typhoon Marenti (2004) overpass also shows a 37-GHz cyan and pink ring, with the pink arc on the southwest side of the center (Fig. 3.17a). A complete 20-dBZ radar reflectivity ring is seen in both the Danielle and Marenti overpasses (Figs. 3.16b and 3.17b), resembling the 37-GHz cyan and pink ring. Harnos and Nesbitt (2011) claimed that they found a ring for RI storms where 85-GHz PCT $\leq$ 250 K. However, in the 14-yr

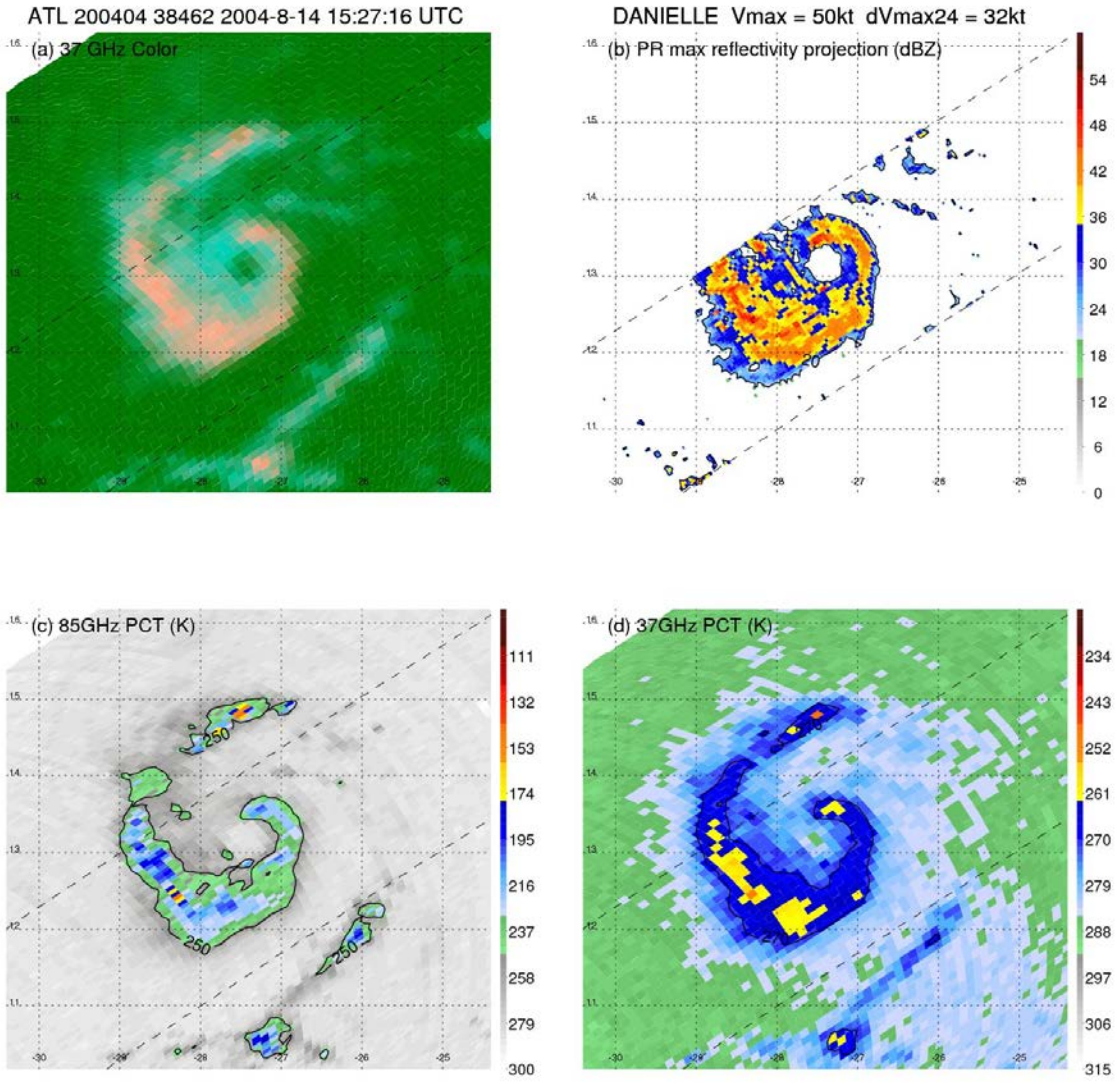

Figure 3.16: An RI continuing case with a 37-GHz color cyan and pink ring observed by TRMM for Hurricane Danielle (2004) at 1527 UTC 14 August in the Atlantic (ATL) basin. (a) TMI 37-GHz color, (b) PR maximum reflectivity projection with 20-dBZ contour, (c) TMI 85-GHz PCT with 250 K contour, and (d) TMI 37-GHz PCT with 270 K contour. The Vmax and 24-h future intensity change (dVmax24) are indicated at the top of (b).

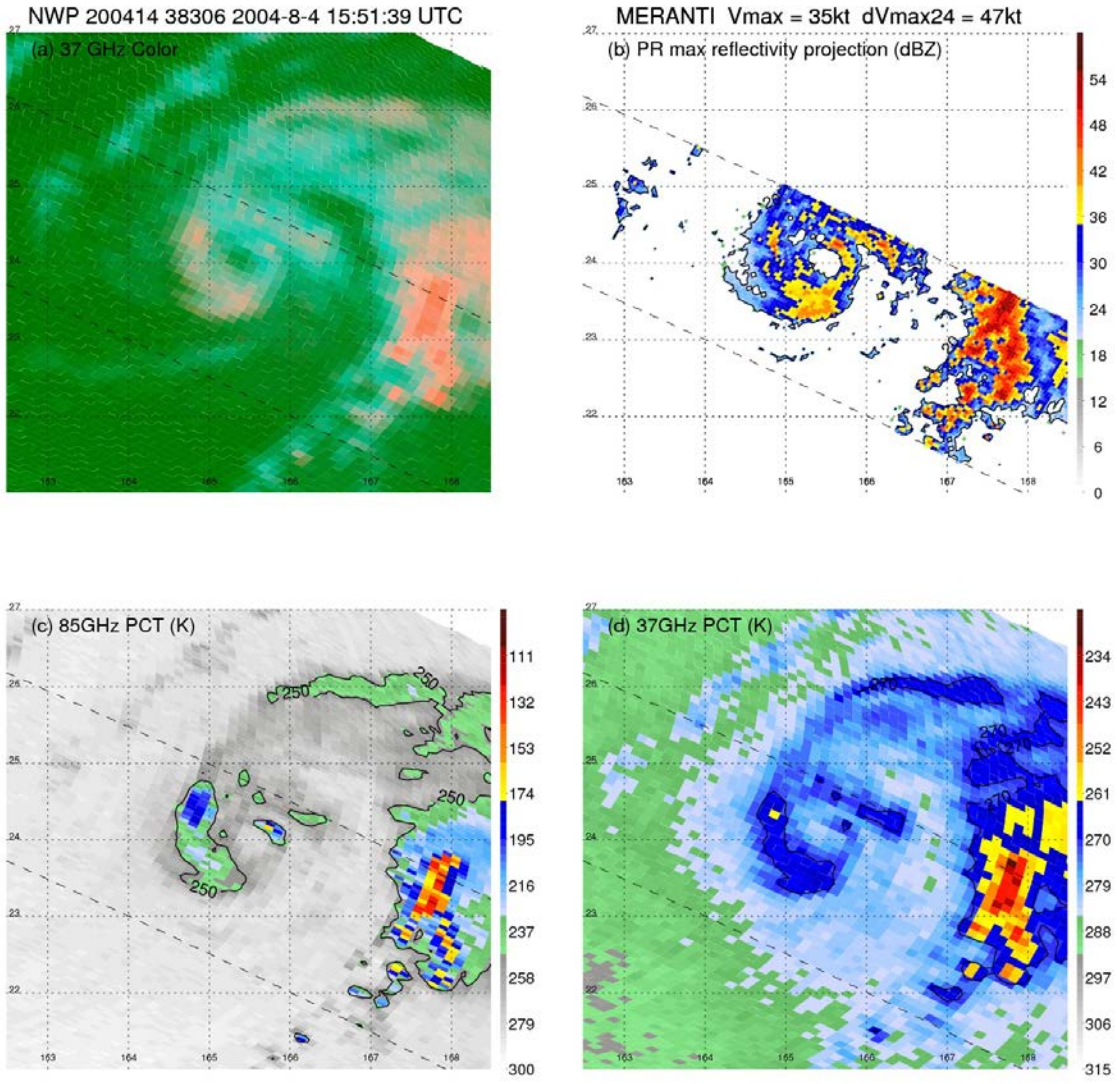

Figure 3.17: As in Figure 3.16, but for an RI initial case for Typhoon Meranti (2004) at 1551 UTC 4 August in the northwestern Pacific (NWP) basin.

TRMM TC dataset that we examined, there are about 80% of RI cases with a 37-GHz cyan and pink ring and a 20-dBZ radar ring (when the inner core is covered by the PR swath). But most of these cases do not have a ring where 85-GHz PCT ≤ 250 K, as shown in Figures 3.16c and 3.17c. For comparison, Table 3.2 also shows that only 28 out of the 139 RI cases (about 20%) have a ring where 85-GHz PCT ≤ 250 K within the TMI swath. The pink color in the 37-GHz color product roughly corresponds to 37-GHz PCT ≤ 270 K, which is also roughly equivalent to 85-GHz PCT ≤ 250 K, as you can see by comparing Figure 3.16c with Figure 3.16d and Figure 3.17c with Fig. 3.17d. As pointed out in section 3.2, the pink color simply indicates precipitation within ice, not necessarily deep convection, as indicated by Lee et al. (2002). Note that we define 85-GHz PCT by following Spencer et al. (1989) and 37-GHz PCT by following Cecil et al. (2002).

Using the 83 RI cases with a 37-GHz cyan and pink ring seen within the PR swath, Figure. 3.18 shows the composite shear-relative distributions of the percent occurrence of total precipitation, total-minus-shallow precipitation, 37-GHz cyan and pink color, and 85-GHz PCT ≤ 250 K. Figures 3.18a, b are degraded to the 37-GHz footprint size in order to get the equivalent radar reflectivity field that the 37-GHz channel sees. An almost-closed 95% ring is seen in both Figs. 3.18a, c, indicating that the 37-GHz cyan and pink ring is essentially a radar echo ring containing at least 20-dBZ reflectivity. It is therefore concluded that the 37-GHz ring is precipitative. Note that the composite ring in Fig. 3.18c is not a 100% ring (even each of the 83 individual case has a ring) mainly because of the TC size difference and some small dis- location of the storm center. If shallow precipitation is excluded, the maximum value for the precipitative ring dropped

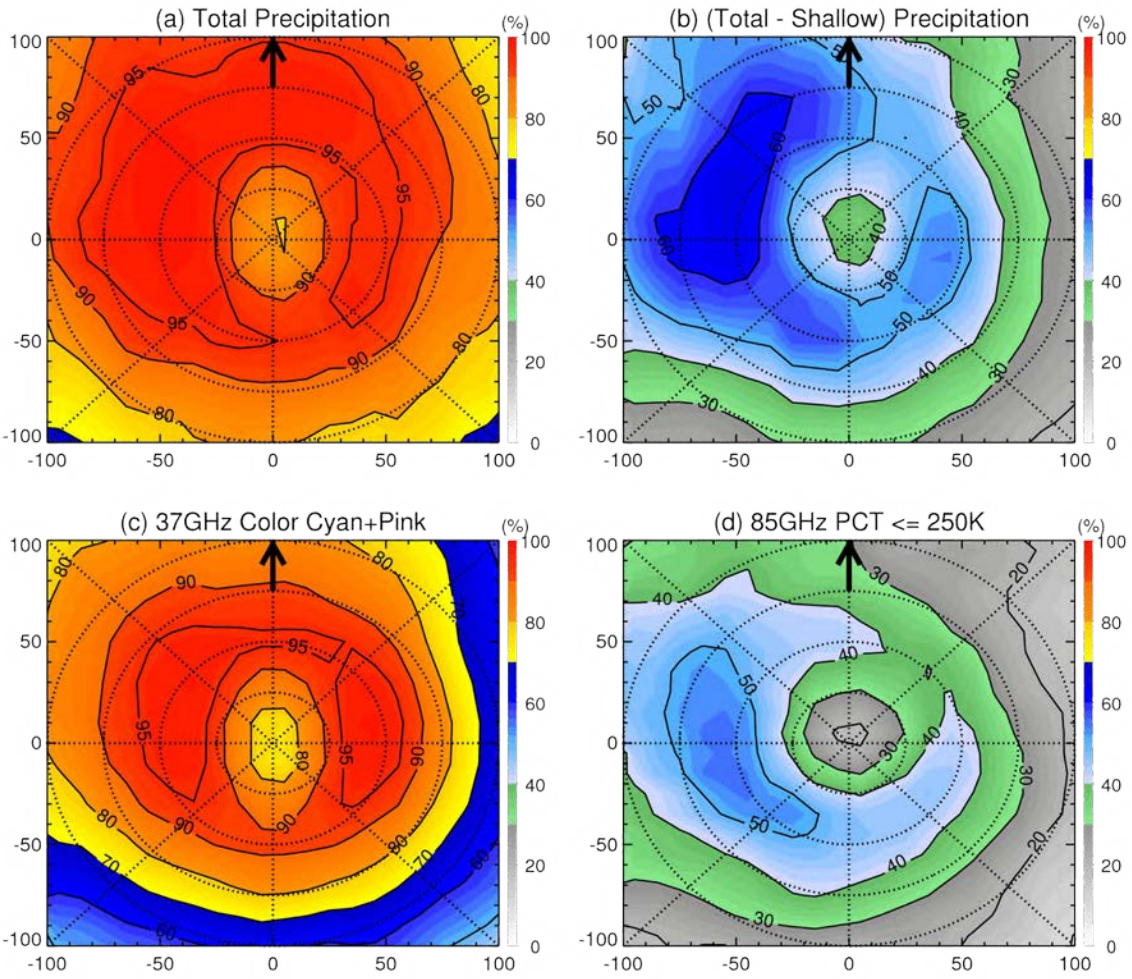

Figure 3.18: Composite shear-relative distribution of the percent occurrence of (a) total precipitation (b) total minus shallow precipitation, (c) cyan and pink color on the 37-GHz color product, and (d) 85-GHz PCT ≤ 250 K for the 83 RI cases (including RI initial and RI continuing) with a 37-GHz cyan and pink ring seen within the PR swath (see Table 3.2). The black arrow represents the orientation of the vertical wind shear vector. The 25-, 50-, 75-, and 100-km radii are shown as dotted rings.

to 40% (Fig. 3.18b). The 85-GHz PCT ≤ 250 K occurrence only has a 30% closed ring around the storm center (Fig. 3.18d), indicating that the so-called 85-GHz convective ring is not actually a good predictor for RI. If both shallow and moderate precipitation are excluded (only considering moderately deep and very deep precipitation), a ring of 5% occurrence is found (not shown), similar to the frequency of deep convection in ZJ14 (see their Fig. 8e). This implies that the 37-GHz ring feature in Kieper and Jiang (2012) is mostly contributed by shallow to moderate convection and is thus reasonably denoted as precipitative. Interpretation of the 37-GHz cyan and pink ring feature in rapidly intensifying TCs will be further examined in an upcoming study.

3.8 Conclusion

Using 14 years of TRMM Precipitation Radar (PR) reflectivity data, shear-relative distributions of four types of precipitation–convection in different intensity categories of tropical cyclones (TCs) have been statistically quantified and compared in this study. With an emphasis on rapidly intensifying (RI) TCs, we analyzed 1139 TRMM PR overpasses of tropical storms through category 2 hurricanes with at least moderately favorable environmental conditions.

Generally, shallow precipitation (defined as 20-dBZ radar echo top height, 6 km) is more widespread in RI than non-RI storms. A significant difference is observed between RI initial and slowly intensifying storms, as the RI initial category has a much higher frequency of shallow precipitation in all radial distances and shear-relative quadrants (Table 3.4; Figs. 3.2 and 3.6). This indicates that increased shallow precipitation

surrounding the storm center is a first sign of RI and could be used as a predictor of the onset of RI.

Among the four types of precipitation defined in this study, moderate precipitation (20-dBZ radar echo top between 6 and 10km) has the highest percent occurrence in TCs (about 27% overall; Table 3.4), followed by shallow precipitation (about 22% overall), moderately deep precipitation (about 3% overall), and very deep precipitation (about 0.7% overall). Additionally, moderate precipitation contributes over 60% to both total volumetric rain and total latent heating, while the other three kinds of precipitation together account for less than 40% (Table 3.7).

The onset of RI also features more widespread moderate precipitation in all shear-relative quadrants than slowly intensifying, neutral, and weakening storms (Fig. 3.5; Table 3.4). Once the RI begins, the moderate precipitation frequency and its contributions to total volumetric rain and total latent heating continue to increase significantly and peak for RI continuing storms (Fig. 3.5f; Table 3.7). The azimuthally averaged percent occurrence of moderately deep precipitation (20-dBZ radar echo between 10 and 14 km) is very similar in magnitude for storms at the onset of RI and those that are slowing intensifying (Fig. 3.2b), while storms during RI have a much higher occurrence of moderately deep precipitation. The contribution to total volumetric rain from moderately deep precipitation also increases and becomes more symmetric around the center as RI continues.

Very deep convection (20-dBZ radar echo height $\geq$ 14 km) is quite rare in TCs and

is more widespread in non-RI than RI storms (Fig. 3.3; Table 3.4). The maximum frequencies of both moderately deep and very deep convection are located closer to the storm center in RI storms than in non-RI storms. Although very deep precipitation accounts for a disproportion- ate amount of total volumetric rain and total latent heat within the inner core, its absolute percent contribution decreases in order from slowly intensifying, neutral, weakening, RI initial, to RI continuing storms (Table 3.7).

It is found that the contribution to total volumetric rain and total latent heating from the shallow to moderate precipitation in the inner core is greater in RI initial and continuing storms than non-RI storms, while the opposite is true for moderately to very deep precipitation (Table 3.7). This implies that the shallow to moderate precipitation is more important in initiating and maintaining RI. This is consistent with ZJ14 and other satellite-based statistical studies (e.g., Jiang 2012; Jiang and Ramirez 2013) showing that it is not the deep convection but the widespread and symmetric rainfall that is more important to RI.

However, this is inconsistent with previous observational case studies (e.g., Reasor et al. 2009; Guimond et al. 2010; Molinari and Vollaro 2010; Nguyen and Molinari 2012; Reasor and Eastin 2012; Stevenson et al. 2014; Rogers et al. 2015; Susca-Lopata et al. 2015), which emphasized the role of asymmetric very deep convection in RI. As mentioned in section 3.7, most of these observational case studies are biased toward the ending period of RI, while the three studies about Hurricane Earl (2010) focused on deep convection before RI while the storm was in the slowly intensifying stage. Here we argue that RI is more likely triggered by the increase of shallow to moderate precipitation and the

appearance of more moderately to very deep convection in the middle of RI is more likely a response or positive feedback to changes in the vortex that occur earlier in the slowly intensifying period to the beginning of the RI period. The specific mechanism of how shallow to moderate precipitation initiates RI is unknown, but a hypothesized conceptual model is given in Fig. 3.14. It is proposed that the increased shallow to moderate precipitation at the onset of RI might be linked with the moistening, vortex alignment, axisymmetrization, and more latent heat release. Further studies are needed in this direction.

Another interesting finding of this study is that although the downshear-left quadrant is favored for all types of precipitation for weakening, neutral, and slowly intensifying storms, consistent with previous studies for TCs in general (e.g., Corbosiero and Molinari 2002, 2003; Chen et al. 2006; Cecil 2007; Hence and Houze 2012), the shear-relative distributions for RI storms are very different. A cyclonic rotation of peaks from shallow (downshear right) to moderate (downshear left) to moderately and very deep precipitation (upshear left) follows the tangential wind direction around the TC center and may be an indicator of the vortex rapidly strengthening.

A ring of almost 90% occurrence of total precipitation is found for storms in the middle of RI (Fig. 3.14f). After selecting the RI cases with a 37-GHz cyan and pink ring seen in the PR swath, Figure 3.18 indicates that a total precipitation ring is closely analogous to the cyan and pink ring in the 37-GHz color product defined by Kieper and Jiang (2012) that is a very good predictor for RI. The ring is mostly contributed by shallow to moderate precipitation and is thus reasonably denoted as precipitative. The ring indicates

a very high degree of symmetry of shallow to moderate precipitation. Shallow precipitation alone contributes about 40%–50% of the ring (Fig. 3.18b). A ring of only 20%–30% occurrence of 85-GHz PCT $\leq$ 250 K is found for RI cases, indicating that the 85-GHz convective ring claimed by Harnos and Nesbitt (2011) is not a good predictor of RI (Table 3.2; Fig. 3.18d). Jiang and Ramirez (2013) found that the total volumetric rain and total raining area in the inner-core region is much higher in RI storms than non-RI storms. They concluded that high total raining area and total volumetric rain in the inner core are necessary conditions of RI. However, by further separating RI into RI initial and continuing categories, this study finds that higher volumetric rain in the inner core appears only during RI but not at the onset of RI, suggesting that it is a symptom rather than an indicator of the onset of RI.

4. THE EVOLUTION OF RAINFALL AND CONVECTION IN RAPIDLY INTENSIFYING TROPICAL CYCLONES USING 16 YEARS OF TRMM DATA

4.1 Abstract

Using 16-year Tropical Rainfall Measuring Mission (TRMM) Microwave Imager (TMI) observations, rainfall and convection distributions in tropical cyclones (TCs) are examined with respect to the evolution of rapid intensification (RI) events. The onset of RI follows a significant increase in the areal coverage of rainfall (rain rate > 0.5 and 1 mm/hr), cyan of 37 GHz color composites, and shallow precipitation (85 GHz polarization corrected brightness temperature (PCT85) between 260 and 275 K) upshear-left, which in turn could be used as potential parameters to predict RI. Storms during RI (from RI onset to 24 hours before RI ends) are featured with increased rainfall and moderate precipitation (200 K < PCT85 ≤ 260 K). This increase concentrates in the upshear semicircle, especially upshear-right, in the early stage of RI and rotates cyclonically, concentrating to the right of shear in the middle of RI. Very deep convection (PCT85 ≤ 160 K) is most frequent upshear-left 12-24 hours before RI onset but rapidly decreases in the following 24 hours. The RI ending (a 24-h period before RI ends) begins with a significant decrease in total rainfall and cyan coverage. The magnitude of vortex vertical misalignment is quantified by applying the Automated Rotational Center Hurricane Eye Retrieval (ARCHER) product to TMI 85 and 37 GHz observations. The tilt of vortex is large before and near RI onset but decreases quickly in the middle of RI, indicating that vertical alignment is a result rather than a trigger of RI.

4.2 Introduction

Forecasting the intensity change, especially rapid intensification (RI), of tropical cyclones (TCs) is challenging (Marks and Shay 1998) but is also of great importance, considering the associated catastrophic impacts on society. It is now well known that RI most commonly occurs under favorable environmental conditions (Kaplan and DeMaria 2003; Wang and Wu 2004), including warm sea surface temperatures (SSTs) and a deep warm oceanic mixed layer, low vertical wind shear, high lower-tropospheric relative humidity, conditional instability, etc. In the meantime, it is generally accepted that considerations of environmental conditions alone are not sufficient for an accurate forecast of RI (Hendricks et al. 2010). Processes operating on scales smaller than environmental scale, such as vortex and convective scale processes are also part of the mechanisms that govern the RI of TCs.

Rainfall and convection within the inner core region of TCs have been linked with RI in several satellite-based observational studies (e.g., Jiang 2012, Jiang and Ramirez 2013). Jiang (2012) investigated the inner-core convective intensity of TCs in different intensity change categories, classified by the change of maximum sustained winds in future 24 hours. Four convective parameters derived from the Tropical Rainfall Measuring Mission (TRMM) satellite were used as proxies for the strength of inner-core convection and statistically significant differences were found between RI and non-RI storms. This study suggested a potential of improving RI forecast based on the inner-core convective intensity of TCs. It also indicated that the occurrence of hot towers, defined as precipitating systems with 20-dBZ radar echo heights exceeding 14.5 km, were neither necessary nor sufficient for RI. Using TRMM Precipitation Radar (PR), Zagrodnik and Jiang (2014)

studied the shear-relative composite distributions of rainfall, convection and latent heating in TCs that undergo RI. They noted that future 24-h intensity change was most strongly correlated with the areal coverage of rainfall, defined as the percent occurrence of PR near-surface reflectivity > 20 dBZ. Using the same dataset, Tao and Jiang (2015, hereafter TJ15) analyzed the distributions of four types of precipitation-convection in TCs and quantified their contribution to total volumetric rain and total latent heating. It was shown that statistically, RI followed increased and widespread shallow precipitation (defined as 20 dBZ radar echo height < 6 km) around the TC center, which in turn could be used as an indicator of RI.

Composites and statistical analysis of previous satellite-based studies are very useful in distinguishing the inner-core rainfall and convection distributions of RI storms from those in other intensity change categories. But there are some limitations as well, given that RI typically occurs as an event (Kieper and Jiang, 2012). Examining RI only in terms of future 24-h intensity change cannot fully address the role of convection in RI, because of the absence of temporal information before the RI onset, at the beginning of RI, during the middle of RI, and within the ending period of RI. Kieper and Jiang (2012) analyzed the 37 GHz color composite images (Lee et al., 2002) of 28 RI events during the 2003-2007 Atlantic hurricane seasons. These RI events lasted for at least 24 hours and could be as long as 48-60 hours. They indicated that a well-defined ring pattern around the center, identified from 37 GHz color images, combined with the Statistical Hurricane Prediction Scheme (SHIPS) RI index (RII) was very skillful for RI prediction. This ring pattern, named cyan+pink color ring, was at least 90% closed around the storm center and filled with either cyan color (warm rain or low-level water clouds) or pink color (precipitation

with ice aloft). However, further analyses using statistical tools are needed since the cyan+pink color ring is only defined subjectively.

The convective evolution in RI storms is examined extensively in recent case studies (e.g., Stevenson et al. 2014, Susca-Lopata et al. 2015). Stevenson et al. (2014) studied the evolution of lightning burst during the RI period of Hurricane Earl (2010), based on the World Wide lightning Location Network (WWLLN) and aircraft data. They found an increase of lightning outbreak within the inner core region six hours prior to the RI onset. The increased lightning occurrence concentrated in the upshear-left quadrant, different from the typical inner-core lightning distribution (Corbosiero and Molinari 2003), and located inside the radius of maximum wind (RMW). They further hypothesized that the RI of Hurricane Earl (2010) was a result of the reduced upshear tilt by vertical wind shear and the enhanced warm core by lightning within the RMW. The RI period of Hurricane Earl (2010) was also examined by Rogers et al. (2015), using observations from multiple aircraft missions. Alternatively, their study focused on the role of convective bursts (i.e., intense and vigorous convection). It was indicated that the onset of RI followed the process of vortex vertical alignment, which was closely associated with the occurrence of convective bursts around the center. All the mechanisms that proposed triggering the onset of RI by case studies need to be statistically quantified based on a larger dataset.

This study examines the evolution of rainfall and convection in the inner core region of TCs based on the concept of RI events. Observations from the TRMM Microwave Imager (TMI) are classified into several categories by their time relative to the RI onset. By investigating and comparing the rainfall and convection distributions before RI, during RI, and in the ending period of RI, the properties of rainfall, the role of convection, and the

magnitude of vortex vertical alignment in different stages of RI and their relationship with the RI onset are analyzed statistically. Section 4.3 describes the data and methods applied in this study. The time evolution and shear-relative composites of rainfall and convection during the RI periods are discussed in section 4.4. Section 4.5 analyzes the magnitude of vortex vertical misalignment and the direction of tilt relative to vertical wind shear. The discussion and conclusion are presented in section 4.6.

4.3 Data and Methodology

4.3.1 RI event-based dataset

The best track data from the National Hurricane Center (NHC) and Joint Typhoon Warning Center (JTWC) are used to determine RI events from a total of 1518 TCs between 1998 and 2013. An RI event is defined as multiple, continuous, and overlapping 24-h periods where the maximum sustained winds of each period increased by at least 30 kt, as illustrated in Figure 4.1. Here, each 24-h period within an RI event refers to one RI case in Kaplan and DeMaria (2003). Figure 4.2 displays the best track of defined RI events in seven TC oceanic basins, including north Atlantic (ATL), east Pacific (EPA), central Pacific (CPA), northwest Pacific (NWP), north Indian Ocean (NIO), south Indian Ocean (SIO), and south Pacific (SPA). The corresponding statistics are summarized in Table 4.1. TCs are most active in NWP basin, which contains the largest population of both TCs and those undergoing RI. Interestingly, by this definition, RI is more frequent for TCs in the Southern Hemisphere. A storm could have more than one RI event during its lifetime, as shown in Table 4.1. The mean time period for an RI event is approximately 38 hours.

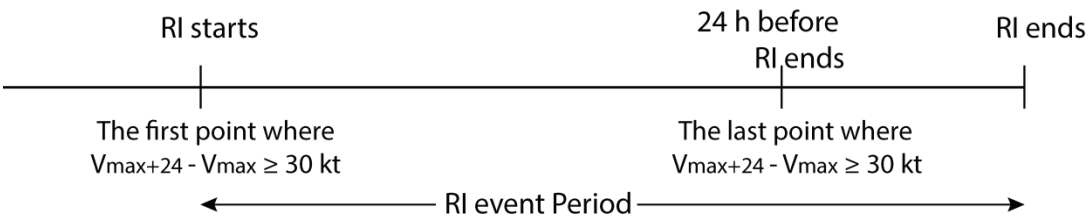

Figure 4.1: Definition of an RI event using the best track data. Here, V_{max} and V_{max+24} represent the maximum sustained wind at the current synoptic time and 24 hours in future, respectively.

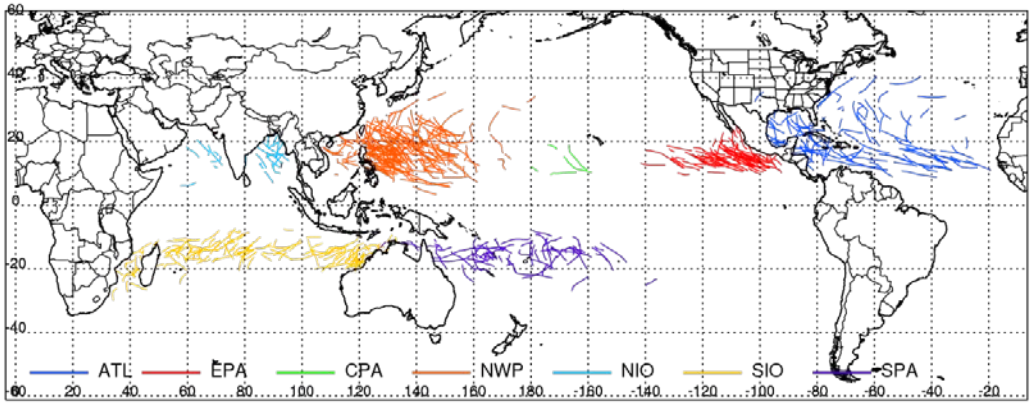

Figure 4.2: Global TC RI event best track in seven oceanic basins during 1998-2013.

Table 4.1: Number of TCs and TCs that undergo RI, percentage of TCs that undergo RI, number of RI event, and mean RI event period in different TC basins.

	ATL	EPA	CPA	NWP	NIO	SIO	SPA	All
# of TCs	278	263	23	456	85	268	145	1518
# of TCs that undergo RI	90	85	3	179	21	113	61	552
% of TCs that undergo RI	32.4	32.3	13.0	39.3	24.7	42.2	42.1	36.4
# of RI event	113	96	5	239	23	145	79	700
Mean RI event period [hr]	35.3	37.8	42.0	39.2	42.0	37.1	37.7	37.9

4.3.2 Selection of TRMM overpasses

The dataset for this study is derived from the TRMM Tropical Cyclone Precipitation Feature (TCPF) database (Jiang et al. 2011), which includes the overpasses of all global

TCs viewed by the TRMM satellite. Similar to Zagrodnik and Jiang (2014), the storm center interpolated with global best track information is manually adjusted for TCs between 1998 and 2013 to better align with the imageries of PR and TMI 37 GHz channel. Besides the TRMM database, two additional datasets are applied to characterize the large-scale environmental conditions of each case. The sea surface temperature (SST) is obtained from the Reynolds daily SST grid point (at a spatial grid resolution of 0.25^{o}) nearest to the storm center (Reynolds et al. 2007). The total precipitable water (TPW) and wind field data are derived from the 0.75^{o}-resolution European Centre for Medium-Range Weather Forecasts (ECMWF) interim reanalysis dataset (Simmons et al. 2007). The TPW of each case refers to the average of the innermost 250 km around the TC center. The vertical wind shear is the difference between the averaged wind vectors at the 200- and 850-hPa. The wind vectors are averaged within a ring of 500-750 km from the TC center to eliminate the influence of the storm's circulation as much as possible, following Hence and Houze (2011).

Since the focus of this study is the inner core rainfall and convection during the RI periods of TCs, several criteria have been applied to the selection of overpasses viewed by the TRMM TMI. Firstly, the interpolated storm center must be over water at the current observational time and 24 hours in the future, as the intensity change of TCs over land is governed by different mechanisms. Secondly, TMI overpasses must capture the innermost 200 km area in order to be included in the study, i.e., the inner-core region of a innermost 200 km area in order to be included in the study, i.e., the inner-core region of a storm is fully covered by each selected overpass. Thirdly, storms that are tropical depressions (maximum sustained wind less than 34 kt) and major hurricanes (maximum sustained wind

greater than 95 kt) are excluded, following Zagrodnik and Jiang (2014). Generally, tropical depressions rarely rapidly intensify and the intensity changes of major hurricanes are most commonly associated with eyewall replacement cycles (Willoughby et al. 1982), which is beyond the topic of this study. Based on the TRMM observational time and the start/end time of RI events, the selected TMI overpasses are classified into 14 categories, listed in Table 4.2.

Table 4.2: Number of selected TRMM TMI overpasses in different TC basins before RI, during RI and in the RI ending period.

Category		Number of overpasses [#]											
		Oceanic Basins							All	Intensity change			
		ATL	EPA	CPA	NWP	NIO	SIO	SPA		RI	SI	N	W
Before RI	36~48 h before	3	3	1	8	1	8	2	26	0	14	10	2
	24~36 h before	6	1	1	17	0	8	6	39	0	25	14	0
	18~24 h before	4	4	0	7	2	11	4	32	0	21	11	0
	12~18 h before	11	3	0	18	1	10	4	47	0	37	10	0
	6~12 h before	3	5	0	23	0	8	5	44	0	42	2	0
	0~6 h before	3	4	0	19	1	7	2	36	0	36	0	0
During RI	0~6 h after	8	3	0	19	0	8	3	41	41	0	0	0
	6~12 h after	7	2	0	16	1	15	4	45	45	0	0	0
	12~18 h after	9	5	0	19	0	9	3	45	45	0	0	0
	18~54 h after	4	9	1	26	2	12	7	61	61	0	0	0
RI ending	18~24 h before	6	8	1	15	2	9	3	44	0	43	1	0
	12~18 h before	5	10	0	20	1	15	4	55	0	52	2	1
	6~12 h before	7	3	1	14	0	11	8	44	0	23	18	3
	0~6 h before	3	7	0	15	0	11	0	36	0	13	18	5
All		79	67	5	236	11	142	55	595	192	306	86	11

The effects of the environmental conditions also have to be considered before completing the final dataset. Figure 4.3 shows the evolution of SST, vertical shear magnitude, TPW, and storm motion for all TRMM TMI overpasses that meet the above-mentioned requirements. As it can be seen, it is extremely difficult to pinpoint the time of RI onset depending on environmental parameters alone (Hendricks et al. 2010). But RI

generally does not occur in an unfavorable environment (Kaplan and DeMaria 2003; Wang and Wu 2004). Based on the extreme values of the selected environmental parameters during RI (i.e., from the RI onset to 24 hours before RI ends), four cutoff criteria have been determined to at most remove the impacts of environmental conditions on RI: SST $\geq$ 25.8 ^{o}C, shear $\leq$ 14.1 m/s, TPW $\geq$ 48.7 mm, storm $\leq$ 10.8 m/s.

It should be noted that the selected cases in this study are only classified depending on the time period relative to RI events, regardless of the future 24-h intensity change. Therefore, overpasses of storms that contain more than one RI event during their lifetime could fall into multiple categories, resulting in RI cases (defined as future 24-h intensity change $\geq$ 30 kt) included in categories of before RI (i.e., period before the onset of RI) or RI ending (i.e., period within 24 hours before RI ends). For this reason, the future 24-h intensity change is also considered to remove the ambiguity. The final sample size for each RI event-based category over global TC basins is shown in Table 4.2, with RI cases only counted in during RI category. Also displayed in Table 4.2 is the number of selected TMI overpasses in different future 24-h intensity change categories, including RI, slowly intensifying (SI), neutral (N), and weakening (W). The definition of each intensity change category follows TJ15. The dataset of this study mainly consists of overpasses associated with SI (51.4%) and RI (32.3%) storms.

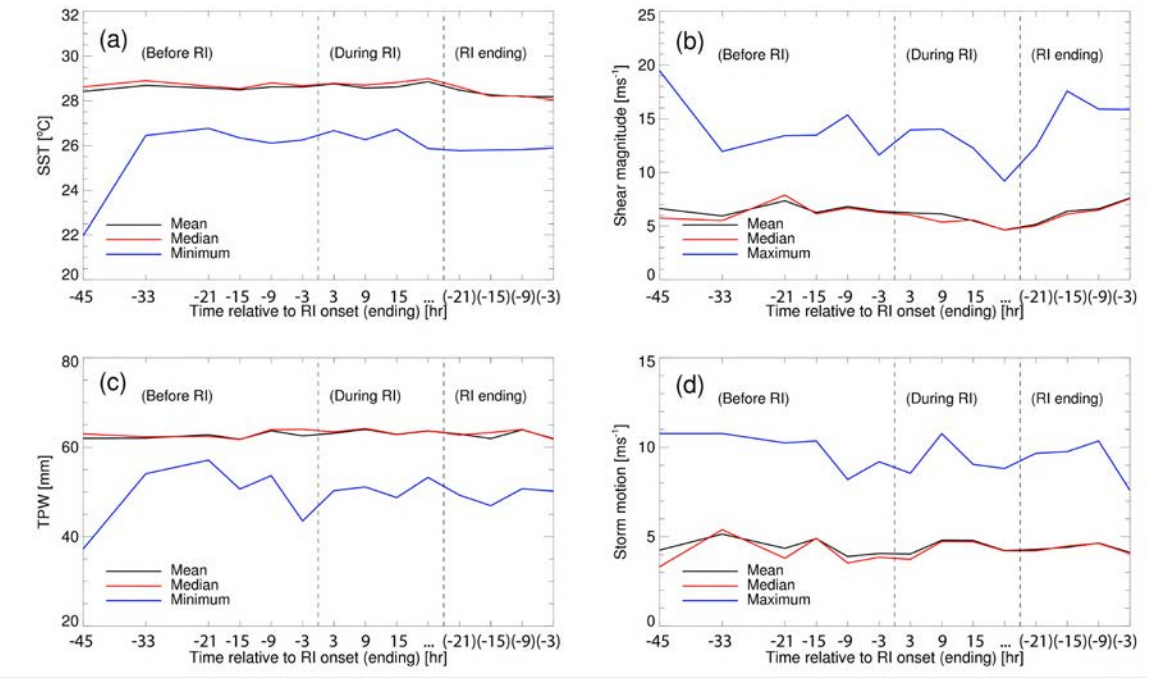

Figure 4.3: Evolution of mean, median, and maximum/minimum values of environmental conditions: (a) SST, (b) shear magnitude, (c) TPW, and (d) storm motion over time. Time is defined the same way as in Fig. 4.1.

4.3.3 Selection of variables

To examine the rainfall and convection distributions during the RI periods, three variables are selected, including rain rate, 85 GHz and 37 GHz brightness temperature. Rain rate derived from the version 7 of the TMI 2A12 algorithm is applied, with a resolution of 8 × 6 km (7 × 5 km before boost in 2001). Different from version 6, a parameter named probability of precipitation is added in version 7 for pixels over ocean with a nonzero raining rate. Here, a 90% probability of rain threshold is used, i.e., rain rate with a probability of precipitation lower than 90% is regarded as zero. The microwave brightness temperatures at 85 and 37 GHz channels decrease markedly by the existence of

frozen hydrometers. To distinguish the ambiguity between low brightness temperatures due to ice scattering and those due to low surface emissivity, a polarized corrected brightness temperature (PCT) for 85 GHz (Spencer et al. 1989) and 37 GHz (Cecil et al. 2002) is derived respectively. Generally, low PCTs represent deeper and more vigorous convection in the storm. But it should be noted that emission by liquid water also contributes to higher PCTs at these channels, especially at 37 GHz.

In this study, four types of precipitation-convection are defined based on the 85 GHz PCT (PCT_{85}). These include very deep convection ($PCT_{85} \leq 160$ K), moderately deep convection (160 K < $PCT_{85} \leq 200$ K), moderate precipitation (200 K < $PCT_{85} \leq 260$ K), and shallow precipitation (260 K < $PCT_{85} \leq 275$ K). The original idea of classifying shallow to very deep precipitation-convection in TCs comes from TJ15. The difference is that their study used the height of 20 dBZ radar echo observed by TRMM PR while this study uses 85 GHz PCT from TRMM TMI. Using the same dataset as TJ15, the 20 dBZ radar echo height and the corresponding 85 GHz PCT are obtained for all PR pixels within the inner core region. The cutoff criteria for 85 GHz PCT of each type of precipitation-convection defined in this study are derived from the cumulative distribution function (CDF) shown in Figure 4.4. For all identified TRMM TMI pixels in the innermost 250 km of the storm center, the scatterplot of their real colors in the 37 GHz color composite products (Lee et al. 2002) as a function of vertically (V_{37}) and horizontally polarized (H_{37}) brightness temperatures is displayed in Figure 4.5. According to their appearances on the 37 GHz color composite product, three regions are identified, including pink ($PCT_{37} < 270$ K), dark cyan ($PCT_{37} \geq 270$ K & $H_{37} \geq 225$ K & $V_{37} \leq 265$ K), and bright cyan ($PCT_{37} \geq 270$ K & $H_{37} \geq 225$ K & $V_{37} > 265$ K).

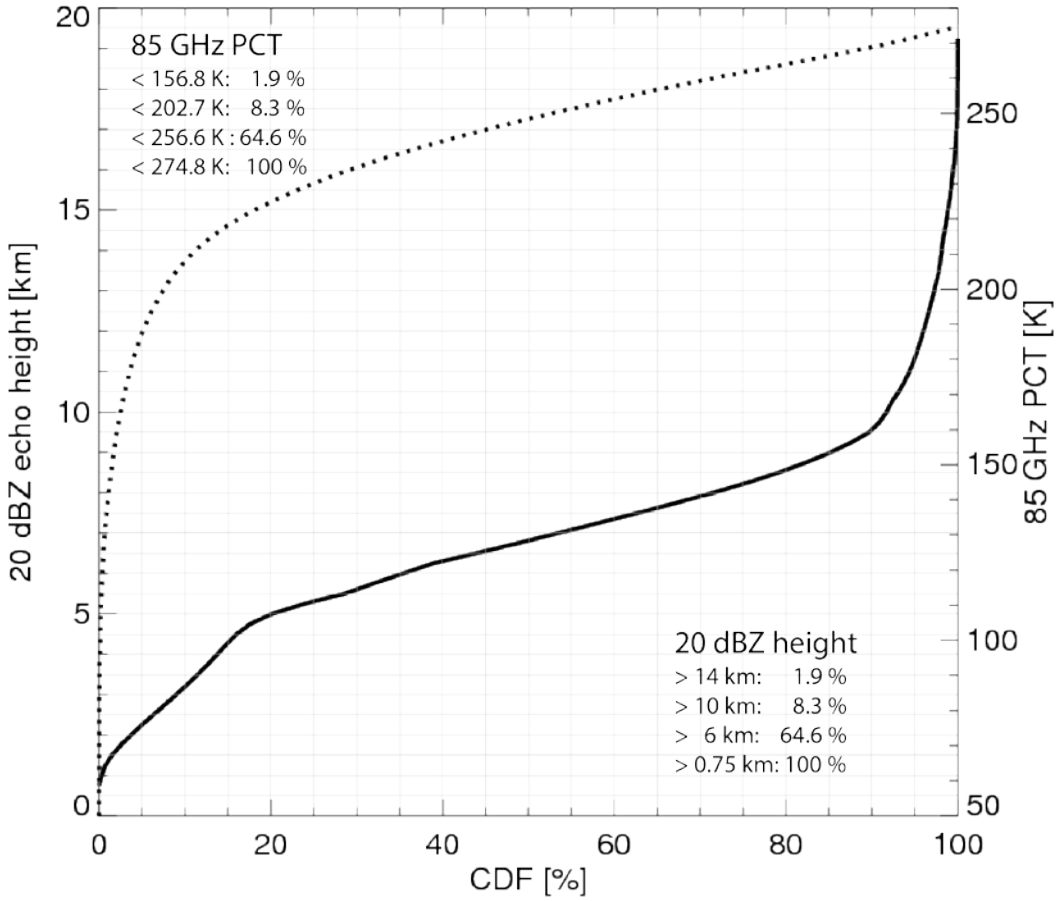

Figure 4.4: Cumulative distribution functions (CDFs) of 20 dBZ echo height (solid line) and 85 GHz PCT (dashed line) for pixels within the inner core region. Numbers in the upper left and lower right indicate the percentage of pixels meeting various criteria.

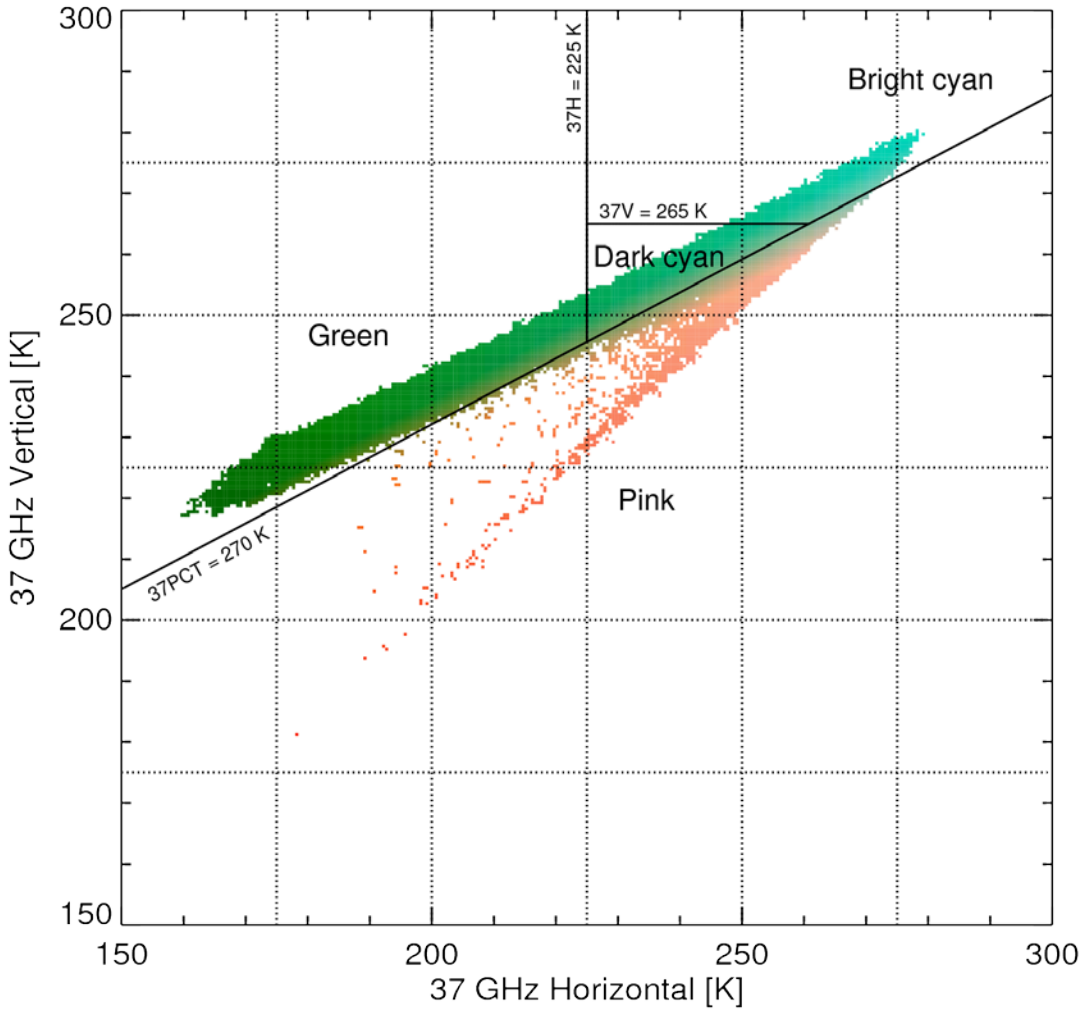

Figure 4.5: Scatterplot of real colors in the NRL 37 GHz color product as a function of 37H and 37V for all TMI pixels in the innermost 250 km of the storm center. Pink, dark cyan, and bright cyan are separated by solid black lines.

4.4 Evolution of rainfall and convection distribution

4.4.1 Time evolution

1) Rain rate

This part of study uses the Hovmöller diagrams to plot the time evolution of azimuthally averaged rainfall and convection during the RI periods of TCs. The Hovmöller diagrams are generated by grouping the TMI pixels from the 14 RI event-based categories (Table 4.2) into bins representing 10-km annuli (15-km annuli for pixels at 37 GHz) extending radially outward from the storm center.

Figure 4.6 displays the Hovmöller diagram of the percent occurrence of rain rate > 0.5, 1, 5, and 10 mm/hr. Here, the percent occurrence refers to the fraction of pixels with different levels of rain rate divided by the total number of pixels. In the inner core region of TCs (r < 100 km), both the percentages of pixels with rain rate > 0.5 (Fig. 4.6a) and 1 mm/hr (Fig. 4.6b) increase significantly around 3-9 hours before the onset of RI and continue to increase after RI begins. In the middle of RI events (> 9 hours after RI onset), more than 90% and 80% of the area between 30-70 km is covered by raining pixels with rain rate > 0.5 and 1 mm/hr, respectively. During the period before the RI onset, the percent occurrence of rain rate > 5 (Fig. 4.6c) and 10 mm/hr (Fig. 4.6d) steadily increase with time approaching RI onset while rapidly increase around 3-9 hours after the RI onset. Both of these percentages continue to increase as RI goes on and reach the maximum values around 50 km of the storm center just prior to 24 hours before RI ends.

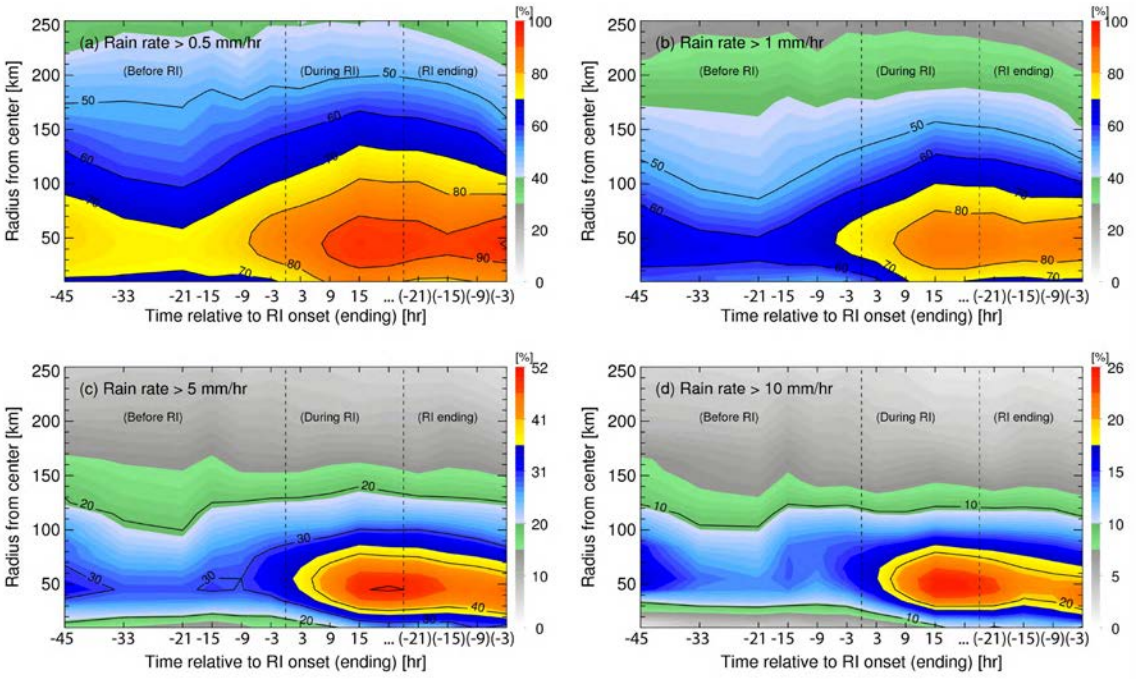

Figure 4.6: Hovmöller diagrams of azimuthally averaged percent occurrence of rain rate (a) > 0.5 mm/hr, (b) > 1 mm/hr, (c) > 5 mm/hr, and (d) > 10 mm/hr. The averages are shown from the storm center out to 250 km. Dashed lines from left to right represent the RI onset and 24 hours before RI ends.

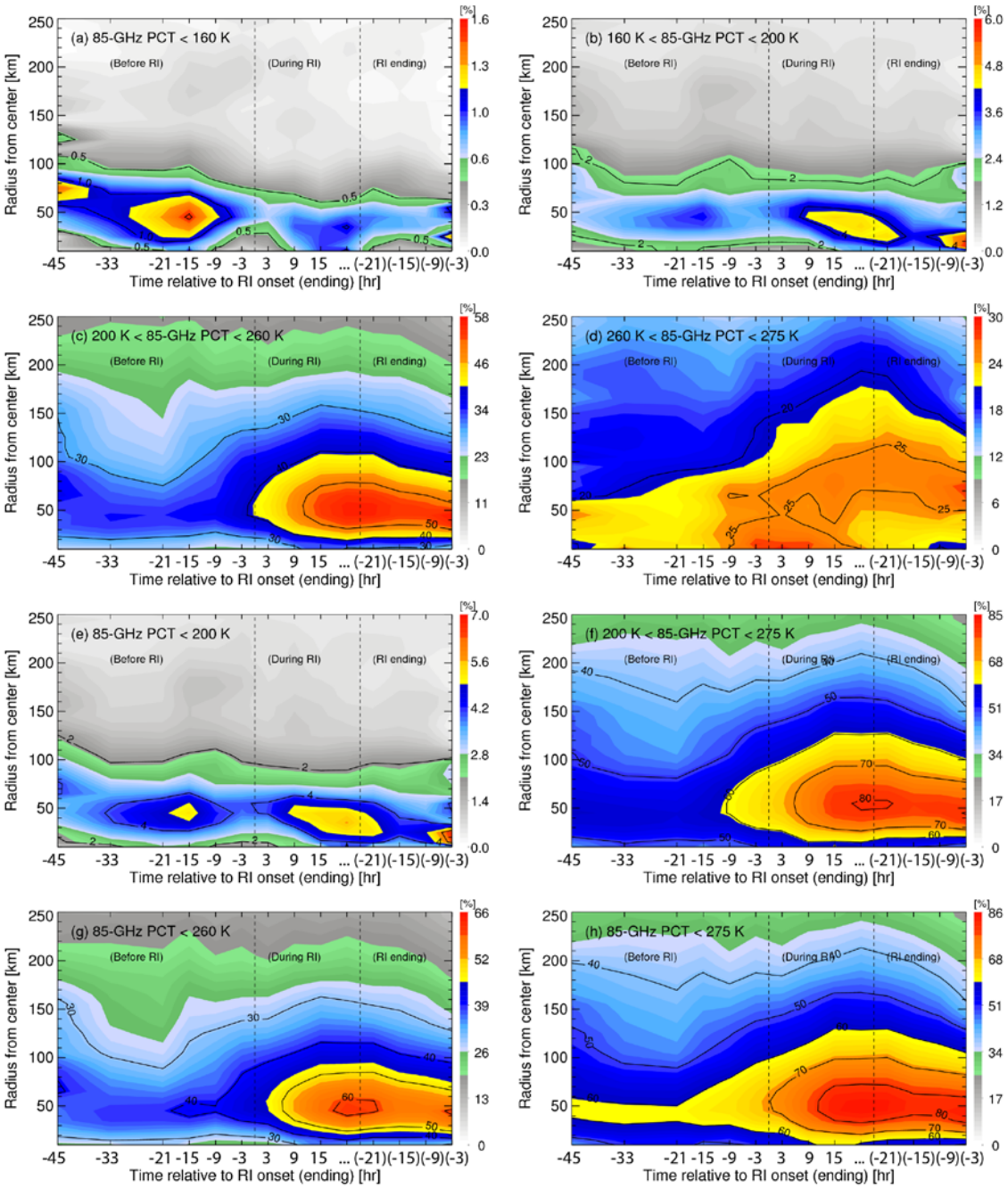

Figure 4.7: As in Fig. 4.6, but for percent occurrence of 85 GHz PCT (a) < 160 K, (b) 160-200 K, (c) 200-260 K, (d) 260-275 K, (e) < 200 K, (f) 200-275 K, (g) < 260 K, and (h) < 275 K.

2) 85 GHz brightness temperature

The Hovmöller diagram of the percent occurrence of shallow to very deep precipitation-convection defined by the 85 GHz PCT are shown in Figure 4.7. Overall, pixels with 85 GHz PCT less than 160 K are quite rare in TCs. The maximum azimuthal-mean of the percent occurrence of very deep convection is at about 1.5% (Fig. 4.7a). The occurrence of very deep convection peaks about 15 hours before the RI onset at around 50 km from the storm center, and rapidly decreases in the following 24 hours. Generally, the areal coverage of very deep convection does not reach 1% during the RI periods of TCs until in the end of the RI ending period. This is consistent with TJ15, which indicated that very deep convection (defined as 20-dBZ echo height $\geq$ 14 km) was more widespread in SI than RI storms. Different from very deep convection, two peaks are found in the Hovmöller diagram of the percent occurrence of moderately deep convection (Fig. 4.7b). The first peak is observed at around six hours before RI ends, with a percentage of about 6% between 10-30 km from the storm center. The second one is at around 15 hours after the onset of RI. The percent occurrence of moderately deep convection steadily increases before the RI onset, with a slight decreasing period between 3-9 hours prior to the RI onset.

Moderate precipitation is most commonly observed in TCs compared with other types of precipitation-convection defined in this study. The percentage of pixels with 85 GHz PCT between 200 and 260 K increases significantly when storms begin to RI and this increase continues at a higher rate as RI goes on (Fig. 4.7c). The percent occurrence of moderate precipitation has increased by 10% within 10 hours from the RI onset. From the middle of RI events to the end of the RI ending period, about 55% of the area between 30-60 km of the storm center is covered with moderate precipitation. Shallow precipitation is

most frequent in a 12-h period from three hours before the onset of RI to nine hours after. The percent occurrence of shallow precipitation peaks at about 30% near the storm center, and decreases just prior to the beginning of the RI ending period (Fig. 4.7d).

The Hovmöller diagram of the azimuthally averaged percent occurrence of 85 GHz PCT < 200 K (i.e., moderately deep to very deep convection) is illustrated in Figure 4.7e. The overall pattern is similar to that of moderately deep convection (Fig. 4.7b) except for a third peak at around 15 hours before the onset of RI, which is mostly contributed by the increased very deep convection. The percent occurrence of shallow to moderate precipitation, shown in Figure 4.7f, increases significantly at around nine hours before the RI onset and continues to increase for storms undergoing RI. A maximum value (~80%) at about 50 km of the storm center is observed near 24 hours before RI ends. Figure 4.7g and 4.7h depict the percent occurrence of 85 GHz PCT < 260 K (i.e., all precipitation but shallow) and < 275 K (i.e., all precipitation), respectively, which are both closely analogous to that of shallow to moderate precipitation (Fig. 4.7f). Without considering shallow precipitation, the areal coverage of rainfall decreases from 70% (Fig. 4.7h) to 40-45% (Fig. 4.7g) near the onset of RI.

3) 37 GHz brightness temperature

The percent occurrence of pink region in 37 GHz color composites increases significantly at about nine hours after the RI onset and the maximum (~38%) is observed 24 hours before RI ends at around 55 km of the storm center (Fig. 4.8a). During the period before the onset of RI, the percentage of bright cyan first decreases and then increases at about nine hours prior to the RI onset (Fig. 4.8b). The increase continues as RI goes on, with a maximum of ~30% between 45-60 km of the storm center at around 15 hours after

the RI onset. A 12-h decrease is observed at the beginning of the RI ending period, followed by an increase several hours before RI ends. Generally, at least 30% of the innermost 50 km area is covered by dark cyan (Fig. 4.8c) during the whole period of analysis (i.e., from 48 hours before RI onset to the end of RI events) and the maximum percent occurrence (~35%) is observed between 3-15 hours after the RI onset. Considering both dark and bright cyan regions, shown in Figure. 4.8d, a significant increase is observed at around six hours before the onset of RI. The percent occurrence of cyan (both dark and bright cyan) continues to increase as RI goes on and peaks at ~60% around 12 hours after the onset of RI. Figures 4.8e and 4.8f show the Hovmöller diagram of the percent occurrence of pink and bright cyan, and pink and cyan, respectively. Both distributions show significant increase several hours prior to the onset of RI and around six hours after RI begins. Overall, results of Figures 4.6-4.8 indicate that the onset of RI follows increased areal coverage of rainfall with light-to-moderate raining rate and shallow precipitation around the storm center, consistent with TJ15.

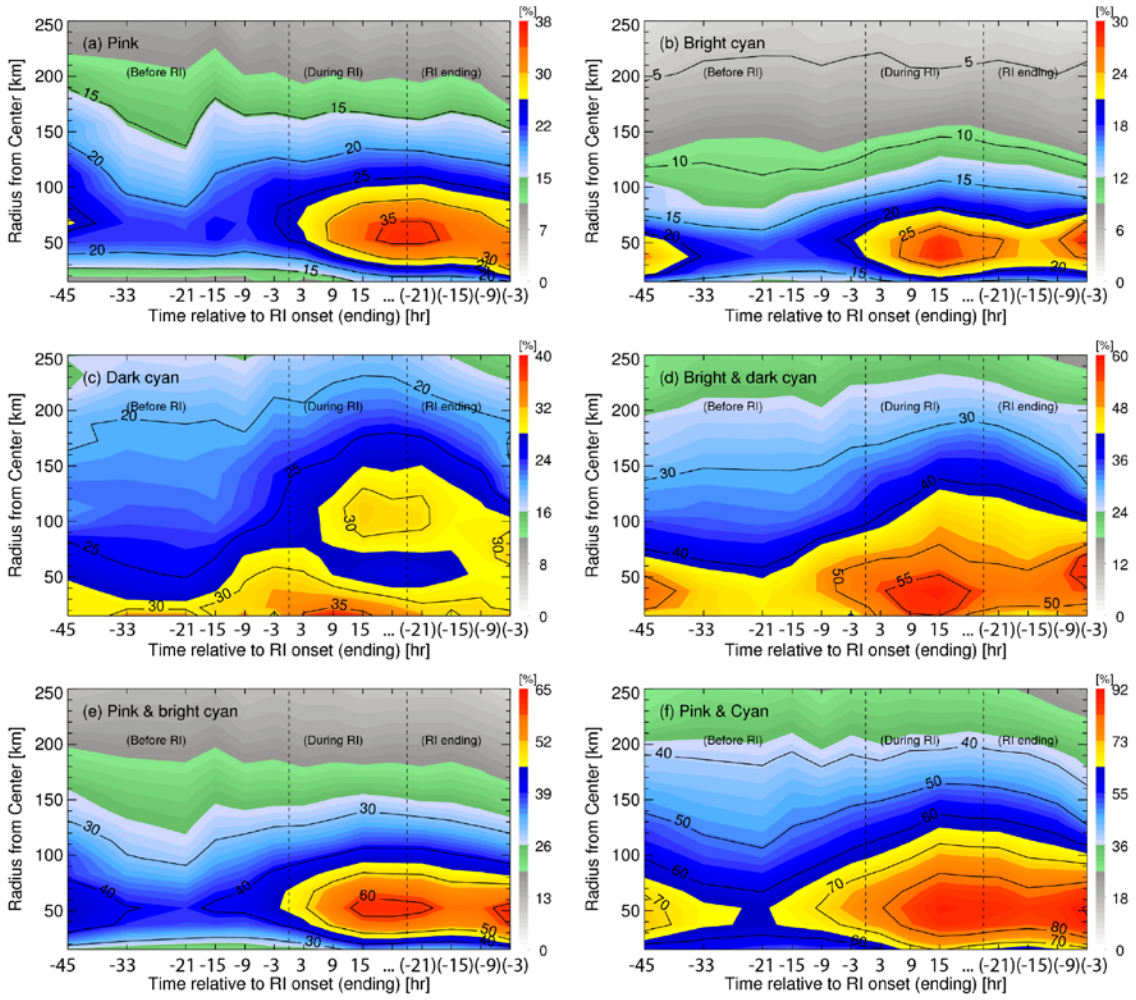

Figure 4.8: As in Fig. 4.6, but for percent occurrence of (a) pink, (b) bright cyan, (c) dark cyan, (d) cyan, (e) pink and bright cyan, and (f) pink and cyan in 37 GHz color composite images.

Table 4.3: Mean values of maximum sustained winds at current observational time (Vmax), SST, vertical wind shear magnitude, TPW, storm motion, and the difference between the direction of vertical wind shear and storm motion vector. Asterisks represent the statistical significance of the value from the value in the previous column at the 95% (*), 99% (**), and 99.9% (***) confidence level.

Category	Before RI			During RI		RI ending	
	24~48 h	12~24 h	0~12 h	RI init.	RI cont.	12~24 h	0~12 h
Vmax [kt]	52.42	52.12	53.99	58.22	64.56**	63.58	71.19**
SST [^{o}C]	28.73	28.52	28.64	28.66	28.76	28.39**	28.17
Shear [m/s]	5.95	6.75	6.47	6.18	5.01*	5.66	6.74*
TPW [mm]	62.48	62.15	63.33	63.58	63.30	62.65	63.02
Motion [m/s]	4.70	4.67	4.04	4.44	4.47	4.31	4.40
Shear–Motion[deg]	-68.85	-34.56	-67.27	-50.37	-74.62	-48.59	-60.21

4.4.2 Significance tests

To further analyze the above-noted differences in the areal coverage of rainfall and convection before and after the RI onset, the environmental conditions associated with each RI event-based category are firstly quantified. The mean values of the maximum sustained winds, SST, shear magnitude, TPW, storm motion, and the discrepancy between the direction of shear and motion vector are shown in Table 4.3. The total number of RI event-based categories considered here reduces from 14 to 7 in order to obtain a large enough sample size for each category. Statistical significance levels derived from the student's t-test are also displayed in Table 4.3. Storms that have been undergoing RI for over 12 hours (i.e., RI continuing) present significantly higher intensity and lower vertical wind shear than those within 12 hours from the RI onset (i.e., RI initial). The SST decreases

significantly 12 hours following the period of RI continuing, while the intensity and vertical wind shear significantly increase from 12-24 to 0-12 hours before RI ends.

The composite-mean values, averaged within 100 km of the storm center, are summarized in Table 4.4. Within 12 hours prior to the onset of RI, the increase of the percent occurrence of several rainfall and convective parameters shown in the Hovmöller diagrams are all statistically significant at the 95% confidence levels or higher. These parameters include rain rate > 0.5 and 1 mm/hr, shallow precipitation, shallow-to-moderate precipitation, all precipitation, and dark cyan, cyan, pink/bright cyan, and pink/cyan regions in 37 GHz color composite product. The percentages of pixels with all selected levels of rain rate continue to increase rapidly during the RI period (both RI initial and RI continuing) until the beginning of the RI ending period. This is also the case for the percent occurrence of moderate precipitation, shallow-to-moderate precipitation, all precipitation but shallow, all precipitation, and pink/cyan regions in 37 GHz color images. The areal coverage of 37 GHz PCT less than 270 K (pink region) only increases significantly in the middle of RI events (i.e., RI continuing stage). The RI ending period begins with a rapid decrease in the percent occurrence of rain rate > 0.5, 1, 5, and 10 mm/hr, all precipitation, and pink/cyan regions in 37 GHz color images.

Table 4.4: Composite-mean values of the percent occurrence of various rain rate, 85-GHz and 37-GHz brightness temperatures, averaged within 100 km of the TC center. Asterisks represent the statistical significance of the value from the value in the previous column at the 95% (*), 99% (**), and 99.9% (***) confidence level.

		Before RI			During RI		RI ending	
		24~48	12~24	0~12	RI init.	RI cont.	12~24	0~12
Rain rate [mm/hr]	Rain rate > 0.5	71.60	66.09	77.32***	84.39**	90.54**	85.25**	86.24
	Rain rate > 1	59.23	54.17	64.10**	73.54**	82.75***	75.65**	76.75
	Rain rate > 5	26.17	25.55	28.61	36.02**	42.54**	37.07*	38.06
	Rain rate > 10	13.32	12.78	13.50	17.57*	21.15*	16.77**	18.75
85-GHz [K]	$PCT_{85} \leq 160$	0.67	1.08	0.59	0.49	0.45	0.61	0.37
	$160 < PCT_{85} \leq 200$	2.14	2.81	2.28	2.69	2.97	2.59	2.41
	$200 < PCT_{85} \leq 260$	32.08	30.28	35.44	41.82*	51.56***	47.50	45.14
	$260 < PCT_{85} \leq 275$	21.24	20.91	24.72**	25.08	25.05	24.61	25.31
	$PCT_{85} \leq 200$	2.81	3.89	2.87	3.19	3.42	3.20	2.78
	$200 < PCT_{85} \leq 275$	53.32	51.19	60.16**	66.89*	76.61***	72.12	70.45
	$PCT_{85} \leq 260$	34.89	34.17	38.31	45.01*	54.98***	50.70	47.92
	$PCT_{85} \leq 275$	56.13	55.08	63.03*	70.08*	80.03***	75.31*	73.23
37-GHz	Pink	18.44	18.76	20.94	23.21	26.75*	24.47	24.09
	Bright cyan	12.74	11.07	13.14	15.90	16.67	13.90*	15.36
	Dark cyan	24.80	22.13	26.28**	27.87	30.18	28.54	27.69
	Cyan	37.54	33.20	39.41**	43.77	46.85	42.44*	43.04
	Pink & bright cyan	31.17	29.83	34.07*	39.11*	43.42	38.38*	39.45
	Pink & cyan	55.97	51.96	60.35**	66.98*	73.60**	66.91**	67.14

4.4.3 Shear-relative composites

1) Rain rate

Shear-relative composite images are applied in this part of study (Figures 4.9-4.12). The composites are generated by orientating the selected TMI overpasses with the shear vector pointing upward along the +y axis and the storm center in the middle. Overpasses of Southern Hemisphere are flipper 180^{o} before composited with those of Northern Hemisphere, following Chen et al. (2006). The TMI pixels, with their new shear-relative

coordinates, are then compiled into 8×8 km^2 (8×16 km^2 for 37 GHz) grid cells. The value of each grid cell represents the percentage of pixels satisfying the criteria of various rain rate, and 85 GHz and 37 GHz brightness temperatures. Shear-relative images are described using a quadrant approach (Chen et al. 2006), with the upper-left, upper-right, lower-left, and lower-right quadrants referring to downshear-left (DL), downshear-right (DR), upshear-left (UL), and upshear-right (UR), respectively. Our focus here is how the inner-core rainfall and convection distributions evolve relative to the direction of vertical wind shear from 12-24 hours prior to the RI onset to 12-24 hours before RI ends.

The composites of the percent occurrence of rain rate at different levels are DL dominated in all RI event-based categories (Fig. 4.9), consistent with previous studies (e.g., Chen et al. 2006; Wingo and Cecil 2010). The significant increase in the percentage of pixels with rain rate > 0.5 mm/hr 0-12 hours prior to the RI onset (Table 4.4) is mostly contributed by pixels in the upshear semicircle. RI initial (Fig. 4.9I.c) and RI continuing (Fig. 4.9I.d) categories are featured with significant increase of the percent occurrence of rain rate > 0.5 mm/hr UR, while a rapid decrease in the same shear-relative quadrant is observed at the beginning of the RI ending period (Fig. 4.9I.e). A ring of at least 90% occurrence of rain rate > 0.5 mm/hr is observed extending completely around the center for RI continuing storms (Fig. 4.9I.d). Similar results are found for that of rain rate > 1 mm/hr (Fig. 4.9II).

Both the percentages of pixels with rain rate > 5 and > 10 mm/hr increase significantly from 0-12 hours before RI onset (Fig. 4.9III.b & Fig. 4.9IV.b) to RI initial stages (Fig. 4.9III.c & Fig. 4.9IV.c) and the increase mostly concentrates in the UL quadrant. Significant increase in the percent occurrence of rain rate > 5 and 10 mm/hr

continues when storms move onto the RI continuing stages (Fig. 4.9III.d & Fig. 4.9IV.d) but the increase during this period is mostly contributed by raining pixels right of the shear. Overall, the rainfall distribution becomes more symmetric around the storm center from 12-24 hours before the onset of RI to RI continuing periods. This is consistent with Alvey III et al. (2015). They examined the precipitation properties of TCs as a function of the intensity changes based on 15 years of passive microwave satellite data, and indicated that the rate of symmetrization in precipitation distribution increased with increasing rate of intensity change.

2) 85 GHz brightness temperature

Very deep convection is most frequent 12-24 hours prior to the RI onset and concentrates in the UL quadrant (Fig. 4.10I.a), peaking at about 4.5% of total pixels. However, a dramatic decrease is observed in the following 12 hours (Fig. 4.10I.b) and it continues to decrease after RI begins. The percent occurrence of very deep convection is less than 1% everywhere within 100 km of the storm center during the RI initial (Fig. 4.10I.c) and RI continuing (Fig. 4.10I.d) categories, and does not increase much until 12-24 hours before RI ends (Fig. 4.10I.e). Different from very deep convection, the maximum percent occurrence of moderately deep convection (around 7%) is observed DL 12-24 hours before RI starts (Fig. 4.10II.a). But similarly, it also decreases significantly 0-12 hours before the RI onset (Fig. 4.10II.b). The areal coverage of moderately deep convection slightly increases in both DL and UL quadrants when storms begin to RI (Fig. 10II.c). Such increase, however, is not considerable until in the middle of RI events. A composite maximum percent occurrence of moderately deep convection (about 10%) is observed in the DL quadrant for storms that have been undergoing RI for at least 12 hours (Fig. 10II.d).

The bottom panel of Figure 10 shows the composite shear-relative distribution of deep convection (both moderately deep and very deep convection), generated by simply combining the upper two panels for each RI event-based category. The overall pattern is similar to that of moderately deep convection, except for 12-24 hours before RI onset, where an UL dominated distribution, mostly contributed by very deep convection, is observed (Fig. 10III.a).

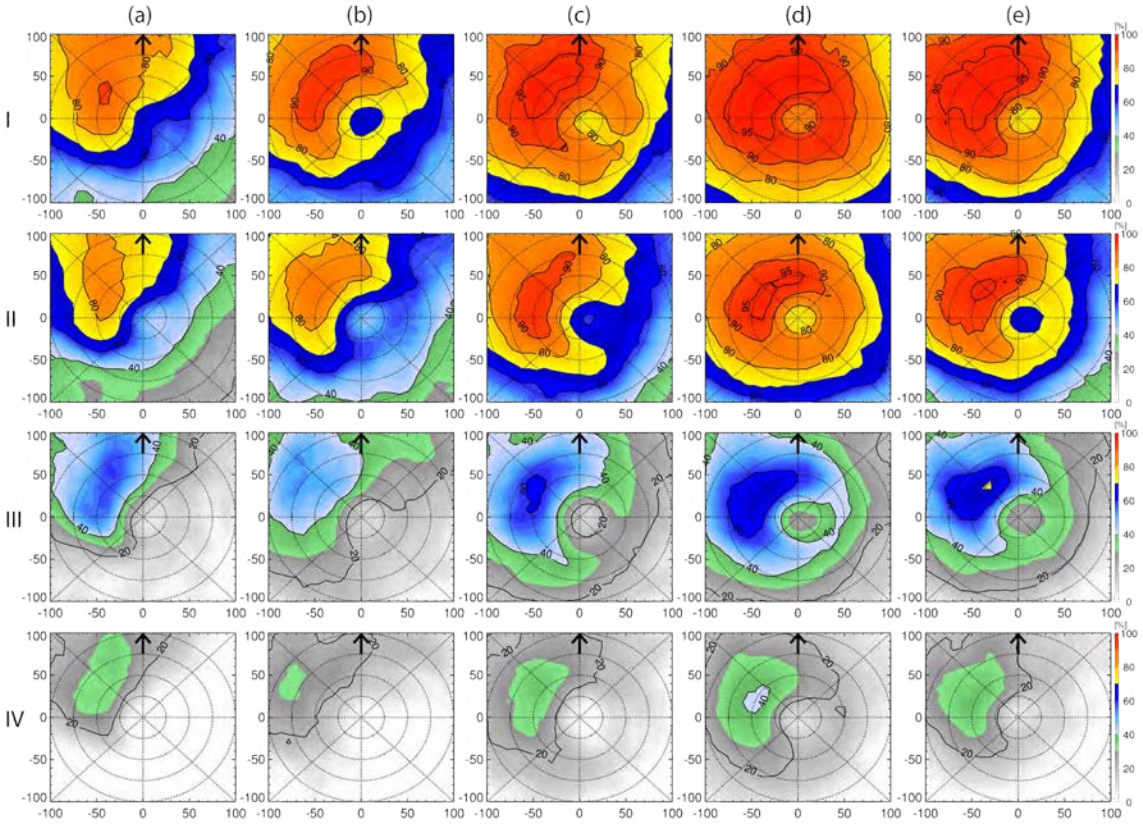

Figure 4.9: Composite shear-relative distributions of the percent occurrence of rain rate (I) > 0.5 mm/hr, (II) > 1 mm/hr, (III) > 5 mm/hr, and (IV) > 10 mm/hr. From left to right: (a) 12~24 h before RI starts, (b) 0~12 h before RI starts, (c) RI initial, (d) RI continuing, and (e) 12~24 h before RI ends. Dotted range rings represent the 25-, 50-, 75-, and 100-km radii.

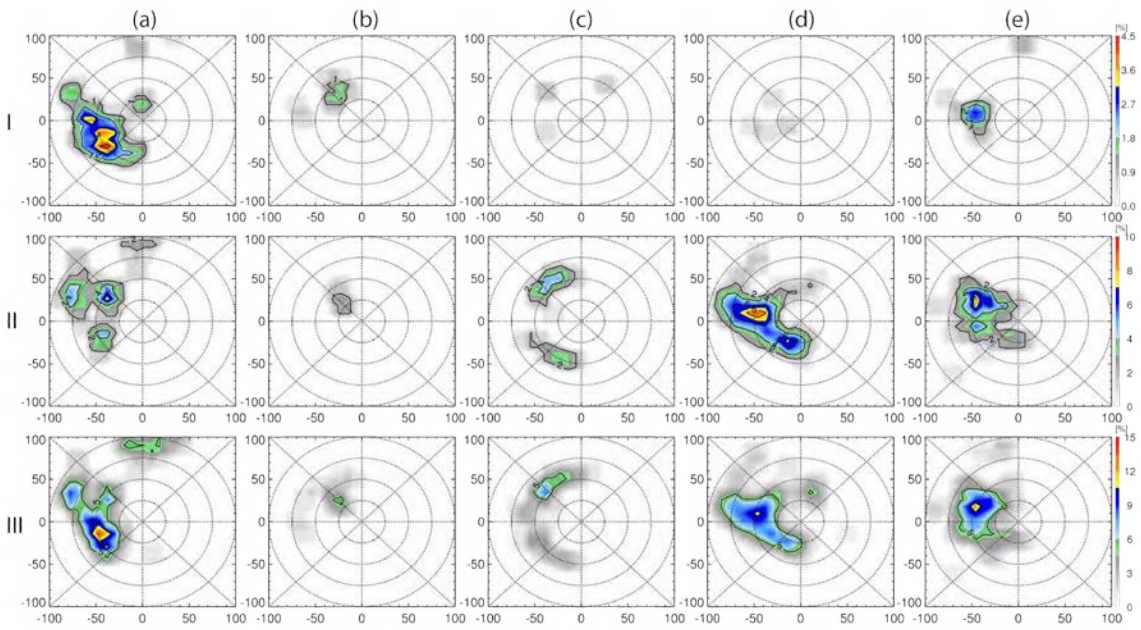

Figure 4.10: As in Fig. 4.9, except for percent occurrence of 85 GHz PCT (I) < 160 K, (II) 160-200 K, and (III) < 200 K.

The distribution of the percent occurrence of moderate precipitation is DL dominated in all RI event-based categories (Fig. 4.11I). From 0-12 hours before the RI onset (Fig. 4.11I.b) to RI initial period (Fig. 4.11I.c), the significant increase in the percentage of moderate precipitation, shown in Table 4.4, is concentrated in the UL quadrant; while from RI initial to RI continuing stages (Fig. 4.11I.d), the more widespread moderate precipitation around the storm center is mostly contributed from pixels right of the shear vector (both DR and UR). A ring of ~50% of moderate precipitation is extending completely around the center for storms that have been undergoing RI for at least 12 hours. Shallow precipitation increases rapidly from 12-24 (Fig. 4.11II.a) to 0-12 (Fig. 4.11II.b) hours prior to the RI onset (Table 4.4) and the increase mostly concentrates UL, with a secondary maximum downshear. Considering both shallow and moderate precipitation, the

significant increase is firstly observed in the UL quadrant 0-12 hours prior to the RI onset (Fig. 4.11III.a-b) and rotates cyclonically with the evolution of RI events (Fig. 4.11III.c-d), similar to that of moderate precipitation. Similar results are also found for the percent occurrence of all precipitation (Fig. 4.11IV).

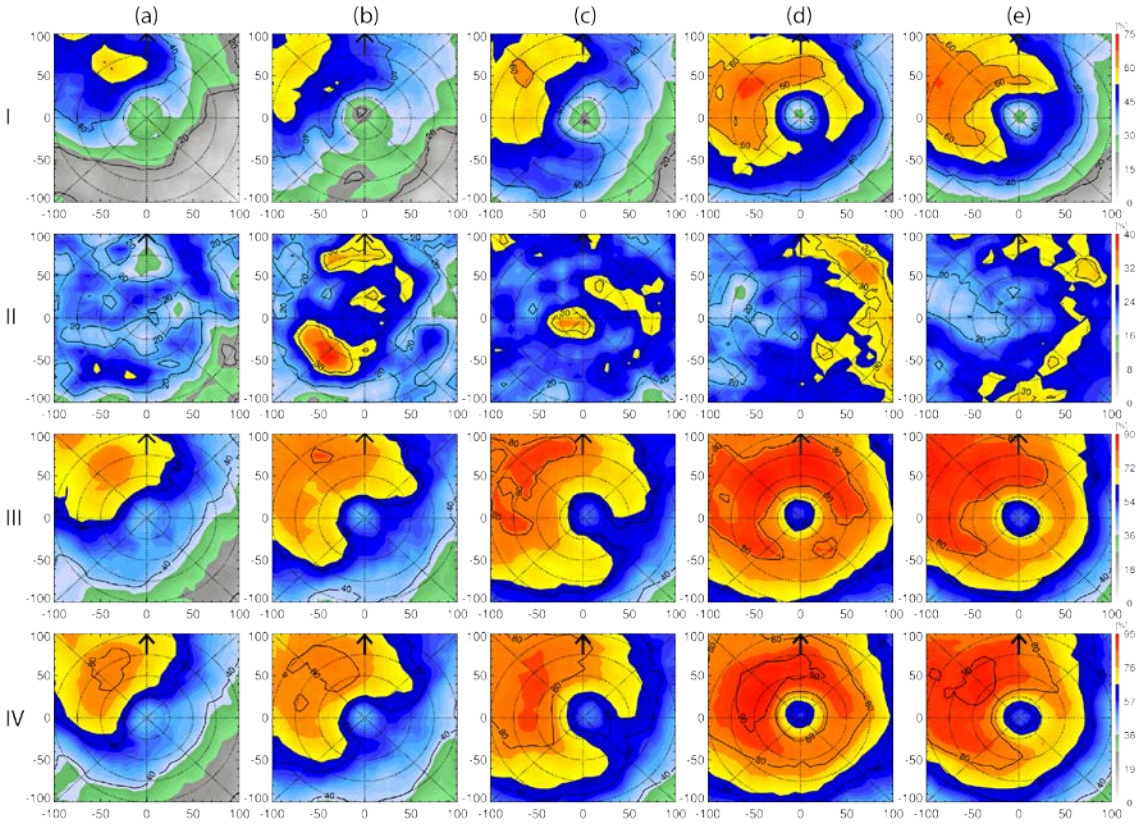

Figure 4.11: As in Fig. 4.9, except for percent occurrence of 85 GHz PCT (I) 200-260 K, (II) 260-275 K, (III) 200-275 K, and (IV) < 275 K.

3) 37 GHz brightness temperature

The percent occurrence of pink region in 37 GHz color images is DL dominated in all RI event-based categories (Fig. 4.12I). The significant increase (~10-20%) of pink 0-12 hours before the RI onset (Fig. 4.12I.b) and during the RI initial periods (Fig. 4.12I.c) is first observed UL, and then concentrates to the right of the shear in RI continuing periods (Fig. 4.12I.d). Bright cyan most commonly occurs left of the shear before the RI onset (Fig. 4.12II.a-b) but becomes more widespread when RI begins (Fig. 4.12II.c-e). The significant increase of dark cyan 0-12 hours before the RI onset is mostly contributed by pixels left of shear between 25-75 km of the storm center (Fig. 4.12III.b). The percent occurrence of dark cyan then increases steadily when RI begins and becomes right-shear dominated in RI continuing category (Fig. 4.12III.d). Considering pink and cyan (both bright and dark cyan) together, the significant increase 0-12 hours before the RI onset concentrates in the upshear semicircle, with a slightly stronger preference UL versus UR (Fig. 4.12IV.b). Pink and cyan continues to increase rapidly and becomes more widespread in RI initial and RI continuing categories (Fig. 4.12IV.c-d) but the increase has a stronger preference UR and to the right of shear, respectively. A ring of 80-90% occurrence of pink and cyan in 37 GHz color composites is extending completely around the TC center for RI continuing storms, consistent with Kieper and Jiang (2012).

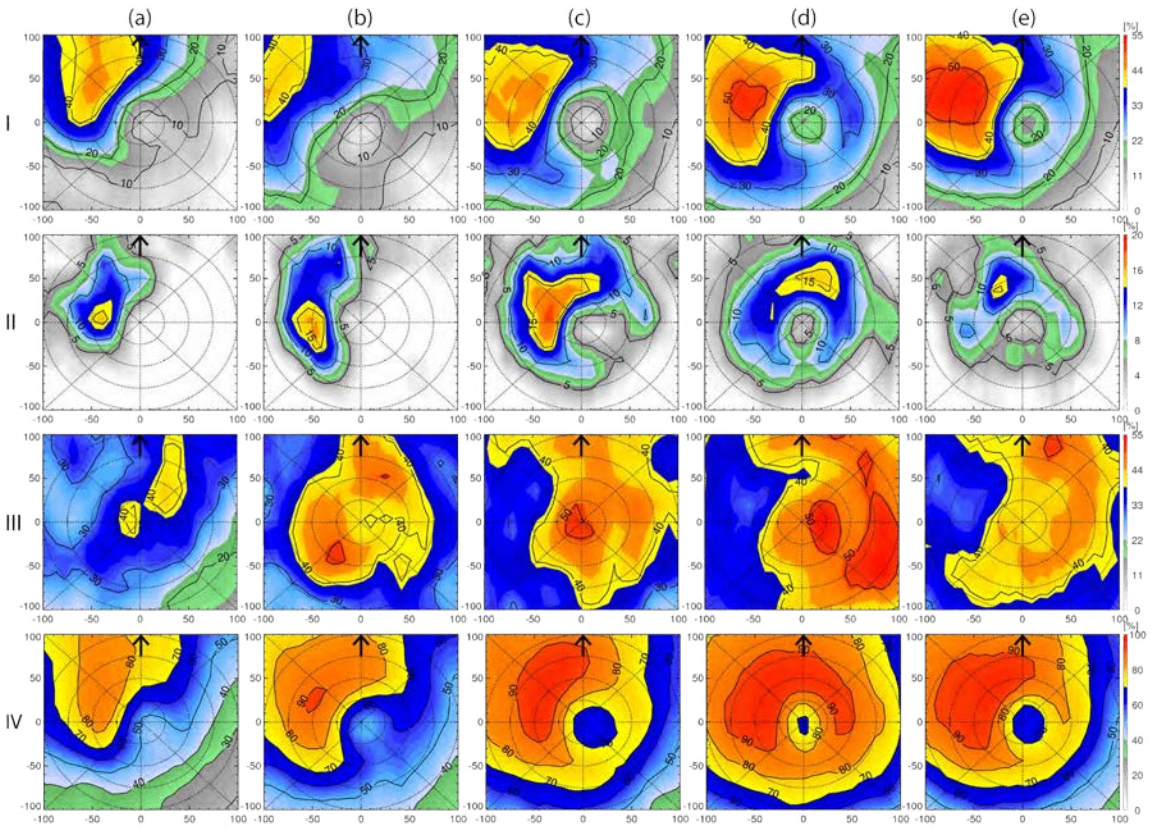

Figure 4.12: As in Fig. 4.9, except for percent occurrence of (I) pink, (II) bright cyan, (III) dark cyan, and (IV) pink and cyan.

4.4.4 Linear regression analysis

The above composite analysis indicates a relationship between RI and the areal coverage of rain rate > 0.5 and 1 mm/hr, shallow to moderate precipitation (200 K < 85 GHz PCT ≤ 275 K), and pink and cyan regions in 37 GHz color images within the inner core region of TCs. The percent occurrence of these four rainfall and convective parameters increase significantly 0-12 hours before RI onset while rapidly decreases at the beginning of the RI ending period (Table 4.4). One of the limitations of composite analysis is that the information of each individual case is not provided. This part of study presents linear regression analysis to further examine the above-mentioned four rainfall and convective

parameters with the evolution of RI events. In this section, each point represents a rainfall or convective coverage value for an individual case in contrast with an average value for all selected cases in composite analysis. Here, our focus is the period from 24 hours prior to the RI onset to 24 hours before RI ends. The areal coverage of rain rate > 1 mm/hr has the highest correlation coefficient with regard to time relative to the RI onset (0.52). Periods before the onset of RI have broad rainfall distributions, with rainfall frequency varying from near zero to greater than 95% (Fig. 4.13b). With the exception of three cases, storms during the RI periods (both RI initial and RI continuing categories) have a minimum inner 100-km rainfall (with rain rate > 1 mm/hr) coverage around 40%. A moderate relationship is also found between the time relative to the RI onset and the areal coverage of rain rate > 0.5 mm/hr (0.49), shallow to moderate precipitation (0.47), and pink and cyan regions in 37 GHz color composites (0.45).

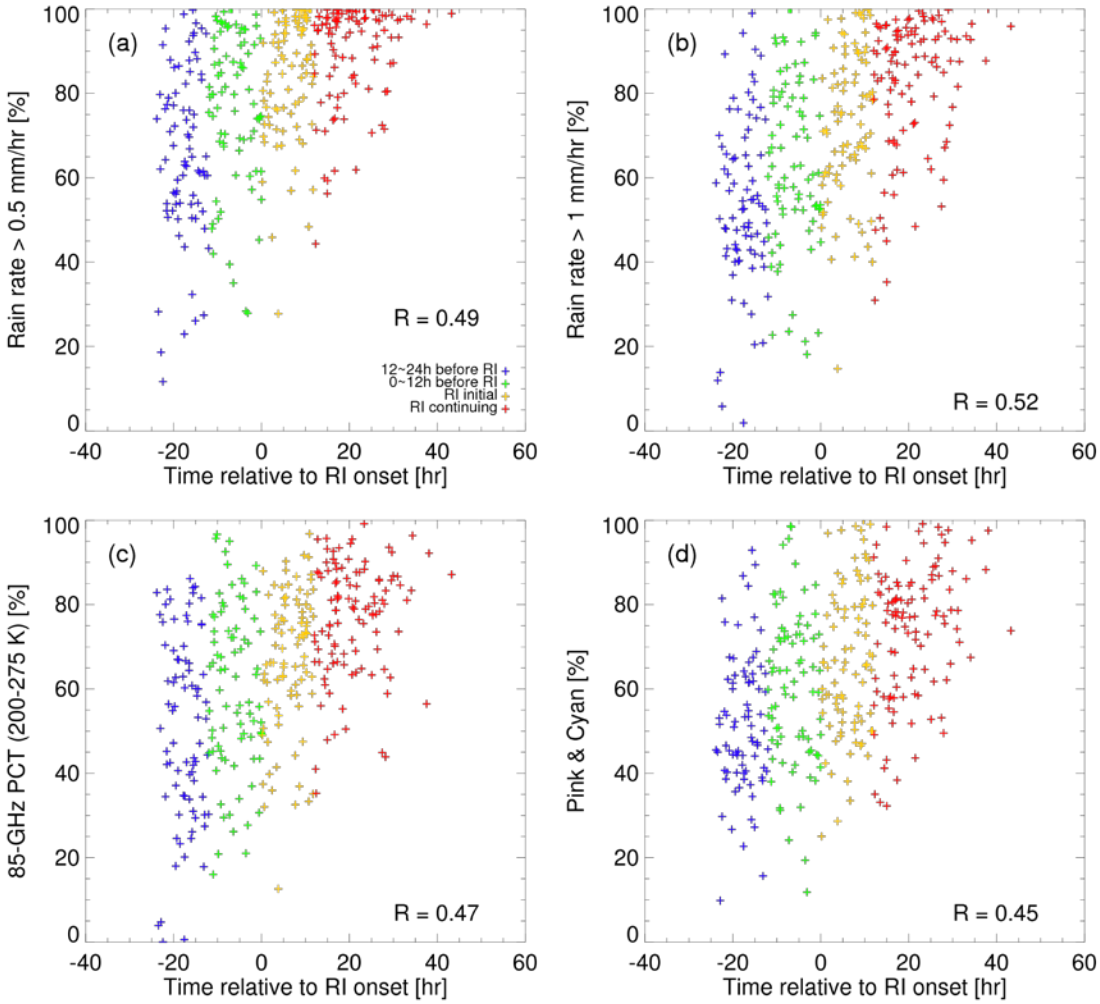

Figure 4.13: Scatterplots of percent occurrence of (a) rain rate > 0.5 mm/hr, (b) rain rate > 1 mm/hr, (c) 85 GHz PCT between 200-275 K, and (d) pink and cyan in 37 GHz color composites, versus time relative to RI onset. Negative numbers from x-axis represents hours before the onset of RI and positive number represents hours after RI onset. The correlation coefficient is included in the bottom right.

4.5 Evolution of vortex vertical alignment

4.5.1 Center determination using ARCHER

As mentioned in the introduction, recent case studies proposed that the onset of RI is triggered by the vertical alignment of the TC vortex (Rogers et al. 2015; Stevenson et al. 2014). To test this hypothesis, this section examines the evolution of the magnitude of the vortex vertical misalignment and its distribution relative to the direction of vertical wind shear. Here, the vortex vertical misalignment refers to the difference between the rotational centers of 37 and 85 GHz imageries. The rotational center of 37 GHz images approximates to the surface center while that of 85 GHz represents the center at around 10 km (Wimmers and Velden 2010). This part of study applies the Automated Rotational Center Hurricane Eye Retrieval version 2 (ARCHER-2) product (Wimmers and Velden 2016) to determine the rotational center in 37 and 85 GHz imageries derived from the TRMM TMI. The ARCHER-2 product locates the center of rotation by combining the spiral-centering algorithm with the ring-fitting algorithm. An example of the ARCHER-2 diagnostic image is shown in Figure 4.14, with the final ARCHER-2 position marked as a square. More details about the ARCHER-2 product are demonstrated in Wimmers and Velden (2010, 2016).

To evaluate the performance of the center fixing, the radius of 50% and 95% certainty are also obtained as one of the outputs in the ARCHER-2 product. These two parameters represent the corresponding expected error of the ARCHER-2 center-fixes. Therefore, the smaller the radius, the better the expected accuracy. Figure 4.15 shows the probability density function (PDF) and CDF of the 50% and 95% confidence radius for all selected TRMM TMI overpasses in this study. The overall distribution is similar for 37 and

85 GHz channels. To generate the final dataset, a 95% threshold is used here considering both center fixing accuracy and sample size, i.e., cases with expected error beyond the top 95% level are excluded.

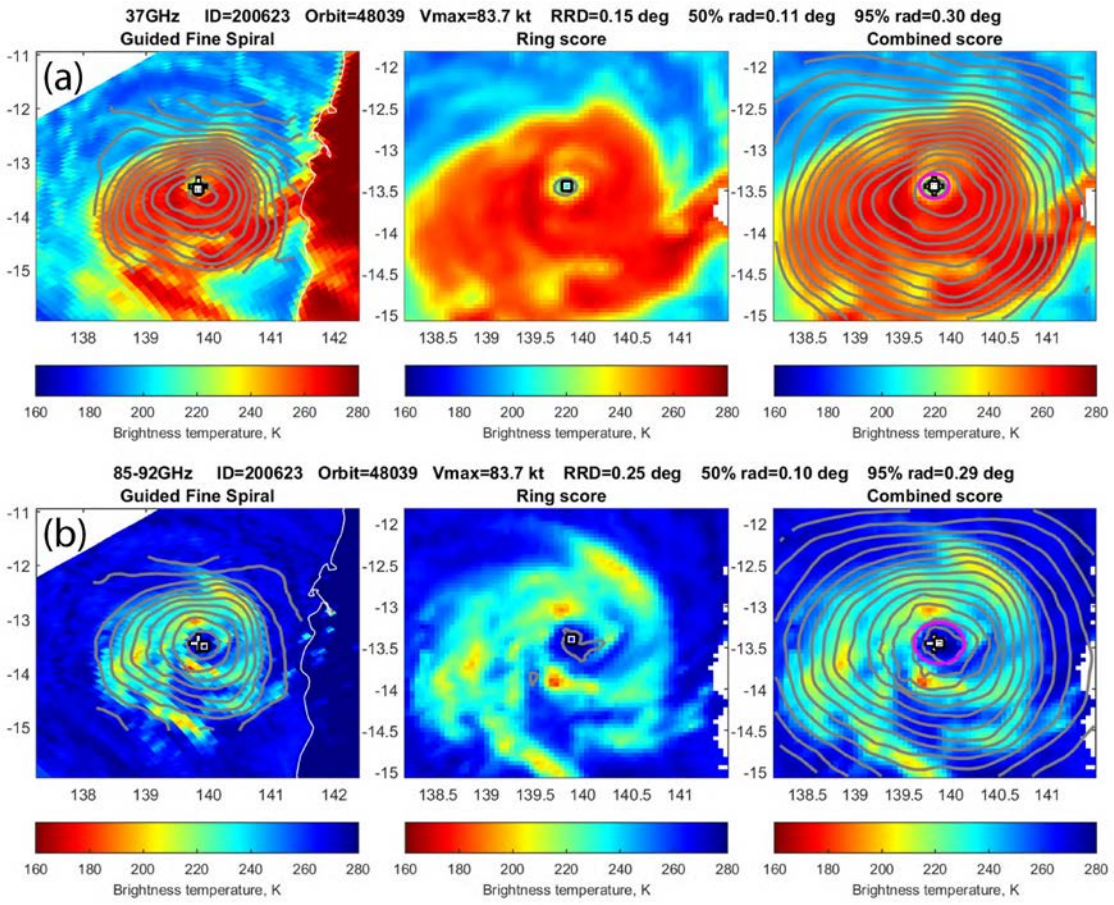

Figure 4.14: ARCHER diagnostic images for an example of (a) 37-GHz and (b) 85-GHz image for Cyclone Monica (2:12:44 UTC 21 April 2006). Background images are from TRMM TMI 37-GHz and 85-GHz channel (horizontal polarization). In each image, the cross is the first-guess position of the rotational center and the square marker is the location of the maximum score (i.e., the center used in this study). The pink circle denotes the ARCHER output eyewall inner radius.

4.5.2 Vortex vertical misalignment

With the position of the rotational centers in 37 and 85 GHz channels determined from the ARCHER-2 product, the vortex vertical misalignment is calculated for each individual case and the corresponding CDFs for seven RI event-based categories are shown in Figure 4.16. The vortex vertical misalignment has a broad distribution, varying from near zero up to 120 km. Generally, differences among the distributions of vertical misalignment are not obvious for storms in the RI continuing and RI ending periods, where the vortex is significantly less tilted compared with storms in the other RI event-based categories. Similar distributions are also found for storms that are 24-48 and 12-24 hours before the RI onset and in the RI initial periods, where the greatest values of vortex vertical misalignment are observed. Results of significance tests in Table 4.5 indicate that statistically, the magnitude of storm's vertical misalignment does not decrease much until in the middle of RI events (i.e., RI continuing category), suggesting that the vortex vertical alignment is a result or positive feedback rather than the trigger of RI. This is consistent with Chen and Gopalakrishnan (2015). Based on the result of a forecast from the operational Hurricane Weather Research and Forecast system (HWRF) of Hurricane Earl (2010), they found that the vortex was largely tilted at the onset of RI but the tilt of vortex quickly decreases as RI continues. This lessened vertical vortex tilting in the RI continuing period could be a result of the decreasing vertical wind shear as shown in Table 4.3 (DeMaria 1996).

The distributions of the vortex vertical misalignment in the inner core region of TCs are also analyzed according to the direction of vertical wind shear for each RI event-based category, using 2D scatterplots (Figure 4.17). To generate the shear-relative scatterplots,

the rotational center of each 85 GHz imagery is rotated with the shear vector pointing upward along the +y axis and the corresponding rotational center of 37 GHz in the middle. Similarly, cases of Southern Hemisphere are flipper 180^{o} before composited with those of Northern Hemisphere. In general, the direction of the displacement of 85 GHz rotational center concentrates in the DL quadrant, consistent with previous theoretical, numerical, and observational studies of vortices in a sheared environment (e.g., Rogers et al. 2003; Reasor et al. 2004; Reasor and Eastin 2012). However, there are some differences among various RI event-based categories. The tilt of vortex is much more DL-dominated for storms before the onset of RI (Fig. 4.17a-c) while more evenly distributed in both DL and DR quadrants for the other RI event-based categories (Fig. 4.17d-g).

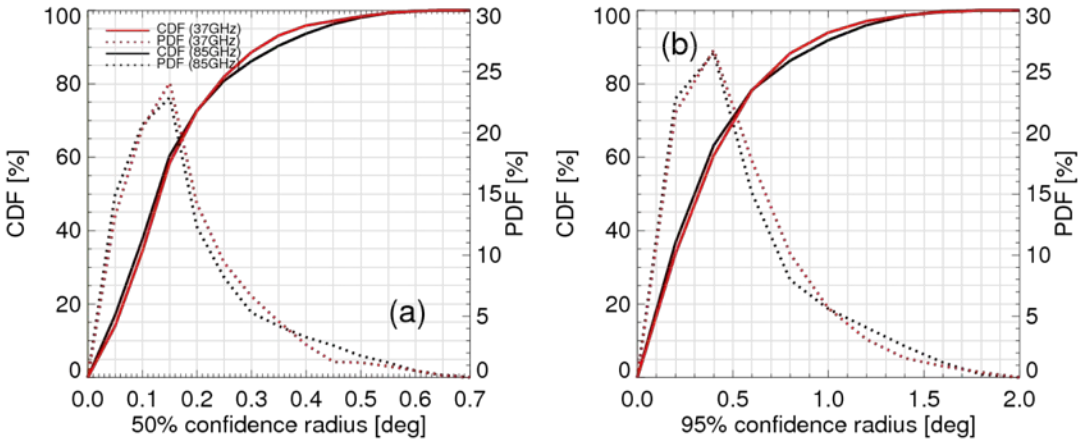

Figure 4.15: Probability density function (PDF) and cumulative distribution function (CDF) for (a) 50% and (b) 95% confidence radius.

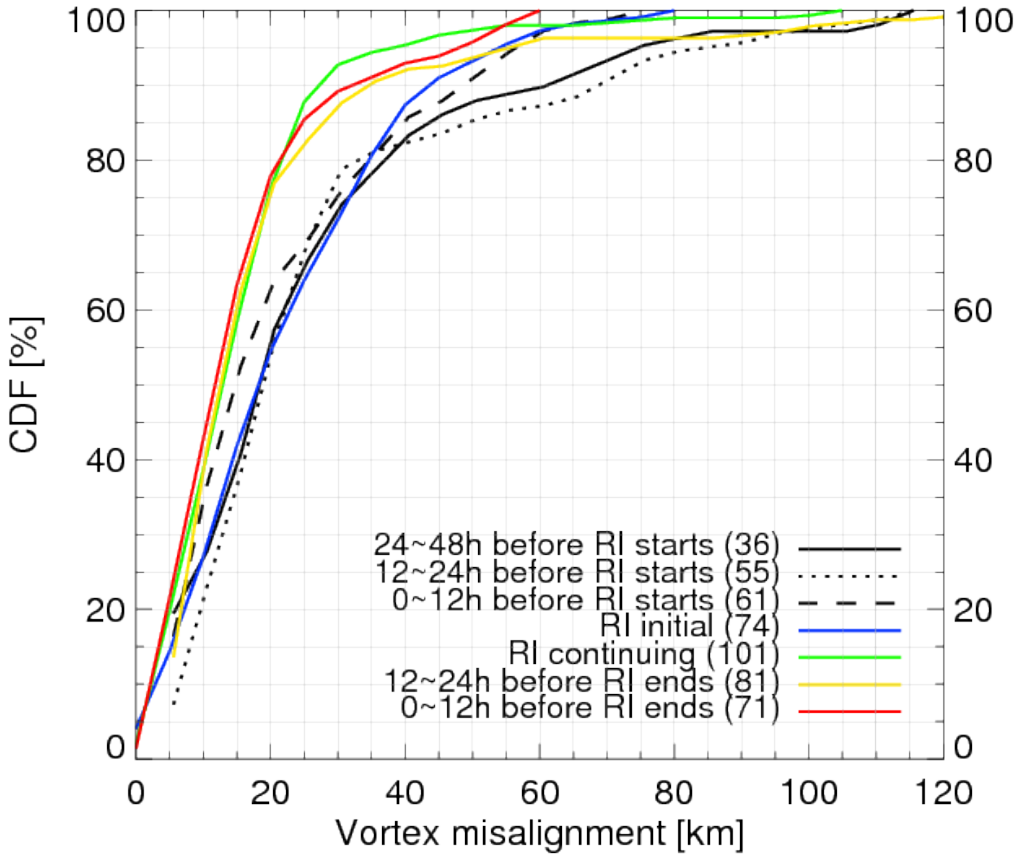

Figure 4.16: Cumulative distribution functions (CDFs) of vortex misalignment for each RI event-based category. Number in parenthesis indices the sample size.

Table 4.5: The mean, median, and standard deviation of vortex misalignment for each RI event-based category. Asterisks (**) represents the statistical significance of the value from the value in the previous column at the 99% confidence level.

	Before RI			During RI		RI ending	
	24~48	12~24	0~12	RI init.	RI cont.	12~24	0~12
Mean	29.90	31.24	24.89	26.18	19.44**	22.47	19.22
Median	22.95	24.90	17.60	23.61	16.70	16.70	16.70
Std. dev.	24.50	25.34	17.79	16.56	14.55	21.32	13.33

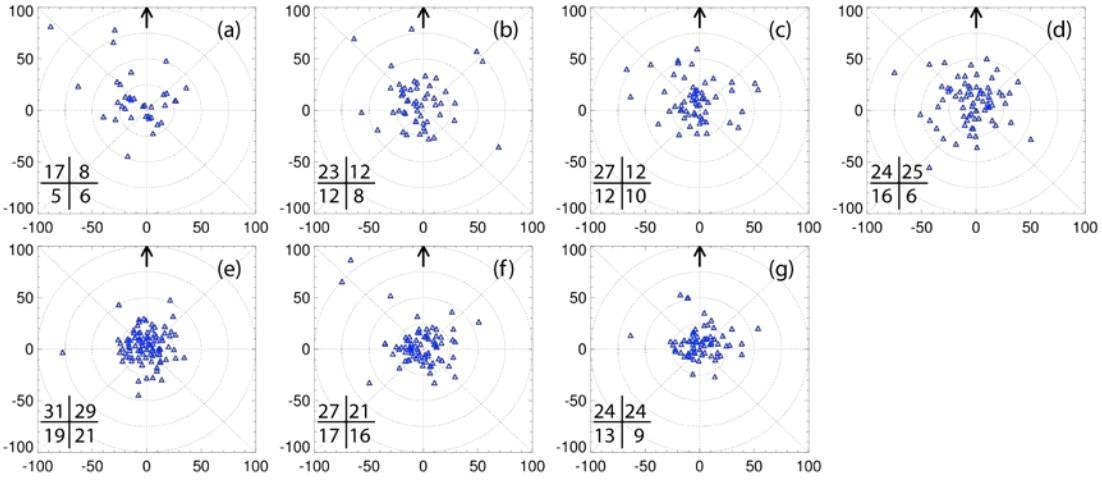

Figure 4.17: Location of the rotational center of 85 GHz imagery in (a) 24~48 hours before RI onset, (b) 12~24 hours before RI onset, (c) 0~12 hours before RI onset, (d) RI initial, (e) RI continuing, (f) 12~24 hours before RI ends, and (g) 0~12 hours before RI ends. The 85 GHz centers have been rotated around the 37 GHz centers and the direction of vertical wind shear, indicated by the arrow. Numbers in each shear-relative quadrant are shown in lower left.

4.6 Discussion and Conclusion

Based on 16 years of observations from the TRMM TMI, the evolution of rainfall and convection in the inner core region of TCs are examined in terms of RI events. Consistent with previous satellite-based studies (e.g., Jiang 2012; Zagrodnik and Jiang 2014, TJ15), both RI initial and RI continuing storms are featured with increased areal coverage of rainfall, moderate precipitation (200 K < PCT_{85} ≤ 260 K), and pink/cyan regions in 37 GHz color composite imageries (Fig. 4.6-4.8, Table 4.4). A ring of 80-90% occurrence of pink and cyan is observed in the middle of RI events (i.e., RI continuing), consistent with Kieper and Jiang (2012).

By comparing the distributions before and near the RI onset, this study further indicates that the onset of RI is closely associated with an increased coverage of rainfall and shallow precipitation. A statistically significant increase in the percent occurrence of rain rate > 0.5 and 1 mm/hr, shallow precipitation (260 K < PCT_{85} ≤ 275 K), and cyan regions is noted 0-12 hours prior to the RI onset, which in turn could be used as potential parameters to forecast the onset of RI. The shear-relative composites show that the increase in the rainfall and convection coverage is first observed in the upshear-left quadrant 0-12 hours before the RI onset and then rotates cyclonically as RI continues, concentrating in the upshear-right quadrant for RI initial storms while right of the shear vector during the RI continuing periods (Fig. 4.9-4.12). The beginning of the RI ending periods (a 24-hour period before RI ends) follows a statistically significant decrease in the areal coverage of rainfall and cyan regions in 37 GHz color composites, especially right of the shear vector, indicating that increased rainfall and cyan (warm rain or low-level water clouds) are also important in maintaining the RI of TCs.

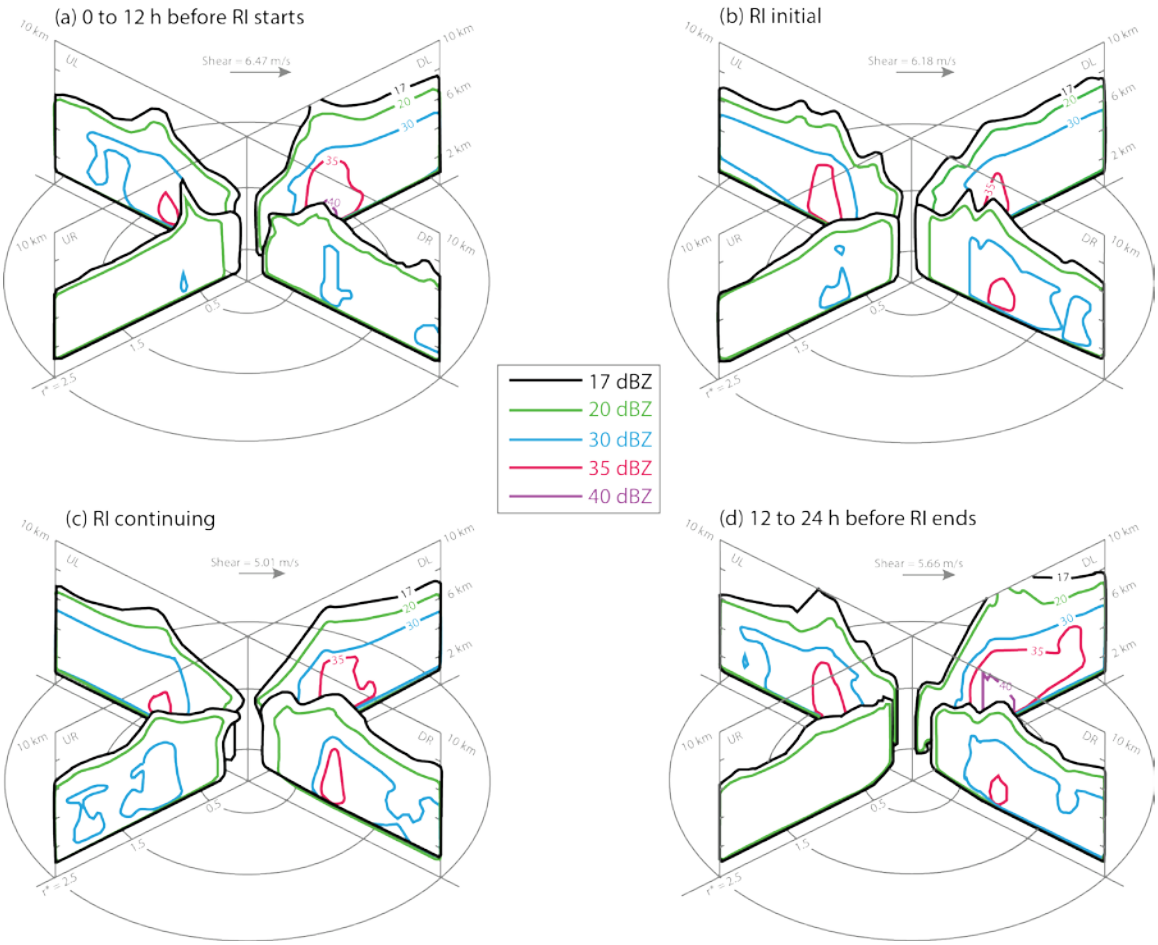

Figure 4.18: Schematic illustration depicting the radial-height diagrams of mean radar reflectivities for storms (a) 0-12 hours before RI starts, (b) RI initial, (c) RI continuing, and (d) 12-24 hours before RI ends. Distance is normalized by the radius of maximum reflectivity. Arrows indicate the direction of vertical wind shear, and quadrants are labeled according to their direction relative to the shear vector (DR, DL, UL, and UR).

This study suggests that the occurrence of very deep convection ($PCT_{85} \leq 160$ K) is not directly linked with the onset of RI, consistent with Jiang (2012) and TJ15. Although a significant increase in the areal coverage of very deep convection is observed 12-24 hours prior to the RI onset, it quickly decreases in the following 12 hours and does not increase until several hours before RI ends. Statistically, the percent occurrence of very deep convection is less than 1% during both the RI initial and RI continuing periods (Fig. 4.9a & Fig. 4.12I). This is contrary to recent observational case studies (e.g., Stevenson et al. 2014; Rogers et al. 2015) that indicated the RI onset is triggered by the lightning or convective bursts around the storm center. The magnitude of the vortex vertical misalignment is also quantified for each RI event-based category using the ARCHER-2 product. The tilt of vortex is large near the onset of RI and decreases rapidly in the middle of RI events (Fig. 4.16), suggesting that vertical alignment is the result instead of the trigger of RI (Chen and Gopalakrishnan, 2015). Consistent with previous studies, the direction of the displacement of rotational center in 85 GHz channels concentrates in the downshear-left quadrant before the onset of RI. But the tilt of vortex becomes more evenly distributed in both downshear-left and downshear-right quadrants when RI starts (Fig. 4.17).

Figure 4.18 shows a schematic[5] outlining the radial-height diagram of mean radar reflectivity in four shear-relative quadrants, where the vertical wind shear is pointing to the right. Storms 0-12 hours before the RI onset (Fig. 4.18a) have a strong shear-induced wavenumber-1 distribution of convection: radar reflectivities are much stronger in the

[5] The schematic is depicted based on the radar reflectivity derived from the TRMM PR. The dataset used here is a subset of that in this study, which includes all well observed PR overpasses.

downshear-left quadrant, with a maximum of 40-45 dBZ. Such wavenumber-1 distribution of convection decreases after RI begins (Fig. 4.18b). Radar reflectivities get stronger in the upshear-left and downshear-right quadrants while weaker in the downshear-left quadrant, resulting in a much more symmetric shear-relative distribution.

The axisymmetrization of the vortex near the RI onset could be a result of the increasing swirling wind (Table 3), as a slightly lower radar reflectivity is noted downshear-left compared with that in the upshear-left quadrant. The vortex axisymmetrization continues as RI goes on (Fig. 4.18c). Radar reflectivities are getting stronger in all shear-relative quadrants and become more symmetric. In the period of 12-24 hours before RI ends, more deep to very deep convection occur around the storm center, leading to a stronger storm with an organized eyewall. But the distribution of radar reflectivities appears more asymmetric (Fig. 4.18d) compared with that during RI (Fig. 4.18b&c): radar reflectivities are much stronger in the downshear-left quadrant. This shear-induced convective asymmetry for RI storms summarized in Fig. 4.18 is generally consistent with that of Black et al. (2002, Fig. 17). We hypothesize that near the onset of RI, the swirling wind increases and induces the vortex axisymmetrization. The increased primary circulation then triggers the strengthening of the secondary circulation, leading to a more symmetric and intense precipitation field as RI continues, which helps maintain the strengthening of the vortex. As the secondary circulation gets stronger, moderate-to-deep convection becomes more asymmetric and downshear-left dominant in the ending stage of RI.

One thing that needs to be noted is that the increased very deep convection 12-24 hours before the RI onset mostly occurs in the innermost 50 km of the storm center. Several studies (e.g., Vigh and Schubert 2009; Rogers 2010) indicated that convection located

within the radius of maximum wind (RMW) promoted the intensification of TCs. As the information of RMW cannot be addressed in this satellite-based study, more detailed examination of the convection distribution normalized with RMW is needed to further quantify the role of very deep convection in RI. Moreover, shear-relative composite analysis shows that the increased very deep convection 12-24 hours before the RI onset concentrates in the upshear-left quadrant. Chen and Gopalakrishnan (2015) suggested that convective bursts concentrated in the downshear-left and upshear-left quadrants were favorable for RI as they promoted the development of upper-level warm core. This study shows a close relationship between the increased rainfall and shallow precipitation in the upshear-left quadrant and the onset of RI. But what is the cause of this increase and whether it is related to the increased very deep convection around 12 hours before is still unknown due to the limitations of satellite observations. Besides the inner-core distributions of rainfall and convection, changes in the wind and moisture fields, and the vortex structure prior to and near the RI onset are important as well. Studies based on finer temporal and horizontal resolutions are needed to better understand the mechanisms triggering the onset of RI.

REFERENCES

Adler, R. F., G. J. Huffman, D. T. Bolvin, S. Curtis, and E. J. Nelkin, 2000: Tropical rainfall distributions determined using TRMM combined with other satellite and rain gauge information. *J. Appl. Meteor.,* 39, 2007–2023.

Alvey III, G., J. Zawislak, and E. J. Zipser, 2015: Precipitation Properties Observed during Tropical Cyclone Intensity Change. *Mon. Wea. Rev.,* 143, 4476–4492.

Black, M. L., J. F. Gamache, F. D. Marks Jr., C. E. Samsury, and H. E. Willoughby, 2002: Eastern Pacific Hurricanes Jimena of 1991 and Olivia of 1994: The effect of vertical shear on structure and intensity. *Mon. Wea. Rev.,* 130, 2291–2312.

Cecil, D. J., 2007: Satellite-derived rain rates in vertically sheared tropical cyclones. *Geophys. Res. Lett.,* 34, L02811, doi:10.1029/ 2006GL027942.

——, S. J. Goodman, D. J. Boccippio, E. J. Zipser, and S. W. Nesbitt, 2005: Three years of TRMM precipitation features. Part I: Radar, radiometric, and lightning characteristics. *Mon. Wea. Rev.,* 133, 543–566.

——, and E. J. Zipser, 2002: Reflectivity, ice scattering, and lightning characteristics of hurricane eyewalls and rain- bands. Part II: Intercomparison of observations. *Mon. Wea. Rev.,* 130, 785–801.

——, ——, and S. W. Nesbitt, 2002: Reflectivity, ice scattering, and lightning characteristics of hurricane eyewalls and rainbands. Part I: Quantitative description. *Mon. Wea. Rev.,* 130, 769–784.

Chen, H., and S. G. Gopalakrishnan, 2015: A study on the asymmetric rapid intensification of Hurricane Earl (2010) using the HWRF system. *J. Atmos. Sci.,* 72, 531–550.

Chen, S. S., J. A. Knaff, and F. D. Marks, 2006: Effects of vertical wind shear and storm motion on tropical cyclone rainfall asymmetries deduced from TRMM. *Mon. Wea. Rev.,* 134, 3190–3208.

Corbosiero, K. L., and J. Molinari, 2002: The effects of vertical wind shear on the distribution of convection in tropical cy- clones. *Mon. Wea. Rev.,* 130, 2110–2123.

——, and ——, 2003: The relationship between storm motion, vertical wind shear, and convective asymmetries in tropical cyclones. *J. Atmos. Sci.,* 60, 366–376.

DeMaria, M., 1996: The effect of vertical shear on tropical cyclone intensity change. *J. Atmos. Sci.,* 53, 2076–2088.

Dessler, A. E., 2002: The effect of deep, tropical convection on the tropical tropopause layer. *J. Geophys. Res.,* 107, 4033, doi:10.1029/2001JD000511.

Fierro, A., J. Simpson, M. A. LeMone, J. M. Straka, and B. F. Smull, 2009: On how hot towers fuel the Hadley cell: An observational and modeling study of line-organized convection in the equatorial trough from TOGA COARE. *J. Atmos. Sci.,* 66, 2730–2746.

Gettelman, A., M. L. Salby, and F. Sassi, 2002: Distribution and influence of convection in the tropical tropopause region. *J. Geophys. Res.,* 107, 4080.

Gray, W. M., 1968: Global view of the origin of tropical disturbances and storms. *Mon. Wea. Rev.,* 96, 669–700.

Guimond, S. R., G. M. Heymsfield, and F. J. Turk, 2010: Multiscale observations of Hurricane Dennis (2005): The effects of hot towers on rapid intensification. *J. Atmos. Sci.,* 67, 633–654, doi:10.1175/2009JAS3119.1.

Hall, T. J., and T. H. Vonder Haar, 1999: The diurnal cycle of west Pacific deep convection and its relation to the spatial and temporal variations of tropical MCSs. *J. Atmos. Sci.,* 56, 3401–3415.

Harnos, D. S., and S. W. Nesbitt, 2011: Convective structure in rapidly intensifying tropical cyclones as depicted by passive microwave measurements. *Geophys. Res. Lett.,* 38, L07805, doi:10.1029/2011GL047010.

Hence, D. A., and R. A. Houze Jr., 2011: Vertical structure of hurricane eyewalls as seen by the TRMM Precipitation Radar. *J. Atmos. Sci.,* 68, 1637–1652.

——, and ——, 2012: Vertical structure of tropical cyclone rain- bands as seen by the TRMM Precipitation Radar. *J. Atmos. Sci.,* 69, 2644–2661.

Hendricks, E. A., M. T. Montgomery, and C. A. Davis, 2004: The role of ‘‘vortical’’ hot towers in the formation of tropical cy- clone Diana (1984). *J. Atmos. Sci.,* 61, 1209–1232, doi:10.1175/ 1520-0469(2004)061,1209:TROVHT.2.0.CO;2.

——, M. S. Peng, B. Fu, and T. Li, 2010: Quantifying environmental control on tropical cyclone intensity change. *Mon. Wea. Rev.,* 138, 3243–3271, doi:10.1175/2010MWR3185.1.

Holton, J. R., P. H. Haynes, M. E. McIntyre, A. R. Douglass, R. B. Rood, and L. Pfister, 1995: Stratosphere–troposphere ex- change. *Rev. Geophys.,* 33, 403–439.

Houze, R. A., Jr., W.-C. Lee, and M. M. Bell, 2009: Convective contribution to the genesis of Hurricane Ophelia (2005). *Mon. Wea. Rev.,* 137, 2778–2800, doi:10.1175/ 2009MWR2727.1.

Iguchi, T., T. Kozu, R. Meneghini, J. Awaka, and K. I. Okamoto, 2000: Rain-profiling algorithm for the TRMM Precipitation Radar. *J. Appl. Meteor.,* 39, 2038–2052, doi:10.1175/ 1520-0450(2001)040,2038:RPAFTT.2.0.CO;2.

——, ——, J. Kwiatkowski, R. Meneghini, J. Awaka, and K. Okamoto, 2009: Uncertainties in the rain profiling algorithm for the TRMM Precipitation Radar. *J. Meteor. Soc.* Japan, 87A, 1–30, doi:10.2151/jmsj.87A.1.

Jiang, H., 2012: The relationship between tropical cyclone intensity change and the strength of inner-core convection. *Mon. Wea. Rev.*, 140, 1164–1176, doi:10.1175/ MWR-D-11-00134.1.

——, and E. J. Zipser, 2010: Contribution of tropical cyclones to the global precipitation from eight seasons of TRMM data: Regional, seasonal, and interannual variations. *J. Climate*, 23, 1526–1543.

——, and E. M. Ramirez, 2013: Necessary conditions for tropical cyclone rapid intensification as derived from 11 years of TRMM data. *J. Climate*, 26, 6459–6470, doi:10.1175/ JCLI-D-12-00432.1.

——, ——, and D. J. Cecil, 2013: Convective and rainfall properties of tropical cyclone inner cores and rainbands from 11 years of TRMM data. *Mon. Wea. Rew.*, 141, 431–450.

——, and C. Tao, 2014: Contribution of tropical cyclones to global deep convection. *J. Climate*, 27, 4313–4336, doi:10.1175/ JCLI-D-13-00085.1.

——, C. Liu, and E. J. Zipser, 2011: A TRMM-based tropical cy- clone cloud and precipitation feature database. *J. Appl. Meteor. Climatol.*, 50, 1255–1274.

Jiang, J. H., B. Wang, K. Goya, K. Hocke, S. F. Eckermann, J. Ma, D. L. Wu, and W. G. Read, 2004: Geographical distribution and interseasonal variability of tropical deep convection: UARS MLS observations and analyses. *J. Geophys. Res.*, 109, D03111, doi:10.1029/2003JD003756.

Johnson, R. H., T. M. Rickenbach, S. A. Rutledge, P. E. Ciesielski, and W. H. Schubert, 1999: Trimodal characteristics of tropical convection. *J. Climate*, 12, 2397–2418, doi:10.1175/ 1520-0442(1999)012,2397:TCOTC.2.0.CO;2.

Kaplan, J., and M. DeMaria, 2003: Large-scale characteristics of rapidly intensifying tropical cyclones in the North Atlantic basin. *Wea. Forecasting*, 18, 1093–1108, doi:10.1175/ 1520-0434(2003)018,1093:LCORIT.2.0.CO;2.

——, ——, and J. A. Knaff, 2010: A revised tropical cyclone rapid intensification index for the Atlantic and eastern North Pacific basins. *Wea. Forecasting*, 25, 220–241, doi:10.1175/ 2009WAF2222280.1.

Kelley, O. A., 2008: The association of tall eyewall convection with tropical cyclone wind intensification. Ph.D. dissertation, George Mason University.

——, J. Stout, and J. B. Halverson, 2004: Tall precipitation cells in tropical cyclone eyewalls are associated with tropical cyclone intensification. *Geophys. Res. Lett.,* 31, L24112, doi:10.1029/ 2004GL021616.

——, ——, and ——, 2005: Hurricane intensification detected by continuously monitoring tall precipitation in the eyewall. *Geophys. Res. Lett.,* 32, L20819, doi:10.1029/2005GL023583.

Kieper, M. E., and H. Jiang, 2012: Predicting tropical cyclone rapid intensification using the 37 GHz ring pattern identified from passive microwave measurements. *Geophys. Res. Lett.,* 39, L13804, doi:10.1029/2012GL052115.

Kistler, R., and Coauthors, 2001: The NCEP–NCAR 50-Year Reanalysis: Monthly means CD-ROM and documentation. *Bull. Amer. Meteor. Soc.,* 82, 247–267.

Kummerow, D., W. Barnes, T. Kozu, J. Shiue, and J. Simpson, 1998: The Tropical Rainfall Measuring Mission (TRMM) sensor package. *J. Atmos. Oceanic Technol.,* 15, 809-817.

——, and J. A. Weinman, 1988: Determining microwave brightness temperatures from horizontally finite, vertically structured clouds. *J. Geophys. Res.,* 93. 3720-3728.

Lee, T. F., F. J. Turk, J. Hawkins, and K. Richardson, 2002: Interpretation of TRMM TMI images of tropical cyclones. *Earth Interact.,* 6, 1–17, doi:10.1175/1087-3562(2002)006,0001: IOTTIO.2.0.CO;2.

Liu, C., and E. J. Zipser, 2005: Global distribution of convection penetrating the tropical tropopause. *J. Geophys. Res.,* 110, D23104, doi:10.1029/2005JD006063.

——, ——, and S. W. Nesbitt, 2007: Global distribution of tropical deep convection: Different perspectives form TRMM infrared and radar data. *J. Climate,* 20, 489–503.

——, ——, D. J. Cecil, S. W. Nesbitt, and S. Sherwood, 2008: A cloud and precipitation feature database from 9 years of TRMM observations. *J. Appl. Meteor. Climatol.,* 47, 2712– 2728.

Marks, F. D., and L. K. Shay, 1998: Landfalling tropical cy- clones: Forecast problems and associated research opportunities. *Bull. Amer. Meteor. Soc.,* 79, 305–323.

Merrill, R. T., 1988: Environmental influences on hurricane intensification. *J. Atmos. Sci.,* 45, 1678–1687, doi:10.1175/ 1520-0469(1988)045,1678:EIOHI.2.0.CO;2.

Molinari, J., and D. Vollaro, 2010: Rapid intensification of a sheared tropical storm. *Mon. Wea. Rev.,* 138, 3869–3885, doi:10.1175/2010MWR3378.1.

Montgomery, M. T., M. E. Nicholls, T. A. Cram, and A. B. Saunders, 2006: A vortical hot tower route to tropical cyclogenesis. *J. Atmos. Sci.,* 63, 355–386.

Montgomery, M. T., and R. K. Smith, 2011: Paradigms for tropical cyclone intensification. *Quart. J. Roy. Meteor. Soc.*, 137, 1–31.

——, M. E. Nicholls, T. A. Cram, and A. B. Saunders, 2006: A vortical hot tower route to tropical cyclogenesis. *J. Atmos. Sci.,* 63, 355–386, doi:10.1175/JAS3604.1.

Nesbitt, S. W., E. J. Zipser, and D. J. Cecil, 2000: A census of precipitation features in the tropics using TRMM: Radar, ice scattering, and lightning observations. *J. Climate,* 13, 4087–4106, doi:10.1175/1520-0442(2000)013,4087: ACOPFI.2.0.CO;2.

Nguyen, L. T., and J. Molinari, 2012: Rapid intensification of a sheared, fast-moving hurricane over the Gulf Stream. *Mon. Wea. Rev.,* 140, 3361–3378, doi:10.1175/MWR-D-11-00293.1.

Nguyen, V. S., R. K. Smith, and M. T. Montgomery, 2008: Tropical- cyclone intensification and predictability in three dimensions. *Quart. J. Roy. Meteor. Soc.,* 134, 563–582, doi:10.1002/qj.235.

Nolan, D. S., and L. D. Grasso, 2003: Nonhydrostatic, three- dimensional perturbations to balanced, hurricane-like vortices. Part II: Symmetric response and nonlinear simulations. *J. Atmos. Sci.,* 60, 2717–2745, doi:10.1175/1520-0469(2003)060,2717: NTPTBH.2.0.CO;2.

——, Y. Moon, and D. P. Stern, 2007: Tropical cyclone intensification from asymmetric convection: Energetics and efficiency. *J. Atmos. Sci.,* 64, 3377–3405, doi:10.1175/JAS3988.1.

Ooyama, K., 1969: Numerical simulation of the life cycle of tropical cyclones. *J. Atmos. Sci.,* 26, 3–40, doi:10.1175/ 1520-0469(1969)026,0003:NSOTLC.2.0.CO;2.

Park, M.-S., and R. L. Elsberry, 2013: Latent heating and cooling rates in developing and nondeveloping tropical disturbances during TCS-08: TRMM PR versus ELDORA retrievals. *J. Atmos. Sci.,* 70, 15–35, doi:10.1175/JAS-D-12-083.1.

Reasor, P. D., and M. D. Eastin, 2012: Rapidly intensifying Hurricane Guillermo (1997). Part II: Resilience in shear. *Mon. Wea. Rev.,* 140, 425–444, doi:10.1175/MWR-D-11-00080.1.

——, M. T. Montgomery, and L. F. Bosart, 2005: Mesoscale observations of the genesis of Hurricane Dolly (1996). *J. Atmos. Sci.,* 62, 3151–3171, doi:10.1175/JAS3540.1.

——, M. D. Eastin, and J. F. Gamache, 2009: Rapidly intensifying Hurricane Guillermo (1997). Part I: Low-wavenumber structure and evolution. *Mon. Wea. Rev.,* 137, 603–631, doi:10.1175/ 2008MWR2487.1.

——, R. F. Rogers, and S. Lorsolo, 2013: Environmental flow impacts on tropical cyclone structure diagnosed from airborne Doppler radar composites. *Mon. Wea. Rev.*, 141, 2949–2969, doi:10.1175/MWR-D-12-00334.1.

Petersen, W. A., and S. A. Rutledge, 2001: Regional variability in tropical convection: Observations from TRMM. *J. Climate,* 14, 3566–3586.

Reynolds, R. W., T. M. Smith, C. Liu, D. B. Chelton, K. S. Casey, and M. G. Schlax, 2007: Daily high-resolution-blended analyses for sea surface temperature. *J. Climate,* 20, 5473–5496, doi:10.1175/2007JCLI1824.1.

Riehl, H., and J. S. Malkus, 1958: On the heat balance in the equatorial trough zone. *Geophysica,* 6, 503–538.

Rogers, R. F., 2010: Convective-scale structure and evolution during a high-resolution simulation of tropical cyclone rapid intensification. *J. Atmos. Sci.*, 67, 44–70, doi:10.1175/2009JAS3122.1.

——, S. S. Chen, J. Tenerelli, and H. E. Willoughby, 2003: A numerical study of the impact of vertical shear on the distribution of rainfall in Hurricane Bonnie (1998). *Mon. Wea. Rev.*, 131, 1577–1599, doi:10.1175//2546.1.

——, P. D. Reasor, and S. Lorsolo, 2013: Airborne Doppler observations of the inner-core structural differences between intensifying and steady-state tropical cyclones. *Mon. Wea. Rev.*, 141, 2970–2991, doi:10.1175/MWR-D-12-00357.1.

——, ——, and J. A. Zhang, 2015: Multiscale structure and evolution of Hurricane Earl (2010) during rapid intensification. *Mon. Wea. Rev.*, 143, 536–562, doi:10.1175/ MWR-D-14-00175.1.

Romps, D. M., and Z. M. Kuang, 2009: Overshooting convection in tropical cyclones. *Geophys. Res. Lett.*, 36, L09804, doi:10.1029/2009GL037396.

Rosenlof, K. H., 1995: The seasonal cycle of the residual mean meridional circulation in the stratosphere. *J. Geophys. Res.,*100 (D3), 5173–5191.

Schumacher, C., and R. A. Houze Jr., 2003: Stratiform rain in the tropics as seen by the TRMM Precipitation Radar. *J. Climate,* 16, 1739–1756.

Shapiro, L. J., and H. E. Willoughby, 1982: The response of balanced hurricanes to local sources of heat and momentum. *J. Atmos. Sci.*, 39, 378–394, doi:10.1175/1520-0469(1982)039,0378: TROBHT.2.0.CO;2.

Shige, S., Y. N. Takayabu, W.-K. Tao, and D. E. Johnson, 2004: Spectral retrieval of latent heating profiles from TRMM PR data. Part I: Development of a model-based algorithm. *J. Appl. Meteor.*, 43, 1095–1113, doi:10.1175/1520-0450(2004)043,1095: SROLHP.2.0.CO;2.

——, ——, ——, and C.-L. Shie, 2007: Spectral retrieval of latent heating profiles from TRMM PR data. Part II: Algorithm improvement and heating estimates over tropical ocean regions. *J. Appl. Meteor. Climatol.,* 46, 1098–1124, doi:10.1175/ JAM2510.1.

Simmons, A., S. Uppala, D. Dee, and S. Kobayashi, 2007: ERA- Interim: New ECMWF reanalysis products from 1989 on- wards. *ECMWF Newsletter*, No. 110, ECMWF, Reading, United Kingdom, 26–35.

Simpson, R., 1978: On the computation of equivalent potential temperature. *Mon. Wea. Rev.,* 106, 124–130, doi:10.1175/ 1520-0493(1978)106,0124:OTCOEP.2.0.CO;2.

Simpson, J., 1990: Global circulation and tropical cloud activity. *Proc. Int. Symp. on Aqua and Planet,* Tokyo, Japan, Tokai University, 77–90.

Spencer, R. W., H. M. Goodman, and R. E. Hood, 1989: Precipitation retrieval over land and ocean with the SSM/I: Identification and characteristics of the scattering signal. *J. Atmos. Oceanic Technol.,* 6, 254–273, doi:10.1175/1520-0426(1989)006,0254: PROLAO.2.0.CO;2.

Stevenson, S. N., K. L. Corbosiero, and J. Molinari, 2014: The convective evolution and rapid intensification of Hurricane Earl (2010). *Mon. Wea. Rev.,* 142, 4364–4380, doi:10.1175/ MWR-D-14-00078.1.

Susca-Lopata, G., J. Zawislak, E. J. Zipser, and R. F. Rogers, 2015: The role of observed environmental conditions and precipitation evolution in the rapid intensification of Hurricane Earl (2010). *Mon. Wea. Rev.,* 143, 2207–2223, doi:10.1175/MWR-D-14-00283.1.

Tao, C., and H. Jiang, 2015: Distributions of shallow to very deep precipitation-convection in rapidly intensifying tropical cyclones. *J. Climate*, 28, 8791-8824, doi: http://dx.doi.org/10.1175/JCLI-D-14-00448.1.

Tao, C., and H. Jiang, 2013: Global distribution of hot towers in tropical cyclones based on 11-yr TRMM data. *J. Climate*, 26, 1371–1386, doi:10.1175/JCLI-D-12-00291.1.

Tao, W., E. A. Smith, R. F. Adler, Z. S. Haddard, A. Y. Hou, T. Iguchi, R. Kakar, T. N. Krishnamurti, C. D. Kummerow, S. Lang, R. Meneghini, K. Nakamura, T. Nakazawa, K. Okamoto, W. S. Olson, S. Satoh, S. Shige, J. Simpson, Y. Takayabu, G. J. Tripoli, and S. Yang, 2006: Retrieval of latent heating from TRMM measurements, *Bulletin of the AMS*, November 2006, 1555-1572.

Vigh, J. L., and W. H. Schubert, 2009: Rapid development of the tropical cyclone warm core. *J. Atmos. Sci.,* 66, 3335–3350, doi:10.1175/2009JAS3092.1.

Wang, Y., and C.-C. Wu, 2004: Current understanding of tropical cyclone structure and intensity changes—A review. *Meteor. Atmos. Phys.,* 87, 257–278, doi:10.1007/s00703-003-0055-6.

Wilheit, T. T., A. T. C. Chang, M. S. V. Rao, E. B. Rodgers, and J. S. Theon, 1977: A satellite technique for quantitatively mapping rainfall rates over the oceans. *J. Appl. Meteor.,* 16, 551-560.

Willoughby, H. E., J. A. Clos, and M. G. Shoreibah, 1982: Concentric eye walls, secondary wind maxima, and the development of the hurricane vortex. *J. Atmos. Sci.,* 39, 395–411, doi:10.1175/1520-0469(1982)039,0395: CEWSWM.2.0.CO;2.

Wimmers, A., and C. Velden, 2010: Objectively determining the rotational center of tropical cyclones in passive microwave satellite imagery. *J. Appl. Meteor. Climatol.,* 49, 2013–2034.

——, and ——, 2016: Advancements in objective multisatellite tropical cyclone center fixing. *J. Appl. Meteor. Climatol.,* 55, 197–212.

Wingo, M. T., and D. J. Cecil, 2010: Effects of vertical wind shear on tropical cyclone precipitation. *Mon. Wea. Rev.,* 138, 645– 662, doi:10.1175/2009MWR2921.1.

Wu, R., and J. A. Weinman, 1984: Microwave radiances from precipitating clouds containing aspherical ice, combined phase, and liquid hydrometeors. *J. Geophys. Res.,* 89, 7170-7178.

Yulaeva, E., J. R. Holton, and J. M. Wallace, 1994: On the cause of the annual cycle in the tropical lower-stratospheric temperatures. *J. Atmos. Sci.,* 51, 169–174.

Zagrodnik, J. P., and H. Jiang, 2014: Rainfall, convection, and la- tent heating distributions in rapidly intensifying tropical cyclones. *J. Atmos. Sci.,* 71, 2789–2809, doi:10.1175/ JAS-D-13-0314.1.

Zhang, D.-L., and H. Chen, 2012: Importance of the upper- level warm core in the rapid intensification of a tropical cyclone. *Geophys. Res. Lett.,* 39, L02806, doi:10.1029/ 2011GL050578.

Zipser, E. J., D. Cecil, C. Liu, S. Nesbitt, and D. Yorty, 2006: Where are the most intense thunderstorms on earth? *Bull. Amer. Meteor. Soc.,* 87, 1057–1071.

VITA

CHENG TAO

	Born, Wuhan, Hubei, China PR
2006-2010	B.S., Applied Meteorology Sun Yat-Sen University Guangzhou, China PR
2010-2011	Teaching Assistant Florida International University Miami, Florida
	NASA GRIP Group Achievement Award
2011-2014	Research Assistant Florida International University Miami, Florida
	NASA Earth and Space Science Fellowship (NESSF)
	WxChallenge Forecasting Competition Category 2 Winner for Duluth, MN
2013-2015	Doctoral Candidate Florida International University Miami, Florida
	Dissertation Year Fellowship (DYF) Florida International University

PUBLICATIONS

Tao, C., and H. Jiang, 2015: Distributions of shallow to very deep precipitation-convection in rapidly intensifying tropical cyclones. *J. Climate,* **28,** 8791-8824.

Jiang, H., and C. Tao, 2014: Contribution of tropical cyclones to global deep convection. *J. Climate,* **27,** 4313-4336.

Tao, C., and H. Jiang, 2013: Global distribution of hot towers in tropical cyclones based on 11-year TRMM data. *J. Climate,* **26,** 1371-1386.